# Analytical Planet-Centred Solar-Sail Trajectory Prediction with the Stark Model

MSc Thesis

Federico Fructuoso Vidal-Aragón

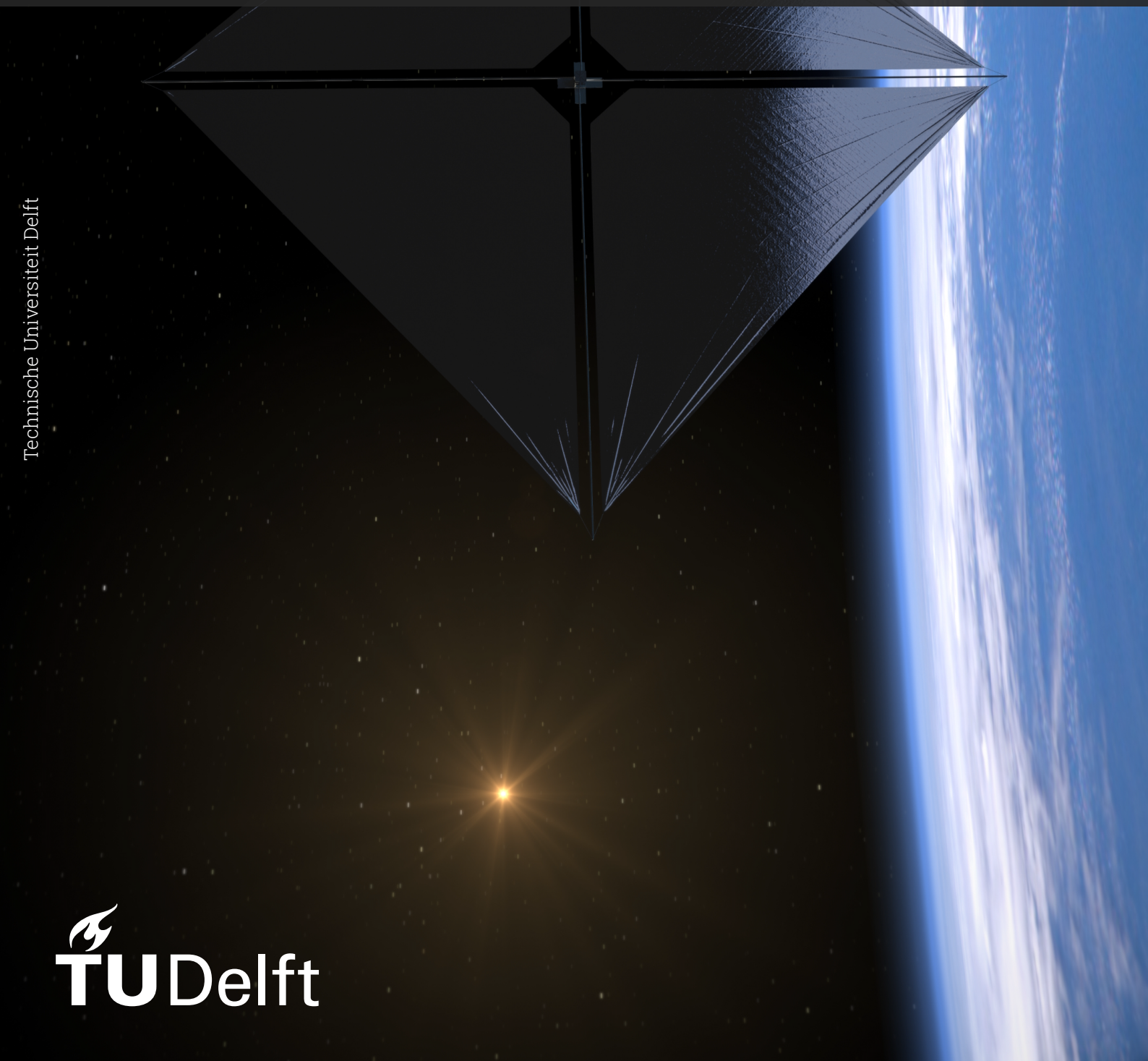

Technische Universiteit Delft

TU Delft

# Analytical Planet-Centred Solar-Sail Trajectory Prediction with the Stark Model

## MSc Thesis

by

Federico Fructuoso Vidal-Aragón

to obtain the degree of Master of Science in Aerospace Engineering
at Delft University of Technology
to be defended publicly on Monday, October 27, 2025, at 13:00.

**Student number**: 6052932
**Project duration**: January 13, 2025 – October 27, 2025
**Thesis committee**:

| | |
|---|---|
| Dr. ir. M.J. Heiligers, | TU Delft, Supervisor |
| Dr. J. Guo, | TU Delft, Chair |
| Dr. João de Teixeira da Encarnaçao, | TU Delft, External examiner |

**Cover**: Artist's concept of NASA's Advanced Composite Solar Sail System spacecraft in Earth orbit with the Sun in the background. Credit: NASA/Aero Animation/Ben Schweighart (Modified).

An electronic version of this thesis is available at `http://repository.tudelft.nl/`.

TU Delft

# Preface

This thesis represents the culmination of my two-year journey through space. It has not been an easy process, but this master's degree has allowed me to deepen my knowledge in space, experience Dutch culture, and meet incredible people. Therefore, I do not regret a single moment that has taken me where I am today, and I would like to express my gratitude to some of the people who have supported me throughout this process.

My deepest appreciation to my supervisor, Jeannette Heiligers, for her patience and dedication devoted to the thoughtful guidance of this work and for promoting my personal and academic growth.

Special thanks to my family, in particular to my parents, Piedad and Gonzalo, and my brother Gerardo, who have been my supporting pillars not only through the master's but through every moment of my life, and have encouraged me to pursue my goals, making me a better person. It does not matter how many times I let them down; they always stay by my side, and I will always be eternally grateful to them.

Lastly, I would like to extend my sincere thanks to my friends from the master's, especially to Gabriel, Varun, Jasper, and Manuel, for making my time at Delft a much more enjoyable and lighter experience, and for their constant emotional and academic support during this time, making the journey much easier and more remarkable.

*Federico Fructuoso Vidal-Aragón*
*Delft, October 2025*

# Executive Summary

Planet-centred solar sailing is emerging as a relevant concept in astrodynamics, complementing the historically dominant focus on heliocentric applications. By exploiting solar radiation pressure (SRP), solar sails can sustain non-Keplerian motion in Earth-centred scenarios, enabling displaced orbits, pole-sitter missions, orbit precession for persistent coverage, and propellantless station-keeping. These capabilities highlight the potential of solar sailing to support future Earth observation and communication missions.

For mission design, particularly in preliminary design phases and global trade-space exploration, analytical and semi-analytical models may offer compelling computational advantages. They can reduce the per-evaluation cost of trajectory propagation and steering-law evaluation, enabling larger parameter sweeps and faster optimisation loops compared to brute-force numerical propagation. The Stark model provides a convenient analytical framework, capturing first-order deviations from Keplerian motion while admitting closed- or semi-closed-form solutions.

Although the Stark model has been studied in the context of low-thrust propulsion, time-varying perturbations, such as $J_2$ and atmospheric drag, and, briefly, for SRP-perturbed orbits, its application to controlled solar-sail trajectories around Earth remains largely unexplored. The objective of this thesis is therefore to assess the performance of the Stark model in this context, with particular emphasis on accuracy and computational efficiency compared to classical numerical integration methods.

The acceleration model incorporates point-mass gravity and SRP under the following simplifying assumptions: constant Sun-sail distance, parallel-rays approximation, neglect of eclipses, and ideal sail behaviour. For a fixed sail attitude, these assumptions yield a force of constant magnitude and direction, forming the basis for the integration of the Stark model.

The Stark model is derived through the Hamilton-Jacobi integration of the equations of motion. For constant control laws, the model enables a direct evaluation of the state at any time. For time-varying control laws, obtaining the solution requires a discretisation of the trajectory into intervals where the control is assumed constant, followed by analytical integration of each interval. The analysis focuses on the bounded solution of the Stark problem, consistent with Earth-centred applications.

The analysis is structured into two main components: (i) the study of the model under constant control laws and (ii) the study of the model under time-varying control laws, corresponding to analytical formulations for locally optimal raising of individual orbital elements: semi-major axis (SMA), eccentricity, inclination, right ascension of the ascending node (RAAN), and argument of periapsis. The first component evaluates the performance of the model across different sail parameters and orbital regimes, while the second examines its behaviour under varying control profiles. In the latter case, comparisons are established against classical numerical integrators by imposing fixed step sizes for analytical propagation and integration tolerances for the numerical solver. A complementary analysis is also performed with variable step sizes determined adaptively by the numerical integration scheme.

Performance is assessed in terms of computational time and the maximum position error, $\Delta r_{\max}$, accumulated over the propagation interval. Velocity errors were also assessed but yielded analogous trends and are therefore omitted in the thesis. The reference numerical integrator is the Runge-Kutta 45 (RK45) scheme with a tolerance of $tol = 10^{-14}$. The reference lightness number $\beta$ corresponds to the Advanced Composite Solar Sail System (ACS3), with $\beta_{ACS3} = 0.0077$, and the nominal reference orbit is that of ACS3, with a SMA of $a = 7346$ km. All simulations were carried out over a one-day propagation.

For constant control laws, the Stark model demonstrated a systematic advantage in computational efficiency, owing to its capability to directly evaluate the state vector at arbitrary time instants without requiring sequential propagation. Parametric studies were performed for varying lightness number $\beta$

and cone angle $\alpha$, revealing that accuracy is strongly correlated with the magnitude of the applied perturbation. Specifically, larger perturbations reduced accumulated errors, with position errors spanning $\Delta r_{\max} \in [10^{-3}, 10^{3}]$ m for perturbation magnitudes in the range of $\epsilon \in [10^{-9}, 10^{-3}]$ m/s$^2$. The primary error source was traced to intermediate analytical functions, such as elliptic integrals, whose inaccuracies compound over long propagation intervals and are further amplified by the reciprocal of the perturbation magnitude, leading to a mismatch in the time at which the solution is evaluated. Sensitivity analyses with respect to the orbital elements showed that performance degradation was primarily associated with the SMA $a$ and eccentricity $e$: smaller $a$ and larger $e$ induce faster orbital dynamics, amplifying time mismatches and resulting in larger position errors and computational cost.

For time-varying control laws, the relative performance of the Stark model, quantified through an equally weighted metric combining computational time and positional accuracy, depended critically on the smoothness of the control profile. In the case of smooth control variations (SMA-, eccentricity-, and argument of periapsis-raising), the Stark model outperformed numerical propagation within the region of step sizes of $\Delta t \in [36, 100]$ s, where numerical methods required tolerances of $tol \in [10^{-10}, 10^{-7}]$ to match the same accuracy. For discontinuous control profiles (inclination- and RAAN-raising), the region in which the Stark model outperformed numerical propagation narrowed significantly, with effective ranges limited to $\Delta t \in [90, 100]$ s and $tol \in [10^{-8}, 10^{-7}]$. Performance also exhibited dependence on sail lightness number. For inclination- and RAAN-raising laws, outperformance occurred only for $\beta \approx 10^{-1}\beta_{ACS3}$, whereas for SMA- and eccentricity-raising laws, it extended to $\beta \in [10^{-1}, 10^{0}]\beta_{ACS3}$. In the case of argument of periapsis-raising, outperformance was maintained across the entire range $\beta \in [10^{-1}, 10^{1}]\beta_{ACS3}$. Additional analyses performed with variable step sizes showed improved accuracy in capturing the dynamics, with the Stark model outperforming numerical propagation for all control laws over tolerance ranges of $tol \in \left[10^{-9}, 10^{-4}\right]$ (slightly varying with the control law). These findings highlight a key model limitation: the inability to internally adapt step sizes under time-varying perturbations.

Overall, the findings confirm that the Stark model constitutes a valuable analytical tool for preliminary planet-centred solar sail trajectory design, particularly in scenarios governed by smooth control laws. Future work should focus on overcoming the fixed-step limitation to better handle strongly time-varying perturbations and on extending the dynamical model to incorporate additional effects such as $J_2$, atmospheric drag, third-body perturbations, and eclipses. These advancements would enhance both the accuracy and the applicability of the Stark model in realistic mission design contexts.

# Contents

# List of Figures

# List of Tables

# Abbreviations

| | |
|---|---|
| **ACS3** | Advanced Composite Solar Sail System |
| **AU** | Astronomical Unit |
| **ECI** | Earth Centred Inertial |
| **ESA** | European Space Agency |
| **IKAROS** | Interplanetary Kite-craft Accelerated by Radiation Of the Sun |
| **JAXA** | Japan Aerospace eXploration Agency |
| **LEO** | Low-Earth Orbit |
| **LOCL** | Locally Optimal Control Law |
| **NASA** | National Aeronautics and Space Administration |
| **ODE** | Ordinary Differential Equation |
| **RAAN** | Right Ascension of the Ascending Node |
| **RK45** | Runge-Kutta 45 |
| **RSW** | Radial-AlongTrack-CrossTrack |
| **SECI** | Stark Earth Centred Inertial |
| **SMA** | Semi-Major Axis |
| **SRP** | Solar Radiation Pressure |
| **TBP** | Two-Body Problem |
| **TLE** | Two-Line Element set |

# Nomenclature

## Symbols

### Latin Symbols

| | |
|---|---|
| $A$ | Area |
| $\bar{A}$ | Auxiliary parameter |
| $a$ | Semi-major axis |
| $\bar{a}$ | Auxiliary parameter |
| $\tilde{a}$ | Absorptance |
| $\mathbf{a}$ | Acceleration vector |
| $a_c$ | Solar-sail characteristic acceleration |
| $a_i$ | Polynomial coefficients |
| $\mathbf{a}_p$ | Perturbing acceleration vector |
| $\mathbf{a}_{SRP}$ | Solar radiation pressure (SRP) acceleration vector |
| $\bar{B}$ | Auxiliary parameter |
| $B_b$ | Non-Lambertian coefficient of the back solar-sail surface |
| $B_f$ | Non-Lambertian coefficient of the front solar-sail surface |
| $B_{RSW}$ | Radial-AlongTrack-CrossTrack (RSW) reference frame |
| $\bar{b}$ | Auxiliary parameter |
| $C$ | Computational time-accuracy cost function |
| $c$ | Speed of light |
| $D$ | Discriminant of the cubic equation |
| $d$ | Distance in the computational time-accuracy plane |
| $E$ | Elliptic integral of the second kind |
| $\bar{E}$ | Normalised position error |
| $\tilde{E}$ | Energy |
| $e$ | Eccentricity |
| $\bar{e}$ | Position error |
| $\tilde{e}$ | Emissivity |
| $\bar{\bar{e}}$ | Logarithmic position error |
| $\tilde{e}_b$ | Emissivity of the back surface |
| $\tilde{e}_f$ | Emissivity of the front surface |
| $F$ | Elliptic integral of the first kind |
| $\tilde{F}$ | Force |
| $\mathbf{f}$ | SRP force vector |
| $\mathbf{f}_{\tilde{a}}$ | Absorption force vector |
| $\mathbf{f}_{\tilde{e}}$ | Emission force vector |
| $\mathbf{f}_n$ | Normal force vector |
| $\mathbf{f}_{\tilde{r}}$ | Reflection force vector |
| $\mathbf{f}_{\tilde{r}s}$ | Specular reflection force vector |
| $\mathbf{f}_{\tilde{r}\bar{s}}$ | Non-specular reflection force vector |
| $\mathbf{f}_t$ | Tangential force vector |
| $f_\lambda$ | Projection of the vector $\mathbf{f}$ along the vector $\boldsymbol{\lambda}$ |
| $G$ | Gravitational constant |
| $g_1, g_2$ | Auxiliary functions |
| $H$ | Hamiltonian |
| $h$ | Plank's constant |
| $\bar{I}$ | Auxiliary function |
| $i$ | Inclination |
| $\bar{J}$ | Auxiliary parameter |
| $J_2$ | Earth's second zonal harmonic coefficient |
| $K$ | Modulus of an elliptic function or integral |
| $\tilde{K}$ | Kinetic energy |
| $L$ | Lagrangian |
| $L_\odot$ | Solar luminosity |
| $M$ | Computational time-accuracy metric |
| $\bar{M}$ | Auxiliary parameter |
| $\tilde{M}$ | Radiant flux emitted per unit area |
| $m$ | Mass |
| $\mathbf{m}$ | Direction of the SRP force vector |
| $m_0$ | Mass at rest |
| $m_\odot$ | Solar mass |
| $\bar{N}$ | Auxiliary parameter |
| $n$ | Characteristic of an elliptic integral of the third kind |
| $\mathbf{n}$ | Solar-sail normal vector |
| $O_{xyz}$ | Earth Centred Inertial (ECI) reference frame |
| $O_{x_x y_s z_s}$ | Stark Earth Centred Inertial (SECI) reference frame |
| $P$ | Pressure |
| $P_1, P_2$ | Auxiliary polynomials |
| $P_{2,i}$ | Auxiliary polynomials |
| $p$ | Linear momentum |
| $\bar{p}$ | Auxiliary parameter |
| $\mathbf{p}$ | Vector of generalised canonical momenta |
| $\tilde{\mathbf{p}}$ | Perturbing acceleration perturbation-specific parameters |
| $Q$ | Auxiliary parameter |
| $\bar{q}$ | Auxiliary parameter |
| $\mathbf{q}$ | Vector of generalised coordinates |
| $R$ | Auxiliary parameter |

| | |
|---|---|
| $\hat{\mathbf{R}}$ | Unit vector along the radial direction of the RSW reference frame |
| $R_{SECI}^{ECI}$ | Rotation matrix from ECI reference frame to SECI reference frame |
| $r$ | Distance |
| $\bar{r}$ | Complex variable modulus |
| $\tilde{r}$ | Reflectance |
| $\mathbf{r}$ | Position vector |
| $r_E$ | Earth's mean heliocentric distance |
| $r_{Moon}$ | Moon's mean geocentric distance |
| $\mathbf{r}_{t,A}$ | Analytical trajectory position vector |
| $\mathbf{r}_{t,N}$ | Numerical trajectory position vector |
| $S$ | Hamilton's principal function |
| $S'$ | Temporal contribution of Hamilton's principal function |
| $\hat{\mathbf{S}}$ | Unit vector along the along-track direction of the RSW reference frame |
| $s$ | Fraction of specular reflected photons |
| $\bar{s}$ | Fraction of non-specular reflected photons |
| $\mathbf{s}$ | Specular reflected sunlight vector |
| $T$ | Temperature |
| $\bar{T}$ | Normalised computational time |
| $T_{eq}$ | Solar-sail equilibrium temperature |
| $t$ | Physical time |
| $\bar{t}$ | Computational time |
| $\bar{\bar{t}}$ | Logarithmic computational time |
| $\mathbf{t}$ | Solar-sail tangential vector |
| $U$ | Potential energy |
| $u$ | Argument of an elliptic function or integral |
| $\mathbf{u}$ | Incident sunlight vector |
| $\bar{\mathbf{u}}$ | Auxiliary vector |
| $\mathbf{v}$ | Velocity vector |
| $W$ | Spatial contribution of Hamilton's principal function |
| $\tilde{W}$ | Solar energy flux |
| $W'$ | Radial contribution of Hamilton's principal function |
| $\hat{\mathbf{W}}$ | Unit vector along the cross-track direction of the RSW reference frame |
| $W_a$ | Contribution of Hamilton's principal function corresponding to variable $a$ |
| $\tilde{W}_E$ | Solar energy flux at Earth's mean heliocentric distance |
| $X$ | Auxiliary variable |
| $\mathbf{X}$ | Auxiliary vector in the ECI reference frame |
| $\mathbf{X}_s$ | Auxiliary vector in the SECI reference frame |
| $\tilde{\mathbf{x}}$ | State vector |
| $\hat{\mathbf{x}}$ | Unit vector along the x-axis of the ECI reference frame |
| $\hat{\mathbf{x}}_s$ | Unit vector along the x-axis of the SECI reference frame |
| $\tilde{\mathbf{x}}_{xyz}$ | State vector in Cartesian coordinates |
| $\tilde{\mathbf{x}}_{\xi\eta\phi}$ | State vector in parabolic coordinates |
| $Y$ | Auxiliary variable |
| $Y'$ | Auxiliary variable |
| $Y''$ | Auxiliary variable |
| $Y'''$ | Auxiliary variable |
| $Y_i$ | Roots of the polynomial $P_1$ |
| $Y_1'', Y_2''$ | Auxiliary parameters |
| $\hat{\mathbf{y}}$ | Unit vector along the y-axis of the ECI reference frame |
| $\hat{\mathbf{y}}_s$ | Unit vector along the y-axis of the SECI reference frame |
| $Z$ | Auxiliary variable |
| $Z_i$ | Roots of the polynomial $P_2$ |
| $\hat{\mathbf{z}}$ | Unit vector along the z-axis of the ECI reference frame |
| $\hat{\mathbf{z}}_s$ | Unit vector along the z-axis of the SECI reference frame |

## Greek Symbols

| | |
|---|---|
| $\alpha$ | Solar-sail cone angle |
| $\tilde{\alpha}$ | Cone angle of the vector $\boldsymbol{\lambda}$ |
| $\alpha'$ | Angle between the $\mathbf{x}$-axis of the ECI reference frame and the solar-sail normal vector |
| $\alpha^*$ | Optimal solar-sail cone angle |
| $\beta$ | Solar-sail lightness number |
| $\Delta t$ | Time step size |
| $\Delta\alpha$ | Difference between the angles $\alpha'$ and $\alpha$ |
| $\delta$ | Solar-sail clock angle |
| $\tilde{\delta}$ | Clock angle of the vector $\boldsymbol{\lambda}$ |
| $\delta^*$ | Optimal solar-sail clock angle |
| $\bar{\delta}_a$ | Undetermined square root sign corresponding to variable $a$ |
| $\epsilon$ | Perturbation magnitude parameter |
| $\zeta$ | Auxiliary variable |
| $\eta$ | Second radial parabolic coordinate |
| $\theta$ | True anomaly |
| $\bar{\theta}$ | Complex variable argument |
| $\kappa$ | Constant of motion in the Stark problem |
| $\lambda$ | Auxiliary parameter |
| $\boldsymbol{\lambda}$ | Vector of functions of the orbital elements of the solar sail |
| $\mu$ | Standard gravitational parameter |
| $\nu$ | Auxiliary parameter |
| $\tilde{\nu}$ | Frequency |
| $\xi$ | First radial parabolic coordinate |
| $\Pi$ | Elliptic integral of the third kind |
| $\pi$ | Mathematical constant pi |
| $\boldsymbol{\rho}$ | Vector of constants of motion in the Stark problem |
| $\sigma$ | Solar-sail loading |

| | |
|---|---|
| $\tilde{\sigma}$ | Stephan-Boltzmann constant |
| $\sigma^*$ | Critical solar-sail loading |
| $\tilde{\tau}$ | Transmission |
| $\tau_1$ | Radial fictitious time |
| $\tau_2$ | Azimuthal fictitious time |
| $\Phi_{in}$ | Thermal input |
| $\Phi_{out}$ | Thermal output |
| $\phi$ | Azimuthal parabolic coordinate |
| $\tilde{\phi}$ | Angle between the direction of the SRP force vector and the sail normal vector |
| $\varphi$ | Auxiliary variable |
| $\Omega$ | Right ascension of the ascending node |
| $\omega$ | Argument of periapsis |
| $\bar{\omega}$ | Auxiliary variable |

## Notation

| | |
|---|---|
| $\lvert\square\rvert$ | Absolute value |
| $\lvert\lvert\square\rvert\rvert$ | Norm |
| $\dot{\square}$ | First time derivative |
| $\ddot{\square}$ | Second time derivative |
| $\hat{\square}$ | Unit vector |
| $\square \cdot \square$ | Dot product |
| $\square \times \square$ | Cross product |
| $\Delta\square$ | Error or difference |
| $\square_0$ | Initial condition |
| $\square_{i/j/k}$ | Indices or counters |
| $\square_A$ | Analytical |
| $\square_N$ | Numerical |
| $\square_{a,b}$ | (Auxiliary) variable or parameter corresponding to variable $a$ and case $b$ |
| $\square_{a,0,b}$ | Initial condition of an (auxiliary) variable or parameter corresponding to variable $a$ and case $b$ |

# 1

# Introduction

Solar sailing has gained prominence as a propulsion concept due to its ability to operate without propellant. The principle is based on solar radiation pressure (SRP), in which solar photons interact with the reflective surface of the sail, transferring momentum to the spacecraft. Although much of the existing research has concentrated on heliocentric missions, increasing attention is being directed toward planet-centred solar sailing. In this setting, SRP can be harnessed to sustain non-Keplerian trajectories, enabling concepts such as displaced orbits, pole-sitter configurations, and propellantless station-keeping. These applications complement the more extensively studied heliocentric scenarios.

Within astrodynamics, mission design constitutes a core discipline, concerned with developing trajectories and control strategies that fulfil mission objectives efficiently. Typically, the process begins with a global optimisation over a wide design space using simplified dynamical models, thereby allowing the rapid identification of favourable regions. Candidate solutions are then subjected to refinement through local optimisation with higher-fidelity models, ultimately producing mission designs that are optimal or near-optimal and suitable for mission proposals.

For most dynamical models, trajectory propagation is achievable only through numerical integration. However, in certain cases, analytical or semi-analytical formulations exist, which may offer significant computational benefits relative to purely numerical approaches, thereby facilitating extensive parameter studies and accelerating optimisation procedures. The classical example is the two-body problem (TBP), where the Keplerian formulation provides an exact analytical solution at a fraction of the computational effort required by numerical propagation.

Beyond the Keplerian case, an analytical formulation is also available for the Stark problem, defined as a perturbed TBP subject to a constant perturbation in both magnitude and direction. This framework, known as the Stark model, affords an analytically manageable representation of first-order deviations from Keplerian motion while retaining closed- or semi-closed-form expressions for the solution.

Despite its potential, the Stark model has not yet been explored as a tool for preliminary mission design in the context of planet-centred solar sailing. The central aim of this thesis is to investigate the viability of employing the Stark model as an alternative to numerical propagation in such scenarios. More specifically, the work evaluates the accuracy and efficiency of the Stark model in comparison with standard numerical integration, assessing its suitability as a framework for preliminary design studies.

The thesis structure is as follows. In Chapter 2 an outline of the relevant literature regarding solar sailing and analytical models for trajectory propagation is provided. Chapter 3 delves into the research gap found in the literature review and presents the research objective of the thesis. The dynamical model, including reference systems, acceleration model, and some of the control laws used in the study are presented in Chapter 4. Then, in Chapter 5, the mathematical derivations to obtain the integrated equations of the Stark model are detailed. Chapter 6 presents the results of the thesis, supported by a brief summary of the methodology, in a paper format. Finally, conclusions extracted from the thesis and recommendations for future work are presented in Chapter 7.

# 2

# Literature Review

In this chapter, the most relevant literature will be outlined in order to identify a research gap that will later be justified and presented as a research objective. Section 2.1 contains the relevant literature on solar sails. It will start with a brief description of the principle of operation of solar sails, followed by a presentation of their history, and finally end with a detailed description of the concept of solar radiation pressure as well as the main force model used to describe the dynamics of solar sails. Section 2.2 focuses on the literature on the use of analytical models in trajectory prediction, describing the main approaches employed to reach to analytical solutions for various dynamical models as well as the literature concerning the Stark model.

## 2.1. Solar-Sailing Technology

This section provides the fundamental background to understand solar-sailing technology. Subsection 2.1.1 introduces the fundamental operating principle of solar sailing. A brief historical overview of solar sailing, including past missions is presented in Subsection 2.1.2. The discussion then proceeds in Subsection 2.1.3 to a comparative analysis of heliocentric and planet-centred solar-sailing applications. Subsequently, a detailed derivation of the momentum transfer produced by the SRP is given in Subsection 2.1.4, serving as basis for the formulation of the force model of the solar sail shown in Subsection 2.1.5.

### 2.1.1. Operating Principle

As briefly stated in Chapter 1, solar sails are a means of propulsion whose main advantage over other conventional means of propulsion, such as chemical or ion propulsion, lies in the lack of need for propellant. This is because the propulsion is generated using the energy carried by the photons of solar radiation. These photons are reflected by the sail, which produces a momentum transfer that generates a force along the direction normal to the reflection [1].

Although solar sailing enables propellantless propulsion, each photon carries a relatively small amount of energy that must be scaled up to provide sufficient acceleration for effective spacecraft control. Consequently, the design of a solar sail must consider both the spacecraft's mass and the reflective area of the sail. A commonly used metric that captures the influence of both parameters is the characteristic acceleration, $a_c$. This represents the acceleration due to SRP experienced by the solar sail when oriented normal to the sunlight at a distance of one astronomical unit (AU) from the Sun [2], which corresponds to the maximum acceleration the sail can provide the spacecraft with at that distance. For the case of ACS3, which is the latest solar-sailing demonstration mission launched, the characteristic acceleration attains a value of $a_c = 0.0455\ mm/s^2$ [3].

Although solar sails have the advantage of not needing propellant, the accelerations provided by solar sails are inherently limited. In addition, solar sails present other constraints, the most significant being their limited directionality. Since the radial component of the acceleration exerted by the solar sail always points away from the Sun, this significantly restricts the range of achievable thrust directions.

Another limitation is the degradation of the sail itself. Although theoretically conceived as an infinite means of propulsion, in reality the solar sail undergoes a process of degradation over time due to its exposure to the space environment. Therefore, the lifetime of a solar-sailing mission is limited by the lifetime of its film, which refers to the thin reflective membrane that constitutes the sail's surface. Some authors have studied the effect that degradation can have on the performance of a solar-sailing mission by considering simple analytical models and have concluded that ignoring degradation when designing a mission could lead to overestimating the solar-sail performance [4, 5].

### 2.1.2. History of Solar Sailing

The first insights on SRP date back to 1610, when Johannes Kepler observed that sunlight causes the tails of comets to point away from the Sun [6]. Later, in 1873 James Clerk Maxwell published his theory of electromagnetism, in which he stated that electromagnetic fields do not only carry energy but also momentum [7]. However, it was not until the twentieth century when Konstantin Tsiolkovsky [8, 9] and Friedrich Tsander [10] started to theorise about the use of SRP for space propulsion.

The first missions involving the use of this concept were Mariner 10 [11] and Messenger [12], which used SRP as a secondary means of propulsion. Later, in 2010, the Interplanetary Kite-craft Accelerated by Radiation Of the Sun (IKAROS) mission from the Japan Aerospace eXploration Agency (JAXA) demonstrated the use of solar sailing as a propulsion alternative to chemical or ion propulsion in interplanetary space [13]. This was considered as an incredible milestone for solar sailing and paved the way for future missions. Later that year, the National Aeronautics and Space Administration (NASA) launched NanoSail-D2, which in 2011 deployed a 10 $m^2$ sail, becoming the first sail to orbit Earth [14].

Several years later, in 2015 The Planetary Society [15] launched LightSail-1 (or LightSail-A), which, although it reentered Earth's atmosphere the same year, successfully proved the in-orbit deployment of a solar sail from a CubeSat [16]. In 2019, The Planetary Society launched LightSail-2 (or LightSail-B), which not only operated for 3.5 years, but also proved the use of solar sailing for orbit control [17], which implied a major advancement in the field.

A more recent mission was launched in 2023 by GAMA, GAMA Alpha, which was its first demonstration mission, including a 73 $m^2$ solar sail on board of a 6U CubeSat [18]. In addition, in 2024 NASA launched its ACS3 mission, aiming to demonstrate solar-sailing technology for future missions [18]. It consists of a 12U CubeSat, with an 80 $m^2$ sail that was successfully deployed several months after its launch [19].

A summary of some of these missions is presented in Table 2.1. It includes the launch year; the mass of the spacecraft, $m$; the area of the sail, $A$; the sail loading, $\sigma$, defined as the ratio of spacecraft mass to sail area; the lightness number, $\beta$, which quantifies the ratio between the acceleration induced by SRP and that due to the Sun's point-mass gravity; and the characteristic acceleration, $a_c$.

**Table 2.1:** Solar-sail characteristics of some previous successful solar-sailing missions.

| Mission | Launch Year | $m$ [$kg$] | $A$ [$m^2$] | $\sigma$ [$kg/m^2$] | $\beta$ [$-$] | $a_c$ [$mm/s^2$] |
|---|---|---|---|---|---|---|
| ACS3 [3] | 2024 | 16 | 80 | 0.2 | 0.0077 | 0.0455 |
| LightSail-2 [20] | 2019 | 4.93 | 32 | 0.154 | 0.0099 | 0.0591 |
| NanoSail-D2 [14] | 2010 | 4 | 10 | 0.4 | 0.0038 | 0.0227 |
| IKAROS [21] | 2010 | 307 | 196 | 1.566 | 0.0010 | 0.0058 |

Table 2.1 shows that recent missions, ACS3 and LightSail-2, exhibit larger values of lightness number and characteristic acceleration, indicating greater propulsive capabilities due to a lower sail loading. This trend suggests a progressive improvement in solar-sailing performance over time as technology matures.

### 2.1.3. Heliocentric versus Planet-Centred Solar Sailing

Historically, the formulation of solar-sail theory and the associated mission design methodologies have been predominantly directed toward heliocentric applications. Foundational analyses of non-Keplerian and Sun-relative trajectories demonstrated that the continuous, propellantless thrust generated by SRP enables the realization of novel families of orbits and transfer trajectories within the heliocentric regime

[1, 22]. This theoretical framework subsequently underpinned a wide range of mission concepts in heliophysics and interplanetary exploration, leveraging the sail's capability to deliver sustained acceleration without incurring the mass penalties inherent to propellant-based propulsion systems.

The JAXA IKAROS mission successfully validated the deployment, attitude control, and navigation of a large-area solar sail within the interplanetary environment [21]. Concurrently, mission concept studies by NASA and European Space Agency (ESA) proposed the use of solar-sail spacecraft positioned at displaced Sun-Earth Lagrange points to support early-warning capabilities and heliospheric science investigations [22, 23]. These configurations exploit the inherent capability of solar sails to sustain observation points located sunward of $L_1$ or at elevated solar latitudes, regions that are dynamically inaccessible to spacecraft relying solely on ballistic trajectories.

In contrast to heliocentric applications, planet-centred solar sailing has historically received comparatively limited attention, despite presenting distinct dynamical characteristics and a range of potential mission opportunities. Within the gravitational environment of a planetary system, SRP can be exploited to maintain displaced equilibrium configurations, provide continuous high-latitude coverage through so-called "pole-sitter" orbits, or induce controlled orbital precession to support targeted scientific observations. The GeoSail mission concept exemplifies this class of application, demonstrating that a relatively modest sail area can sustain a precessing orbit within Earth's magnetotail, thereby enabling uninterrupted in-situ measurements [24]. Analytical and numerical investigations have further identified additional use cases, including augmentation of geostationary coverage, provision of high-latitude communication services, and integration of solar sails within hybrid propulsion architectures combining SRP with other forms of low-thrust propulsion [25].

Flight heritage increasingly substantiates the technical feasibility of planet-centred solar-sailing applications. Demonstration missions such as NanoSail-D2 [14] and LightSail-2 [17] have successfully validated key operational capabilities, including membrane deployment, attitude control, and the detection of quantifiable SRP-induced perturbations to orbital motion in Earth orbit. More recent efforts, including GAMA Alpha [18] and NASA's ACS3 [3], have further advanced the technology readiness level for small-satellite platforms, with demonstrated or anticipated applications encompassing propellantless stationkeeping, controlled end-of-life deorbiting, and manoeuvre execution in Low-Earth Orbit (LEO) and potentially in higher-altitude or cislunar operational regimes.

In summary, although heliocentric solar-sailing missions have established the theoretical foundation and demonstrated large-scale operational capability, the planet-centred regime offers a complementary set of mission opportunities with distinct operational advantages. Potential applications include persistent observation points for scientific measurements, propellantless stationkeeping in displaced orbits, augmentation of communications coverage in high-latitude regions, and sustainable end-of-life disposal strategies. Advancing these capabilities requires systematic investigation of the underlying dynamical regimes, associated control strategies, and tailored mission architectures, representing a timely and necessary continuation of the heliocentric research tradition [14, 17, 22, 24, 25].

### 2.1.4. Solar Radiation Pressure

In Subsection 2.1.1, the underlying operating principle of solar sails was described. There, it was explained how the energy in solar radiation results in a momentum transfer to the spacecraft via photon reflection on the sail surface. To quantify the force exerted on the sail, it is first necessary to determine the radiation pressure acting on it. The derivations carried out in this subsection follow those in [1]. Since pressure is defined as force per unit area, $P = \frac{\tilde{F}}{A}$, and force is defined as the momentum transported per unit of time, $\tilde{F} = \frac{dp}{dt}$, pressure can be expressed as:

$$P = \frac{1}{A}\frac{dp}{dt} \tag{2.1}$$

To derive the expression of the SRP it is necessary to consider the momentum carried by photons. For this purpose, one must begin with the energetic properties of photons. In 1900, Max Planck established that the energy carried by a photon, $\tilde{E}$, is proportional to its frequency, $\tilde{\nu}$ [26].

$$\tilde{E} = h\tilde{\nu} \tag{2.2}$$

Here, $h$ denotes Plank's constant. Later, Einstein developed his famous energy-mass relation as part of the theory of special relativity [27].

$$\tilde{E} = mc^2 \tag{2.3}$$

In Eq. (2.3), $m$ represents the mass of the body and $c$ denotes the speed of light. Building on this, Planck introduced the energy-momentum relation, which expresses the total energy of a moving body as a function of its rest mass $m_0$ and its momentum $p$ [28].

$$\tilde{E}^2 = m_0^2 c^4 + p^2 c^2 \tag{2.4}$$

Given that $m_0 = 0$ for a photon, energy can be expressed only as a function of the momentum of a photon.

$$\tilde{E} = pc \tag{2.5}$$

Differentiating Eq. (2.5) leads to an expression of the rate of change of momentum with respect to energy.

$$\frac{dp}{d\tilde{E}} = c \tag{2.6}$$

In order to obtain the momentum transported per unit of time, the time rate of change of energy is needed. According to the definition of flux, this rate of change can be expressed as:

$$\frac{d\tilde{E}}{dt} = \tilde{W}A \tag{2.7}$$

Here, $\tilde{W}$ denotes the solar energy flux, which is given by:

$$\tilde{W} = \frac{L_\odot}{4\pi r^2} \tag{2.8}$$

Equation (2.8) represents the solar flux at a distance $r$ from the Sun, where $L_\odot$ is the solar luminosity. Combining Eqs. (2.1), (2.6) and (2.8) leads to an expression for the SRP.

$$P = \frac{L_\odot}{4\pi c r^2 A} \tag{2.9}$$

As observed, the SRP depends on the distance to the Sun and the projected area of the body under consideration perpendicular to the direction of the incident solar radiation.

### 2.1.5. Force Models

Over the years, several solar-sail force models have been developed. The most important ones have been detailed by McInnes in [1]. The two most important force models are the optical force model and the parametric force model. Here, only the optical force model will be described, including a particular case of this model, the ideal, perfectly reflective sail model.

#### Optical force model

The optical force model accounts for the optical properties of the sail to characterise the force generated by SRP. The total force acting on the sail can be decomposed into three force components, each associated to a distinct optical property of the sail film: absorptance, $\tilde{a}$; reflectance, $\tilde{r}$; and emissivity, $\tilde{e}$.

$$\mathbf{f} = \mathbf{f}_{\tilde{a}} + \mathbf{f}_{\tilde{r}} + \mathbf{f}_{\tilde{e}} \tag{2.10}$$

Here, $\tilde{a}$ and $\tilde{r}$ represent the fractions of photons that are absorbed and reflected by the sail surface, respectively. These coefficients allow to define a relation that describes how the total number of photons incident on the sail is partitioned among reflection, absorption, and transmission.

$$\tilde{a} + \tilde{r} + \tilde{\tau} = 1 \tag{2.11}$$

Here, $\tilde{\tau}$ denotes the fraction of photons that are transmitted through the sail without interacting with it in terms of momentum transfer. Assuming no transmission ($\tilde{\tau} = 0$), which could occur due to part of the

film tearing apart or intentionally in more novel approaches to solar-sail technology [29], the absorption coefficient can be expressed as a function of the reflection coefficient.

$$\tilde{a} = 1 - \tilde{r} \tag{2.12}$$

Equation (2.9) showed that the SRP depended on the projected area of the body under consideration, in this case the solar sail, perpendicular to the direction of the incident sunlight. Therefore, it is clear that the force generated by the sail depends on its orientation with respect to the direction of solar radiation. Figure 2.1 depicts a representation of the vectors and angles involved in a two-dimensional formulation of the solar-sail force model. The unit vectors $\mathbf{u}$ and $\mathbf{s}$ denote the incident sunlight and its specular reflection on the sail, respectively. Vectors $\mathbf{n}$ and $\mathbf{t}$ define the normal and tangential directions to the sail, while $\mathbf{m}$ represents the direction of the total force due to SRP acting on the sail. The angle $\alpha$, referred to as the cone angle, quantifies the orientation of the sail with respect to the incident radiation as the angle between the incoming sunlight and the sail normal. Finally, angle $\tilde{\phi}$ defines the direction of the total SRP force vector $\mathbf{m}$ with respect to the sail normal vector $\mathbf{n}$.

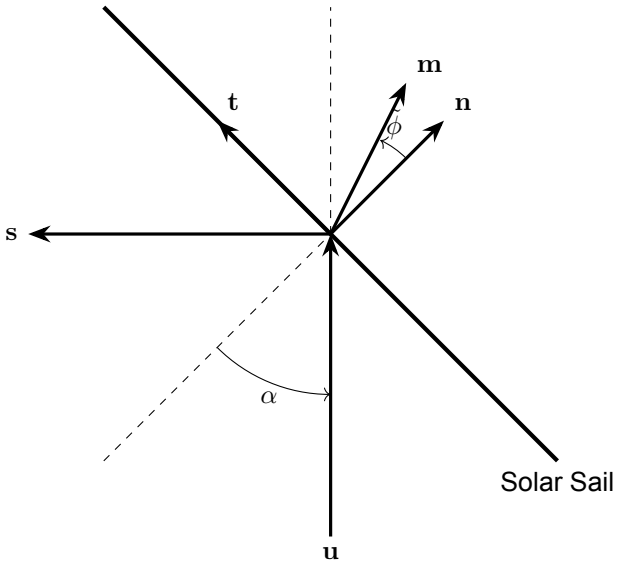


**Figure 2.1:** Representation of the vectors and angles involved in a two-dimensional formulation of the solar-sail force model.

Having established the geometric setup, it is now possible to express the incident and reflected directions in terms of the orientation of the sail.

$$\mathbf{u} = \cos\alpha\mathbf{n} + \sin\alpha\mathbf{t} \tag{2.13}$$

$$\mathbf{s} = -\cos\alpha\mathbf{n} + \sin\alpha\mathbf{t} \tag{2.14}$$

To derive the expression of the force exerted on the sail due to SRP, consider the case on which every photon is absorbed. This results in a unidirectional momentum transfer along the direction of the incoming radiation.

$$\mathbf{f}_{\tilde{a}} = PA\cos\alpha\mathbf{u} = PA\left(\cos^2\alpha\mathbf{n} + \cos\alpha\sin\alpha\mathbf{t}\right) \tag{2.15}$$

Equation (2.15) corresponds to the lower bound of solar-sail performance, as it yields the minimum attainable force due to the lack of reflection. This minimum force depends on the cone angle, $\alpha$, which is maximum for a sail orientated perpendicular to the sunlight direction, given for a cone angle of $\alpha = 0°$. Now, consider the case where a fraction $\tilde{r}$ of photons is reflected. Of these, a proportion $s$ undergoes specular reflection, resulting in a momentum transfer given by:

$$\mathbf{f}_{\tilde{r}s} = -\tilde{r}sPA\cos\alpha\mathbf{s} = \tilde{r}sPA\left(\cos^2\alpha\mathbf{n} - \cos\alpha\sin\alpha\mathbf{t}\right) \tag{2.16}$$

The remaining fraction of reflected photons, $\overline{s} = (1 - s)$, undergoes non-specular reflection, leading to exerting a force as follows.

$$\mathbf{f}_{\tilde{r}\overline{s}} = B_f\tilde{r}\left(1 - s\right)PA\cos\alpha\mathbf{n} \tag{2.17}$$

In Eq. (2.17), $B_f$ alludes to the non-Lambertian properties of the front solar-sail surface, which cause the light not to always reflect specularly, leading to variations in brightness across the surface [30]. The total force due to reflection results from adding Eqs. (2.16) and (2.17).

$$\mathbf{f}_{\tilde{r}} = \mathbf{f}_{\tilde{r}s} + \mathbf{f}_{\tilde{r}\overline{s}} = PA\left[\left(\tilde{r}s\cos^2\alpha + B_f\left(1-s\right)\tilde{r}\cos\alpha\right)\mathbf{n} - \tilde{r}s\cos\alpha\sin\alpha\mathbf{t}\right] \tag{2.18}$$

Finally, the last component of the force to be determined is the force caused by the emission of photons as thermal radiation from both front and back surfaces of the sail. According to the Stephan-Boltzmann law, the radiant flux emitted per unit area, $\tilde{M}$, is a function of the surface temperature, $T$, and the material emissivity, $\tilde{e}$.

$$\tilde{M} = \tilde{e}\tilde{\sigma}T^4 \tag{2.19}$$

Here, $\tilde{\sigma}$ refers to the Stephan-Boltzmann constant. Assuming a constant temperature distribution across the sail and both sail surfaces to be non-Lambertian, the force acting on the sail due to emission is given by:

$$\mathbf{f}_{\tilde{e}} = \frac{\tilde{M}_f B_f - \tilde{M}_b B_b}{c} A\mathbf{n} = \frac{\tilde{\sigma}T^4}{c} A\left(\tilde{e}_f B_f - \tilde{e}_b B_b\right)\mathbf{n} \tag{2.20}$$

The sub-indices $f$ and $b$ refer to the front and back surfaces, respectively. In Eq. (2.20), the temperature of the sail, $T$, is the only unknown variable, thus it needs to be determined. This can be achieved by applying the condition of thermal equilibrium to the sail. The thermal output, representing the heat radiated away from the sail, is governed by the thermal emission from both the front and back surfaces of the sail.

$$\Phi_{out} = \left(\tilde{e}_f + \tilde{e}_b\right)\tilde{\sigma}T^4 \tag{2.21}$$

Here, $\Phi_{out}$ represents the thermal output. The thermal input, $\Phi_{in}$, can be expressed as a function of the absorbed solar flux.

$$\Phi_{in} = \left(1-\tilde{r}\right)W\cos\alpha = \left(1-\tilde{r}\right)cP\cos\alpha \tag{2.22}$$

Equations (2.21) and (2.22) allow to determine the temperature of the sail by applying the thermal equilibrium condition, which requires that the thermal output equals the thermal input.

$$\Phi_{out} = \Phi_{in} \quad \Rightarrow \quad T_{eq} = \left[\frac{\left(1-\tilde{r}\right)cP\cos\alpha}{\left(\tilde{e}_f + \tilde{e}_b\right)\tilde{\sigma}}\right]^{\frac{1}{4}} \tag{2.23}$$

Substituting the equilibrium temperature in Eq. (2.23) into Eq. (2.20) yields an expression in the format of those from Eqs. (2.15) and (2.18), with the emissive force formulated as a function of the SRP.

$$\mathbf{f}_{\tilde{e}} = PA\left(1-\tilde{r}\right)\frac{\tilde{e}_f B_f - \tilde{e}_b B_b}{\tilde{e}_f + \tilde{e}_b}\cos\alpha\mathbf{n} \tag{2.24}$$

Equations (2.15), (2.18) and (2.24) allow to determine an expression of the total force acting on the sail due to SRP, which can be decomposed into its normal and tangential components.

$$\mathbf{f}_n = PA\left[\left(1+\tilde{r}s\right)\cos^2\alpha + B_f\left(1-s\right)\cos\alpha + \left(1-\tilde{r}\right)\frac{\tilde{e}_f B_f - \tilde{e}_b B_b}{\tilde{e}_f + \tilde{e}_b}\cos\alpha\right]\mathbf{n} \tag{2.25}$$

$$\mathbf{f}_t = PA\left(1-\tilde{r}s\right)\cos\alpha\sin\alpha\mathbf{t} \tag{2.26}$$

Having the normal and tangential components, the total force can be expressed as follows.

$$\mathbf{f} = \mathbf{f}_n + \mathbf{f}_t = f\mathbf{m} \quad \textit{where} \quad f = \sqrt{f_n^2 + f_t^2} \tag{2.27}$$

Furthermore, the angle $\tilde{\phi}$ can be determined.

$$\tilde{\phi} = \tan\left(\frac{f_t}{f_n}\right) \tag{2.28}$$

### Ideal Sail

The concept of an ideal sail is defined by a perfectly reflective sail. In this case, all incident photons are specularly reflected, implying that the total force acting on the sail due to SRP arises exclusively from specular reflection. This condition can be expressed by means of the coefficients defined before.

$$\begin{aligned} \tilde{r} &= 1 \qquad \tilde{e}_f = 0 \qquad B_f = 2/3 \\ s &= 1 \qquad \tilde{e}_b = 0 \qquad B_b = 2/3 \end{aligned} \tag{2.29}$$

Substituting the coefficients in Eq. (2.29) into Eqs. (2.25) and (2.26) yields the expressions for the force components along the sail normal and tangential directions generated by an ideal sail.

$$\mathbf{f}_n = 2PA\cos^2\alpha\mathbf{n} \tag{2.30}$$

$$\mathbf{f}_t = \mathbf{0} \tag{2.31}$$

Given that no photon undergoes non-specular reflection, the total force acting on the sail due to SRP lies along the sail normal direction.

$$\mathbf{f} = 2PA\cos^2\alpha\mathbf{n} \tag{2.32}$$

In Subsections 2.1.1 and 2.1.2, the concepts of characteristic acceleration $a_c$ and lightness number $\beta$ were introduced as metrics used to characterise the performance of a solar sail. Additionally, the concept of sail loading $\sigma$ was presented in Subsection 2.1.2. Using Eq. (2.32) as a starting point, the effect of characteristic acceleration, lightness number, and sail loading on the acceleration experienced by an ideal solar sail under SRP is examined. For the force model in Eq. (2.32), the resulting acceleration is given by:

$$\mathbf{a} = 2P\frac{A}{m}\cos^2\alpha\mathbf{n} \tag{2.33}$$

Defining the sail loading as $\sigma = \frac{m}{A}$, Eq. (2.33) can be reformulated in terms of $\sigma$.

$$\mathbf{a} = 2P\frac{1}{\sigma}\cos^2\alpha\mathbf{n} \tag{2.34}$$

Equation (2.34) shows that lower values of sail loading result in higher accelerations experienced by the sail, highlighting the importance of minimising the mass-to-area ratio to enhance propulsion efficiency. The characteristic acceleration is defined as the acceleration experienced by the sail due to SRP when oriented normal to sunlight at a distance of one AU from the Sun. To compute this value, it is required to express the acceleration in Eq. (2.34) as a function of the sail heliocentric distance. Substituting the expression for SRP from Eq. (2.9) into Eq. (2.34) yields the following relation for the acceleration of an ideal sail:

$$\mathbf{a} = \frac{L_\odot}{2\pi c}\frac{1}{\sigma}\frac{1}{r^2}\cos^2\alpha\mathbf{n} \tag{2.35}$$

Substituting the conditions on sail orientation and sail heliocentric distance given by the definition of characteristic acceleration on Eq. (2.35) yields an expression for $a_c$.

$$a_c = \frac{L_\odot}{2\pi c}\frac{1}{\sigma}\frac{1}{r_E^2} = \frac{2\tilde{W}_E}{c\sigma} \tag{2.36}$$

In Eq. (2.36), $r_E$ denotes Earth's mean heliocentric distance (1 AU) and $\tilde{W}_E$ represents the solar flux at this distance, as defined in Eq. (2.8). From Eq. (2.36) it can be deduced that the only sail parameter influencing the characteristic acceleration is the sail loading, $\sigma$.

Finally, to derive the expression for the lightness number, it is necessary to incorporate the Sun's point-mass gravitational acceleration into the expression. This can be achieved by multiplying and dividing Eq. (2.35) by the gravitational parameter of the Sun, $Gm_\odot$, where $G$ is the gravitational constant and $m_\odot$ denotes the solar mass. This manipulation enables the acceleration due to SRP to be expressed relative to the Sun's gravitational acceleration, $\frac{Gm_\odot}{r^2}$.

$$\mathbf{a} = \beta\frac{Gm_\odot}{r^2}\cos^2\alpha\mathbf{n} \tag{2.37}$$

The value of the lightness number $\beta$ in Eq. (2.37) is given by:

$$\beta = \frac{\sigma^*}{\sigma} \quad \textit{where} \quad \sigma^* = \frac{L_\odot}{2\pi G m_\odot c} \tag{2.38}$$

Here, $\sigma^*$ denotes the critical solar-sail loading, which depends solely on solar luminosity and mass. Once again, the dependency on the sail loading can be observed in Eq. (2.38), following the same inverse relation shown in Eq. (2.36) for the characteristic acceleration.

### 2.1.6. Locally Optimal Control Laws

The optimal control problem for a solar-sail trajectory consists of determining the time history of the sail attitude that maximises (or minimises) a specified performance index, such as time of flight, final orbital energy, or propellant mass savings in hybrid systems. Fully optimal solutions to such problems, obtained through direct or indirect optimal control methods, are capable of delivering globally optimal trajectories but are computationally intensive, particularly when embedded within iterative design processes or global search frameworks [1, 31].

Locally optimal control laws (LOCLs) provide an attractive alternative by prescribing the instantaneous sail orientation that optimises a local performance metric, typically the rate of change of a chosen orbital element or energy function, without regard for the entire future trajectory [1, 32]. These laws are derived by maximising (or minimising) the instantaneous variation of a selected quantity under the constraints of the sail dynamics, often using the Gaussian form of variational equations or other formulations for the rate of the orbital elements. Because they only require the current state vector and a small number of analytical expressions, LOCLs are extremely efficient to evaluate.

LOCLs have been developed for a variety of solar-sail mission scenarios. In the heliocentric case, classic examples include control laws for rapid changes in orbital angular momentum or inclination, constant cone-angle spirals, and time-optimal transfers under simplified SRP models [1]. In the planet-centred context, Macdonald and McInnes [31] derived analytical steering laws for geocentric solar sailing, enabling station-keeping, secular changes in argument of perigee, and other mission types without requiring numerical optimisation. More recently, Carzana et al. [32] extended LOCLs concepts to fully three-dimensional transfers and included atmospheric drag in the acceleration model.

This computational efficiency comes at the expense of global optimality: the trajectories produced by LOCLs are generally inferior to those obtained from full optimal control for the same problem definition. Nevertheless, the reduction in computational effort can be substantial, making them particularly well suited for applications where numerous candidate trajectories must be evaluated rapidly. As such, LOCLs have clear relevance for preliminary mission design and early-phase trade-space exploration.

## 2.2. Analytical Trajectory Prediction

This section examines the applicability of analytical models for trajectory prediction and demonstrates how such models can be employed for analytical planet-centred solar-sail trajectory prediction. Subsection 2.2.1 introduces the dynamical framework of a general perturbed TBP, highlighting the necessity of integrating the equations of motion. In Subsection 2.2.2 numerical integration methods are introduced. A distinction between the approaches to equation integration in preliminary and detailed mission design phases is outlined in Subsection 2.2.3, where potential applications of analytical trajectory prediction are also discussed. Finally, Subsection 2.2.4 presents various analytical formulations found in the literature, with particular emphasis on those tailored to solar-sailing missions.

### 2.2.1. Dynamical Model of the Perturbed Two-Body Problem

This subsection introduces the dynamical model of a generic perturbed TBP, defined as a TBP that is subjected to external perturbative acceleration. These perturbations may arise from sources such as the oblateness of the central body, third-body gravitational effects, or SRP. The nature and magnitude of the perturbation generally depends on both the perturbing source and the dynamical state of the orbiting body. The equations of motion governing a generic perturbed TBP are given by:

$$\begin{aligned} \dot{\mathbf{r}} &= \mathbf{v} \\ \dot{\mathbf{v}} &= -\frac{\mu}{r^3}\mathbf{r} + \mathbf{a}_p\left(\mathbf{r}, \mathbf{v}, \tilde{\mathbf{p}}\right) \end{aligned} \tag{2.39}$$

In Eq. (2.39), $\mathbf{r}$ and $\mathbf{v}$ denote the position and velocity vector of the orbiting body, respectively, $\mu$ corresponds to the standard gravitational parameter of the central body, and $\mathbf{a}_p$ represents the perturbing acceleration, which depends on the state of the orbiting body and a series of parameters $\tilde{\mathbf{p}}$ associated with the specific perturbation. For instance, in the case of a solar sail subjected to SRP, the vector $\tilde{\mathbf{p}}$ includes the solar luminosity, the position of the Sun relative to the orbiting body, and sail-specific properties such as the sail loading and orientation.

The equations of motion presented in Eq. (2.39) are, in general, non-integrable. Only three classical problems in celestial mechanics are known to admit closed-form analytical solutions: the Kepler problem [33], the two-fixed centres problem [34], and the Stark problem [35]. For all other cases, including perturbed systems, obtaining a solution requires the application of numerical integration techniques.

### 2.2.2. Numerical Integration Methods

This subsection introduces the concept of numerical integration and provides an overview of the various types of numerical methods available. It also discusses the trade-offs involved in selecting integration parameters, which must balance accuracy, computational efficiency and stability.

Numerical integration refers to the collection of algorithms used to approximate the solution of ordinary differential equations (ODEs), such as the perturbed two-body equations in Eq. (2.39), when a closed-form solution is not available. At its core, a numerical integrator steps the system forward in time by generating successive estimates of the state vector $\tilde{\mathbf{x}} = [\mathbf{r}, \mathbf{v}]$ based on the governing ODE and the chosen discretization strategy [36, 37].

Methods for numerical integration can be classified according to various characteristics that govern their behaviour. One of the most fundamental distinctions is between fixed-step and variable-step schemes. Fixed-step integrators use a constant step size $\Delta t$ throughout the propagation. They are simple to implement and predictable in terms of computational workload, but may suffer from significant cumulative error if $\Delta t$ is too large, or inefficiency if $\Delta t$ must be chosen very small to capture rapid dynamics accurately [38, 39]. In contrast, variable-step integrators dynamically adapt the size of the step $\Delta t$ by estimating the local truncation error at each step, adjusting $\Delta t$ to maintain the error within the user-defined tolerances [36, 40]. This adaptivity enables greater efficiency in regions where the solution evolves slowly, permitting larger step sizes, and high accuracy when rapid changes occur, requiring smaller steps. However, variable-step methods introduce computational overhead due to error estimation and step-size control logic.

Numerical integrators may also be classified as explicit or implicit. Explicit methods, such as the classical Euler or Runge-Kutta schemes, compute the next state using only previously available information. They are straightforward to implement and computationally inexpensive per step, but can become unstable or require prohibitively small step sizes $\Delta t$ when applied to stiff problems [37, 38]. Implicit methods, on the other hand, involve solving one or more non-linear equations at each step, typically using root finding algorithms. While this increases the computational cost per step, it significantly improves stability and permits the use of larger $\Delta t$ in stiff regimes [36, 40].

Any choice of integrator entails a trade-off between accuracy and computational cost. Higher-order methods, such as high-order Runge-Kutta or Dormand-Prince schemes, achieve a given accuracy with larger step sizes, thereby reducing the total number of integration steps. However, each step incurs a higher computational cost due to additional function evaluations [36, 38]. In contrast, low-order methods, such as Euler or midpoint schemes, offer low per-step cost but require many more steps to reach comparable accuracy, which can result in longer total runtimes when high precision is needed [37]. Variable-step integrators can mitigate this trade-off by allocating computational effort adaptively, though the associated overhead must be justified by the complexity of the problem dynamics.

To conclude this subsection, the Euler method is illustrated as an example. The Euler scheme adapts the state of the system at each step as:

$$\tilde{\mathbf{x}}_{k+1} = \tilde{\mathbf{x}}_k + \Delta t \dot{\tilde{\mathbf{x}}}_k \tag{2.40}$$

Here, $\dot{\tilde{\mathbf{x}}}$ denotes the state derivative vector. Applied to the perturbed TBP in Eq. (2.39), the state

updates are given by:

$$\begin{aligned} \mathbf{r}_{k+1} &= \mathbf{r}_k + \Delta t \mathbf{v}_k \\ \mathbf{v}_{k+1} &= \mathbf{v}_k + \Delta t \left[ -\frac{\mu}{r_k^3} \mathbf{r}_k + \mathbf{a}_p \left( \mathbf{r}_k, \mathbf{v}_k, \tilde{\mathbf{p}}_k \right) \right] \end{aligned} \tag{2.41}$$

While trivial to implement and computationally inexpensive, the forward Euler method is only first-order accurate and exhibits substantial energy drift when applied to orbital problems, unless an extremely small time step $\Delta t$ is used [36, 38]. For long-term orbital propagation, higher-order methods, such as the fourth-order Runge-Kutta scheme, are typically preferred for accuracy and long-term stability.

### 2.2.3. Integration Strategies in Preliminary and Detailed Mission Design

This subsection examines integration strategies across the two major phases of space mission design: preliminary mission design and detailed mission design. Preliminary design aims to explore a broad design space to identify feasible mission architectures, trajectories, and system parameters that satisfy high-level requirements. This phase typically employs global search techniques, such as grid searches, genetic algorithms, and other heuristic optimisers, to investigate a wide variety of trajectory options and operational scenarios [41, 42]. Once promising candidate solutions are identified, the design process transitions into the detailed phase, where the focus shifts to refining and validating the selected concept through high-fidelity modelling, local optimisation and rigorous enforcement of constraints [42].

From a computational perspective, this distinction has direct implications for integrating the equations of motion. In detailed mission design, the objective is to obtain accurate, physically consistent solutions suitable for implementation and mission operations. This requires high-fidelity dynamical models, including relevant perturbations such as non-spherical gravity, third-body effects, and SRP, and the use of high-order numerical integration schemes with tight error tolerances [36, 41]. Runge-Kutta methods of high order or implicit integrators for stiff systems are often employed to ensure that local truncation errors remain negligible over long propagation intervals. Such accuracy is essential for manoeuvre optimisation, navigation filter tuning, and long-term stability analysis, as even small integration errors can accumulate to significant trajectory deviations or incorrect performance estimates [43].

In contrast, preliminary mission design aims to efficiently evaluate a large number of candidate solutions during the global search. Since each trajectory evaluation may require hundreds to thousands of integrations over the mission timeline, computational cost is a critical factor [42]. To reduce the runtime, preliminary analysis often employs lower-fidelity dynamical models, looser numerical tolerances, or simplified analytical approximations. Examples include Keplerian motion with impulsive manoeuvres, averaged equations of motion, or low-order numerical integration schemes [41, 43]. While such approximations introduce modelling and integration errors, they are acceptable at this stage because the objective is to identify promising regions of the design space for further refinement rather than produce final, flight-ready trajectories.

### 2.2.4. Analytical Models for Trajectory Prediction

Analytical trajectory-prediction models approximate the solution of the equations of motion through closed-form expressions or low-cost semi-analytical procedures; their principal appeal in the context of mission design is that they generally attain a very low per-evaluation cost compared with high-fidelity numerical propagation. In preliminary mission design, where global searches and optimisation loops evaluate very large numbers of candidate trajectories, this reduction in per-evaluation computational time can substantially increase both the breadth and resolution of the explored design space and thus improve the likelihood of finding high-quality initial guesses for later refinement [41, 42]. This subsection studies the state-of-the-art regarding analytical models for trajectory prediction, with particular emphasis on literature concerning solar sailing.

In astrodynamics, a common method employed to construct analytical approximations is through the use of perturbation methods. Perturbation methods develop the solution of the perturbed problem as a series expansion around the TBP solution; when the perturbation magnitude $\epsilon$ is small, $\epsilon \ll 1$, the expansion converges rapidly and yields accurate approximations with only a few terms [44, 45]. These approaches give rise to closed-form or semi-analytical propagators for a range of perturbations and are therefore natural candidates for use in rapid analyses in the preliminary design phase.

The literature provides mature analytical treatments for several important perturbation classes. The $J_2$ problem has been extensively treated for both single-satellite [46, 47, 48, 49, 50, 51] and relative motion problems [52, 53, 54]. Atmospheric drag and third-body perturbations have likewise received analytical and semi-analytical attention in contexts where these effects are dominant [55, 56, 57, 58, 59].

When it comes to solar-sail dynamics, they have been mainly studied in the heliocentric context. The simplest formulation considers purely radial acceleration, which can be modelled as a modification of the solar gravitational parameter, yielding exact conic-trajectory solutions [1]. Several works have applied linear perturbation methods around the two-body problem, treating the SRP acceleration as a small perturbation to derive analytical approximations of heliocentric solar-sailing trajectories [60, 61]. An alternative line of research employs shape-based approaches, most commonly assuming spiral trajectories. Within this framework, exact solutions have been obtained for the purely radial case [62], while other studies have introduced approximations to generalise the motion to constant, non-radial pitch angles [1, 63], and even to fully three-dimensional configurations [64, 65].

By contrast, planet-centred solar-sailing trajectories pose distinct analytical challenges and remain comparatively underrepresented in the literature. The first analytical treatment of a planet-bound satellite subjected to SRP was provided by Isayev [66], who employed analytical mechanics under the simplifying assumptions of constant perturbing force magnitude and fixed direction. In the solar-sailing context, these assumptions correspond to maintaining a constant cone angle and neglecting variations in the Sun-satellite distance over the bounded planetary orbit.

The general problem of a two-body system perturbed by a constant-magnitude, constant-direction force, known as the Stark problem, was originally studied by Lagrange [67] and later identified as a feasible framework for modelling planet-centred solar sailing by McInnes [1]. Kirchgraber [68] first considered the application of the Stark model to astrodynamics, after which Rufer [69] investigated its use in low-thrust trajectory optimisation. Subsequent work by Lantoine and Russell [35] advanced this line of research, culminating in the derivation of complete closed-form solutions for both two- and three-dimensional cases [70]. Later, Hatten et al. [71] extended the Stark model to incorporate time-varying perturbations, specifically $J_2$ and atmospheric drag, and compared its performance to classical numerical integration methods. They concluded that within certain regions of the accuracy-efficiency trade-off space, the Stark model demonstrated superior performance relative to conventional numerical integrators.

Alternative formulations of the Stark problem have also been developed, including the Weierstrass formalism [72] and the F & G Taylor series approach [73]. A comparative assessment of these methods (see Table 2.2) is presented by Hatten et al. [74], with [73] exhibiting superior computational performance due to the avoidance of Jacobi [35] or Weierstrass [72] elliptic function evaluations, which otherwise yield semi-analytical solutions. In the case of Jacobi elliptic functions, which have been the most extensively applied in this context, several computation strategies exist [75], with the arithmetic-geometric mean method generally preferred [76]. Nevertheless, expansion-based acceleration techniques have been proposed [77, 78], offering potential reductions in computational effort for analytical propagation schemes.

**Table 2.2:** Summary of Stark problem solution techniques [74].

| | **Jacobi elliptic** | **Weierstrass elliptic** | ***F & G* Taylor series** |
|---|---|---|---|
| **Relative execution speed** | Medium | Slow | Medium to fast, depending on number of terms used |
| **Relative code file size** | Medium | Small | Large |
| **Required capabilities** | Elliptic integrals of the first, second, and third kinds; Jacobi elliptic functions | Weierstrass elliptic functions; complex arithmetic | Initial use of symbolic manipulator to derive coefficients |
| **Primary sources of inaccuracy** | Calculation of Jacobi elliptic functions and other transcendental functions; inversion of Stark equation | Calculation of Weierstrass elliptic functions and other transcendental functions; inversion of Stark equation | Truncation error due to large step sizes |

# 3

# Research Objective

This chapter motivates the research objective by synthesising the literature surveyed in Chapter 2 and identifying a specific gap concerning the application of the Stark model to planet-centred solar-sail trajectories.

While historically the focus has been on heliocentric solar sailing, planet-centred solar sailing is an increasingly relevant concept due to the exploitation of SRP for sustained non-Keplerian behaviour in Earth-centred applications. These include displaced orbits, pole-sitter concepts, orbit precession for persistent coverage, and propellantless station-keeping, which complement the more widely studied heliocentric use cases [1, 24, 25].

For mission design, particularly in preliminary design phases and global trade-space exploration, analytical and semi-analytical models may offer compelling computational advantages. They can reduce the per-evaluation cost of trajectory propagation and steering-law evaluation, enabling larger parameter sweeps and faster optimisation loops compared to brute-force numerical propagation [41, 42, 44]. The Stark model provides a convenient analytical framework, capturing first-order deviations from Keplerian motion while admitting closed- or semi-closed-form solutions [35, 72, 73].

Early analytical work applied constant-acceleration models to SRP in a planet-centred context: Isayev derived analytical expressions for a constant-force, constant-direction perturbation and presented a numerical example within the SRP framework [66]. Subsequent developments of the Stark formalism have focused on mathematical formulation and computational strategies [35, 72, 73], predominantly treating it as a canonical dynamical problem. Later, Hatten et al. studied the application of the Stark model to time-varying perturbations and concluded that, in certain regions of the accuracy-efficiency trade-off space, the Stark model could outperform classical numerical integration methods [71].

In addition, Hatten et al. [74] conducted a comparison of the main solution techniques for the Stark problem (see Table 2.2). Among these, the F & G Taylor series approach [73] exhibited superior performance due to the avoidance of semi-analytical elliptic function evaluations, but its series-expansion formulation requires small step sizes to limit truncation errors. In contrast, closed-form solutions derived from analytical mechanics capture the dynamics exactly and are therefore more appropriate as a first step in assessing the Stark model for solar-sailing applications. Between the closed-form options, Hatten et al. [74] found that the Jacobi elliptic solution [35] consistently outperformed the Weierstrass elliptic solution [72]. For this reason, the Jacobi elliptic formulation is adopted in this thesis.

The research gap is therefore twofold and specific. First, although Isayev demonstrated the applicability of constant-acceleration models to SRP, the analysis remains limited and largely illustrative [66]. Second, while Hatten et al. extended the Stark model to time-varying perturbations, its application to planet-centred solar sailing remains unexplored [71]. Consequently, the literature lacks a comprehensive study that evaluates the performance of the Stark model relative to conventional numerical integration methods under different solar-sail control laws. Furthermore, no sensitivity analysis exists that explores how the model behaves across relevant ranges of sail and orbital parameters. To the

best of the author's knowledge, no study quantifies the trade-off between model accuracy and computational efficiency as a function of control law type, lightness number, and orbital regime in the context of planet-centred solar sailing.

Based on this identified gap, the research objective and research question are presented below.

## Research Objective

*Investigate the performance, in terms of accuracy and computational cost, of the Stark model in the context of a controlled solar sail orbiting around Earth, under the effect of point-mass gravity and solar radiation pressure, for different simulation scenarios.*

## Research Question

*Can the Stark model serve as a reliable alternative to numerical integration methods for preliminary design of controlled solar-sail trajectories around Earth under the effect of point-mass gravity and solar radiation pressure?*

1. How does the performance of the Stark model compare to numerical integration methods when simulating solar-sail trajectories governed by a constant control law?
2. How does the performance of the Stark model compare to numerical integration methods when simulating solar-sail trajectories governed by time-varying locally optimal control laws?
3. How does the solar-sail lightness number affect the performance of the Stark model?
4. How do orbit parameters affect the performance of the Stark model?

# 4

# Dynamical Model

This chapter presents the dynamical model adopted for the study. Section 4.1 introduces the reference frames employed. Section 4.2 describes the acceleration model together with the assumptions made. Finally, the planet-centred solar-sail LOCLs for the increase of the orbital elements are detailed in Section 4.3.

## 4.1. Reference Frames

This section describes the reference frames used in the analysis. Specifically, the Earth Centred Inertial (ECI) frame in Subsection 4.1.1, the Stark Earth Centred Inertial (SECI) frame in Subsection 4.1.2, and the Radial-AlongTrack-CrossTrack (RSW) frame in Subsection 4.1.3.

### 4.1.1. Earth Centred Inertial

The ECI reference frame, $O_{xyz}$, is defined with its origin $O$ located at the centre of mass of the Earth and three non-rotating axes $\hat{\mathbf{x}}$, $\hat{\mathbf{y}}$, and $\hat{\mathbf{z}}$ (see Fig. 4.1). The $\hat{\mathbf{x}}$-axis is oriented along the Sun-Earth direction, pointing away from the Sun. The $\hat{\mathbf{y}}$-axis lies in the Ecliptic Plane, perpendicular to $\hat{\mathbf{x}}$ and oriented in the prograde direction. The $\hat{\mathbf{z}}$-axis is defined as the cross product of $\hat{\mathbf{x}}$ and $\hat{\mathbf{y}}$, completing a right-handed trihedron.

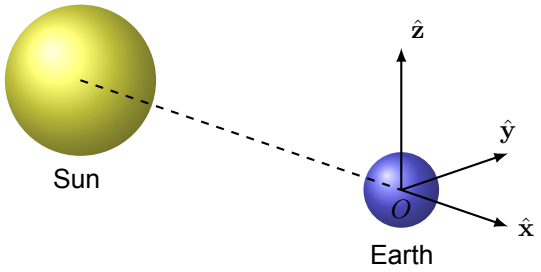


**Figure 4.1:** ECI reference frame.

### 4.1.2. Stark Earth Centred Inertial

The SECI reference frame, $O_{x_s y_s z_s}$, is an inertial reference frame with origin $O$ at the centre of mass of the Earth and three non-rotating axes $\hat{\mathbf{x}}_s$, $\hat{\mathbf{y}}_s$ and $\hat{\mathbf{z}}_s$ (see Fig. 4.2). This reference frame is required to perform the transformation between the coordinates employed in the Stark model and those of the ECI reference frame. The $\hat{\mathbf{x}}_s$-axis is aligned with the normal vector of the sail $\mathbf{n}$. The $\hat{\mathbf{z}}_s$-axis is defined as the normalised cross product between the ECI $\hat{\mathbf{x}}$-axis and $\hat{\mathbf{x}}_s$, $\hat{\mathbf{z}}_s = \frac{\hat{\mathbf{x}} \times \hat{\mathbf{x}}_s}{||\hat{\mathbf{x}} \times \hat{\mathbf{x}}_s||}$. Finally, the $\hat{\mathbf{y}}_s$-axis is defined as orthogonal to both $\hat{\mathbf{x}}_s$ and $\hat{\mathbf{z}}_s$, completing a right-handed orthogonal trihedron.

In Fig. 4.2, angles $\alpha$ and $\delta$ correspond to the cone and clock angles of a 3D solar-sail acceleration model, respectively. Using these angles, the rotation between the ECI and SECI reference frames can

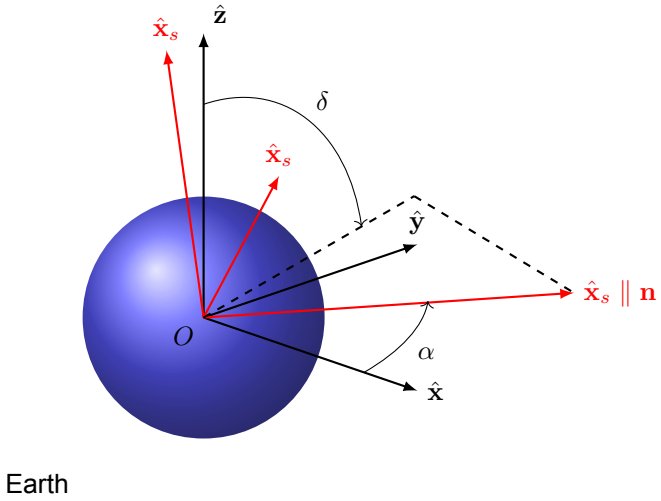


**Figure 4.2:** SECI reference frame.

be expressed as

$$\hat{\mathbf{x}}_s = R^{ECI}_{SECI}\hat{\mathbf{x}} \quad \textit{where} \quad R^{ECI}_{SECI} = \begin{bmatrix} \cos\alpha & \sin\alpha\sin\delta & \sin\alpha\cos\delta \\ -\sin\alpha & \cos\alpha\sin\delta & \cos\alpha\cos\delta \\ 0 & -\cos\delta & \sin\delta \end{bmatrix} \tag{4.1}$$

where $R^{ECI}_{SECI}$ denotes the rotation matrix from ECI to SECI. This transformation consists of a rotation by $\delta$ about the $\hat{\mathbf{x}}$-axis, followed by a rotation by $\alpha$ about the $\hat{\mathbf{z}}_s$-axis.

It must be noted that the angle $\alpha$ in this formulation does not exactly correspond to the geometric cone angle of the solar sail. The discrepancy arises because the cone angle is defined with respect to the Sun-satellite direction, rather than the Sun-Earth direction. Figure 4.3 illustrates a two-dimensional scheme of this relationship, where the angle between the sail normal $\mathbf{n}$ and the $\hat{\mathbf{x}}$-axis is denoted by $\alpha'$, while the angle between the Sun-Earth line and the Sun-satellite line is denoted by $\Delta\alpha$.

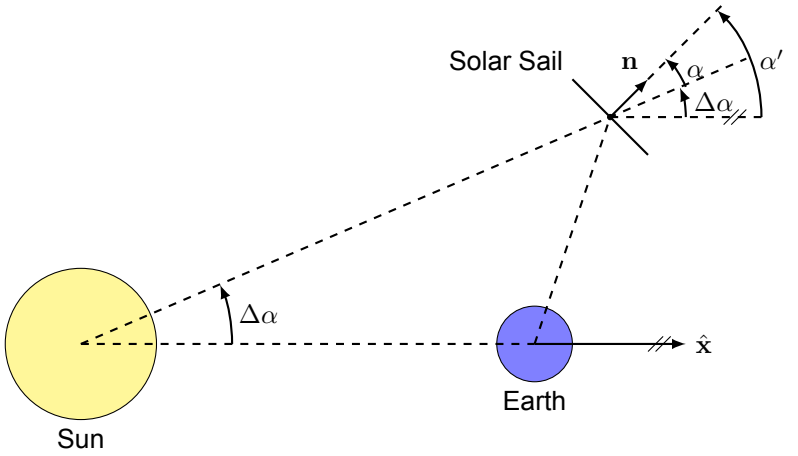


**Figure 4.3:** 2D scheme of the solar-sail cone angle.

In Fig. 4.3, the following relation holds:

$$\alpha' = \alpha + \Delta\alpha \tag{4.2}$$

Since $\Delta\alpha$ varies along the orbit, the magnitude of $\Delta\alpha$ must be bounded. For a circular orbit, the maximum value is given by:

$$\Delta\alpha = \arctan\left(\frac{r}{AU}\right) \tag{4.3}$$

For instance, $\Delta\alpha = 1°$ would require $r \approx 2600000$ km $\approx 8.5 r_{Moon}$. Therefore, it is reasonable to assume that for Earth-centred orbits, and particularly within the LEO environment, the value of $\Delta\alpha$ is negligible.

$$\Delta\alpha \ll 1 \quad \Rightarrow \quad \alpha' \approx \alpha \tag{4.4}$$

This derivation justifies the common assumption that all incoming solar rays are parallel to the $x$-axis. Consequently, angles $\alpha'$ and $\alpha$ will be treated interchangeably in the remainder of the work.

### 4.1.3. Radial-AlongTrack-CrossTrack

The RSW reference frame, $B_{RSW}$, is a body-fixed frame with origin $B$ located at the centre of mass of the solar sail and three moving axes $\hat{\hat{\mathbf{R}}}$, $\hat{\mathbf{S}}$ and $\hat{\mathbf{W}}$. The $\hat{\mathbf{R}}$-axis is aligned with the radial direction, pointing outward from the Earth:

$$\hat{\mathbf{R}} = \frac{\mathbf{r}}{r} \tag{4.5}$$

The $\hat{\mathbf{W}}$-axis is defined perpendicular to the orbital plane, oriented along the specific angular momentum vector:

$$\hat{\mathbf{W}} = \frac{\mathbf{r} \times \mathbf{v}}{||\mathbf{r} \times \mathbf{v}||} \tag{4.6}$$

Finally, the $\hat{\mathbf{S}}$-axis completes the right-handed trihedron:

$$\hat{\mathbf{S}} = \hat{\mathbf{W}} \times \hat{\mathbf{R}} \tag{4.7}$$

The RSW frame is particularly convenient for describing perturbing accelerations and control laws in orbital dynamics, as it is directly tied to the instantaneous orbital geometry.

## 4.2. Acceleration Model

This section introduces the acceleration model adopted for this study. The model is deliberately chosen as the simplest solar-sail acceleration formulation to enable a clear comparison between the Stark model and numerical propagation, while avoiding additional dynamical complexities. Accordingly, only Earth point-mass gravity and SRP accelerations are included. Additionally, some assumptions are considered:

- The Sun-sail distance is constant and equal to the mean Sun-Earth distance.
- The solar flux is modelled under the parallel-rays approximation.
- Orbital eclipses are neglected.
- The solar sail is considered ideal.

Under these assumptions, the SRP acceleration reduces to the expression in Eq. (2.37), where the Sun-sail distance $r$ is assumed constant and equal to one AU, $r = 1$ AU. Consequently, the magnitude of the SRP acceleration depends only on the sail lightness number, $\beta$, and on the sail orientation, defined by its cone angle $\alpha$. The direction of the SRP acceleration is aligned with the sail normal $\mathbf{n}$, whose orientation in a three-dimensional sail acceleration model is parameterized by the cone and clock angles, as defined in Subsection 4.1.2. Accordingly, the sail normal vector in the ECI frame is expressed as:

$$\mathbf{n} = \cos\alpha\hat{\mathbf{x}} + \sin\alpha\sin\delta\hat{\mathbf{y}} + \sin\alpha\cos\delta\hat{\mathbf{z}} \tag{4.8}$$

Substituting Eq. (4.8) into Eq. (2.37) yields the explicit expression for the SRP acceleration in the ECI frame. When combined with the Earth point-mass gravitational acceleration, the complete acceleration model in ECI coordinates is given by:

$$\begin{aligned}
\ddot{x} &= -\mu\frac{x}{r^3} + a_{SRP}\cos\alpha \\
\ddot{y} &= -\mu\frac{y}{r^3} + a_{SRP}\sin\alpha\sin\delta \\
\ddot{z} &= -\mu\frac{z}{r^3} + a_{SRP}\sin\alpha\cos\delta
\end{aligned} \tag{4.9}$$

In Eq. (4.9), $a_{SRP}$ denotes the magnitude of the SRP acceleration. Using the rotation matrix defined in Eq. (4.1), the equations of motion can be transformed into the SECI frame.

$$\begin{aligned} \ddot{x}_s &= -\mu \frac{x_s}{r^3} + a_{SRP} \\ \ddot{y}_s &= -\mu \frac{y_s}{r^3} \\ \ddot{z}_s &= -\mu \frac{z_s}{r^3} \end{aligned} \tag{4.10}$$

This formulation is identical in structure to the classical Stark problem, as will be shown later. In the SECI frame, for a given cone angle, the SRP perturbation is not only constant in magnitude but also fixed in direction, which are precisely the premises that allow the analytical integration of the model.

## 4.3. Planet-Centred Solar-Sail Locally Optimal Control Laws

This section describes the LOCLs introduced in Subsection 2.1.6. Consider the Lagrange variational equation for the rate of change of an orbital element $k$, which can be expressed as:

$$\frac{dk}{dt} = \mathbf{f} \cdot \boldsymbol{\lambda}_k \tag{4.11}$$

In Eq. (4.11), $\mathbf{f}$ represents the perturbing force due to SRP and $\boldsymbol{\lambda}_k$ a vector of functions of the orbital elements of the sail. The rate of change of $k$ is maximised when the projection $\mathbf{f} \cdot \boldsymbol{\lambda}_k$ is maximised. Dropping the subscript $k$ for simplicity, $\boldsymbol{\lambda}$ can be defined as a function of its own cone and clock angles, $\tilde{\alpha}$ and $\tilde{\delta}$.

$$\boldsymbol{\lambda} = \cos\tilde{\alpha}\hat{\mathbf{x}} + \sin\tilde{\alpha}\sin\tilde{\delta}\hat{\mathbf{y}} + \sin\tilde{\alpha}\cos\tilde{\delta}\hat{\mathbf{z}} \tag{4.12}$$

With the vector $\boldsymbol{\lambda}$ defined for a given state, the corresponding angles $\tilde{\alpha}$ and $\tilde{\delta}$ can be determined.

$$\begin{aligned} \tilde{\alpha} &= \arccos\lambda_x \\ \tilde{\delta} &= \arctan\left(\frac{\lambda_y}{\lambda_z}\right) \end{aligned} \tag{4.13}$$

To determine the actual cone and clock angles of the sail, the projection of the force onto the vector $\boldsymbol{\lambda}$ must be defined. Starting from Eq. (2.32), the projection $f_\lambda = \mathbf{f} \cdot \boldsymbol{\lambda}$ is given by:

$$f_\lambda = 2PA\cos^2\alpha\mathbf{n} \cdot \boldsymbol{\lambda} \tag{4.14}$$

Substituting Eqs. (4.8) and (4.12) into Eq. (4.14) yields the expression of the projection $f_\lambda$ as a function of the cone and clock angles from $\mathbf{n}$ and $\boldsymbol{\lambda}$.

$$f_\lambda = 2PA\cos^2\alpha\left[\cos\alpha\cos\tilde{\alpha} + \sin\alpha\sin\tilde{\alpha}\cos\left(\delta - \tilde{\delta}\right)\right] \tag{4.15}$$

From Eq. (4.15) it follows that the projection $f_\lambda$ is maximised when $\delta = \tilde{\delta}$. Under this condition, the optimal value of $\alpha$ is obtained from $\frac{\partial f_\lambda}{\partial \alpha} = 0$. After some algebraic manipulations, the optimal cone and clock angles are given by:

$$\begin{aligned} \delta^* &= \tilde{\delta} \\ \alpha^* &= \arctan\left(\frac{-3\cos\tilde{\alpha} + \sqrt{9\cos^2\tilde{\alpha} + 8\sin^2\tilde{\alpha}}}{4\sin\tilde{\alpha}}\right) \end{aligned} \tag{4.16}$$

These analytical expressions depend solely on $\tilde{\alpha}$ and $\tilde{\delta}$, which in turn are functions of the spacecraft state at a given epoch and the selected orbital element, $k$. Table 4.1 lists the components of the vector $\boldsymbol{\lambda}$ in the RSW frame, obtained from the variational equations in [1], for each orbital element: semi-major axis (SMA), $a$; eccentricity, $e$; inclination, $i$; right ascension of the ascending node (RAAN), $\Omega$; and argument of periapsis, $\omega$. To determine the corresponding cone and clock angles of $\boldsymbol{\lambda}$, the components must be transformed from the RSW frame to the ECI frame before applying Eq. (4.13).

**Table 4.1:** Components of the vector $\boldsymbol{\lambda}$ in the RSW frame for the control laws corresponding to different orbital elements, derived from the variational equations in [1]. Here, $\theta$ denotes the true anomaly.

| **Orbital Element** | $\lambda_R$ | $\lambda_S$ | $\lambda_W$ |
|---|---|---|---|
| $a$ (SMA) | $e \sin\theta$ | $1 + e\cos\theta$ | $0$ |
| $e$ (Eccentricity) | $\sin\theta$ | $\cos\theta + \frac{e+\cos\theta}{1+e\cos\theta}$ | $0$ |
| $i$ (Inclination) | $0$ | $0$ | $\cos(\omega+\theta)$ |
| $\Omega$ (RAAN) | $0$ | $0$ | $\frac{\sin(\omega+\theta)}{\sin i}$ |
| $\omega$ (Argument of periapsis) | $-\cos\theta$ | $\left(1+\frac{1}{1+e\cos\theta}\right)\sin\theta$ | $-\frac{e\sin(\omega+\theta)\tan i}{1+e\cos\theta}$ |

# 5

# Stark Model

In this chapter, the three-dimensional formulation of the Stark model is derived using the Hamilton-Jacobi formalism, following the methodology presented in [70]. Section 5.1 introduces the Stark problem, including its governing equations of motion. The variable transformations required to render the system integrable are described in Section 5.2. Building on these transformations, Hamilton's principal function is formulated in Section 5.3, which forms the basis for obtaining closed-form solutions. Section 5.4 details the integration of the resulting equations of motion, while Section 5.5 summarises the different sets of solutions.

## 5.1. Stark Problem

The Stark problem is a specific instance of the perturbed TBP, as introduced in Eq. (2.39), in which the perturbing acceleration is constant in both magnitude and direction. Accordingly, the acceleration model of the Stark problem is formulated as the classical TBP augmented by a uniform acceleration, $\epsilon$, applied along a single coordinate axis:

$$\begin{aligned} \ddot{x} &= -\mu \frac{x}{r^3} \\ \ddot{y} &= -\mu \frac{y}{r^3} \\ \ddot{z} &= -\mu \frac{z}{r^3} + \epsilon \end{aligned} \tag{5.1}$$

Although Eq. (5.1) specifies the acceleration along the $z$-axis, any constant acceleration vector in $\mathbb{R}^3$ can be transformed into this canonical form by an appropriate rotation of the reference frame. This property underpins the generality of the Stark problem formulation and allows it to accommodate arbitrary constant perturbations within a unified analytical framework.

## 5.2. Variable Changes

This section introduces the transformations of variables required to enable the integration of the equations of motion in the Stark model. The formulation relies on two fundamental changes of variables. First, Subsection 5.2.1 presents the transformation of the state from Cartesian to parabolic coordinates, which provides a more natural framework for exploiting the structure of the Stark problem. Subsequently, Subsection 5.2.2 details the transformation of the independent variable, which is required to regularize the system and facilitate the integration of the resulting equations of motion.

### 5.2.1. State Variable Change

The state transformation employed in the Stark model relies on a change of variables from Cartesian to parabolic coordinates. This nonlinear transformation is particularly well suited to the problem due to the symmetry introduced by the constant perturbing acceleration. The forward transformation, from

parabolic coordinates to Cartesian coordinates, is defined as follows:

$$\begin{aligned} x &= \xi\eta\cos\phi \\ y &= \xi\eta\sin\phi \\ z &= \frac{1}{2}\left(\xi^2-\eta^2\right) \end{aligned} \quad \Rightarrow \quad \begin{aligned} \dot{x} &= \left(\dot{\xi}\eta+\xi\dot{\eta}\right)\cos\phi - \xi\eta\dot{\phi}\sin\phi \\ \dot{y} &= \left(\dot{\xi}\eta+\xi\dot{\eta}\right)\sin\phi + \xi\eta\dot{\phi}\cos\phi \\ \dot{z} &= \xi\dot{\xi}-\eta\dot{\eta} \end{aligned} \tag{5.2}$$

Equation (5.2) establishes the position and velocity components in Cartesian coordinates, $\tilde{\mathbf{x}}_{xyz} = [x, y, z, \dot{x}, \dot{y}, \dot{z}]$, as explicit functions of the parabolic state vector, $\tilde{\mathbf{x}}_{\xi\eta\phi} = \left[\xi, \eta, \phi, \dot{\xi}, \dot{\eta}, \dot{\phi}\right]$. The inverse transformation, which expresses the parabolic coordinates as a function of the Cartesian state, is given by:

$$\begin{aligned} \xi &= \sqrt{r+z} \\ \eta &= \sqrt{r-z} \\ \phi &= \arctan\left(\frac{x}{y}\right) \end{aligned} \quad \Rightarrow \quad \begin{aligned} \dot{\xi} &= \frac{\dot{r}+\dot{z}}{2\sqrt{r+z}} \\ \dot{\eta} &= \frac{\dot{r}-\dot{z}}{2\sqrt{r-z}} \\ \dot{\phi} &= \frac{x\dot{y}-\dot{x}y}{x^2+y^2} \end{aligned} \tag{5.3}$$

This transformation establishes the analytical foundation for reformulating the equations of motion of the Stark problem in parabolic coordinates, a step that is essential to obtaining an integrable representation through the Hamilton-Jacobi formalism.

### 5.2.2. Time Variable Change

The rationale for introducing a time variable transformation can be illustrated by considering the expression for the velocity, $v$, in parabolic coordinates. Using the transformation defined in Eq. (5.2), the squared velocity is given by:

$$v^2 = \dot{x}^2+\dot{y}^2+\dot{z}^2 = \left(\xi^2+\eta^2\right)\left(\dot{\xi}^2+\dot{\eta}^2\right) + \xi^2\eta^2\dot{\phi}^2 \tag{5.4}$$

From Eq. (5.4), it is apparent that the contributions of the $\xi$ and $\eta$ coordinates to the kinetic energy scale with $\left(\xi^2+\eta^2\right)$, whereas the contribution associated with the $\phi$ coordinate scales with $\xi^2\eta^2$. This observation motivates the introduction of the following time reparametrisations:

$$d\tau_1 = \frac{1}{\xi^2+\eta^2}dt \tag{5.5}$$

$$d\tau_2 = \frac{1}{\xi^2\eta^2}dt \tag{5.6}$$

Here, $\tau_1$ and $\tau_2$ represent the radial and azimuthal fictitious times, respectively. Transformations in Eqs. (5.5) and (5.6) regularise the equations of motion and simplify their subsequent integration, as will be detailed in Section 5.4.

## 5.3. Hamilton-Jacobi Formalism

This section approaches the integration of the equations of motion of the Stark problem, introduced in Eq. (5.1), within the framework of the Hamilton-Jacobi formalism. The objective is to construct Hamilton's principal function in a form that admits separation of variables, thereby enabling the integration of the equations of motion. In this formulation, the principal function can be expressed as the sum of component functions, each depending solely on a single coordinate. Derivations and statements regarding analytical mechanics concerns follow [79].

The starting point is the Hamilton-Jacobi equation, which establishes the relation between Hamilton's principal function, $S$, and the Hamiltonian, $H$, of the system:

$$H\left(\mathbf{q}, \mathbf{p}=\frac{\partial S}{\partial \mathbf{q}}, t\right) + \frac{\partial S}{\partial t} = 0 \quad \textit{where} \quad S = S\left(\mathbf{q}, \boldsymbol{\rho}, t\right) \tag{5.7}$$

In Eq. (5.7), $\mathbf{q}$ denotes the vector of generalised coordinates, $\mathbf{p}$ the vector of associated canonical momenta, and $\boldsymbol{\rho}$ a vector of constants of motion. To solve the Hamilton-Jacobi equation, it is first necessary to formulate the Hamiltonian, which is obtained from the Lagrangian of the system through:

$$H = \sum p_i \dot{q}_i \left(\mathbf{p}, \mathbf{q}, t\right) - L\left(\mathbf{q}, \dot{\mathbf{q}}\left(\mathbf{p}, \mathbf{q}, t\right), t\right) \tag{5.8}$$

Here, $L$ denotes the Lagrangian of the system. Since the Lagrangian is defined as the difference between the kinetic $\tilde{K}$ and potential $U$ energies, the first step is to express these quantities in parabolic coordinates. For the system governed by Eq. (5.1), they take the form:

$$\tilde{K} = \frac{1}{2}\left(\dot{x}^2 + \dot{y}^2 + \dot{z}^2\right) = \frac{1}{2}\left[\left(\xi^2 + \eta^2\right)\left(\dot{\xi}^2 + \dot{\eta}^2\right) + \xi^2\eta^2\dot{\phi}^2\right] \tag{5.9}$$

$$U = -\frac{\mu}{r} - \epsilon z = -\frac{2\mu}{\xi^2 + \eta^2} - \frac{1}{2}\epsilon\left(\xi^2 - \eta^2\right) \tag{5.10}$$

From these expressions, the Lagrangian is written as:

$$L = \tilde{K} - U = \frac{1}{2}\left[\left(\xi^2 + \eta^2\right)\left(\dot{\xi}^2 + \dot{\eta}^2\right) + \xi^2\eta^2\dot{\phi}^2\right] + \frac{2\mu}{\xi^2 + \eta^2} + \frac{1}{2}\epsilon\left(\xi^2 - \eta^2\right) \tag{5.11}$$

The canonical momenta are obtained as the partial derivatives of the Lagrangian with respect to the generalised coordinates:

$$p_\xi = \frac{\partial L}{\partial \xi} = \left(\xi^2 + \eta^2\right)\dot{\xi} \tag{5.12}$$

$$p_\eta = \frac{\partial L}{\partial \eta} = \left(\xi^2 + \eta^2\right)\dot{\eta} \tag{5.13}$$

$$p_\phi = \frac{\partial L}{\partial \phi} = \xi^2\eta^2\dot{\phi} \tag{5.14}$$

Equations (5.12), (5.13) and (5.14) highlight once more the motivation behind the time reparametrisation introduced in Subsection 5.2.2, as it simplifies the dependence of the momenta on the coordinates.

Finally, substituting the Lagrangian in Eq. (5.11) and the canonical momenta in Eqs. (5.12), (5.13) and (5.14) into Eq. (5.8), the Hamiltonian of the system can be expressed in terms of the generalised coordinates and their conjugate momenta as:

$$H = \frac{1}{2}\frac{p_\xi^2 + p_\eta^2}{\xi^2 + \eta^2} + \frac{1}{2}\frac{p_\phi^2}{\xi^2\eta^2} - \frac{2\mu}{\xi^2 + \eta^2} - \frac{1}{2}\epsilon\left(\xi^2 - \eta^2\right) \tag{5.15}$$

With the Hamiltonian expressed in this form, the Hamilton-Jacobi equation can now be solved by applying the separation of variables technique to determine Hamilton's principal function.

### Separation of variables on $t$

The Hamiltonian in Eq. (5.15) does not exhibit explicit dependence on the time variable $t$. Consequently, Hamilton's principal function can be separated into temporal and spatial components:

$$\frac{\partial H}{\partial t} = 0 \quad \Rightarrow \quad S\left(\mathbf{q}, \boldsymbol{\rho}, t\right) = S'\left(t, \boldsymbol{\rho}\right) + W\left(\mathbf{q}, \boldsymbol{\rho}\right) \tag{5.16}$$

In Eq. (5.16), the function $S'$ corresponds to the temporal contribution, whereas $W$ denotes the spatial part of Hamilton's principal function. Since the Hamiltonian is independent of time, it follows that the Hamiltonian is a constant of motion.

$$H = constant \tag{5.17}$$

Moreover, from Eq. (5.16), one finds $\frac{\partial S}{\partial t} = \frac{\partial S'}{\partial t}$. Substitution into the Hamilton-Jacobi equation and subsequent integration leads to the following explicit form of the temporal contribution:

$$S'\left(t, \boldsymbol{\rho}\right) = -H\left(t - t_0\right) \tag{5.18}$$

Here, $t_0$ corresponds to the initial condition of the time variable.

Separation of variables on $\phi$

An analogous approach applies to the azimuthal variable $\phi$. Since the Hamiltonian in Eq. (5.15) is independent of $\phi$, the spatial contribution $W$ can be further decomposed as:

$$\frac{\partial H}{\partial \phi} = 0 \quad \Rightarrow \quad W(\mathbf{p}, \boldsymbol{\rho}) = W'(\xi, \eta, \boldsymbol{\rho}) + W_\phi(\phi, \boldsymbol{\rho}) \tag{5.19}$$

Here, $W'$ and $W_\phi$ correspond to the radial and azimuthal contributions of Hamilton's principal function, respectively. The absence of $\phi$ in the Hamiltonian identifies it as a cyclic variable, implying that the corresponding canonical momentum is conserved.

$$p_\phi = constant \tag{5.20}$$

Recalling the definition $p_\phi = \frac{\partial S}{\partial \phi}$ and using $\frac{\partial S}{\partial \phi} = \frac{\partial W_\phi}{\partial \phi}$, the azimuthal part of the characteristic function is expressed as

$$W_\phi(\phi, \boldsymbol{\rho}) = p_\phi(\phi - \phi_0) \tag{5.21}$$

Here, $\phi_0$ corresponds to the initial condition for $\phi$ at $t_0$.

Separation of variables on $\xi$ and $\eta$

To obtain the separation of variables of $\xi$ and $\eta$ the process is different from the variables $t$ and $\phi$. Expanding the Hamiltonian from Eq. (5.15) in the Hamilton-Jacobi equation, substituting $\mathbf{p} = \frac{\partial S}{\partial \mathbf{q}}$, gives the following:

$$\frac{1}{2}\frac{1}{\xi^2+\eta^2}\left[\left(\frac{\partial S}{\partial \xi}\right)^2 + \left(\frac{\partial S}{\partial \eta}\right)^2\right] + \frac{1}{2}\frac{1}{\xi^2\eta^2}\left(\frac{\partial S}{\partial \phi}\right)^2 - \frac{2\mu}{\xi^2+\eta^2} - \frac{1}{2}\epsilon\left(\xi^2-\eta^2\right) + \frac{\partial S}{\partial t} = 0 \tag{5.22}$$

Substituting Eqs. (5.18) and (5.21) into Eq. (5.22) and applying the derivatives allows to rewrite the Hamilton-Jacobi equation as:

$$\frac{1}{2}\frac{1}{\xi^2+\eta^2}\left[\left(\frac{\partial W'}{\partial \xi}\right)^2 + \left(\frac{\partial W'}{\partial \eta}\right)^2\right] + \frac{1}{2}\frac{1}{\xi^2\eta^2}p_\phi^2 - \frac{2\mu}{\xi^2+\eta^2} - \frac{1}{2}\epsilon\left(\xi^2-\eta^2\right) - H = 0 \tag{5.23}$$

Multiplying both sides of Eq. (5.23) by $2\left(\xi^2+\eta^2\right)$ and performing some algebraic manipulation allows to reach the following:

$$\left(\frac{\partial W'}{\partial \xi}\right)^2 + \frac{p_\phi^2}{\xi^2} - 2\mu - \epsilon\xi^4 - 2H\xi^2 = -\left(\frac{\partial W'}{\partial \eta}\right)^2 - \frac{p_\phi^2}{\eta^2} + 2\mu - \epsilon\eta^4 + 2H\eta^2 \tag{5.24}$$

Here, the left side of the equation depends only on $\xi$, while the right side depends only on $\eta$. Because of this, the only possible solution for Eq. (5.24) is that both sides are equal and constant. Therefore, not only a third constant of motion is identified, but also $W'$ can be separated into two different functions.

$$g_1(\xi, \boldsymbol{\rho}) = g_2(\eta, \boldsymbol{\rho}) = \kappa = constant \quad \Rightarrow \quad W'(\xi, \eta, \boldsymbol{\rho}) = W_\xi(\xi, \boldsymbol{\rho}) + W_\eta(\eta, \boldsymbol{\rho}) \tag{5.25}$$

In Eq. (5.25), the expressions of $g_1(\xi)$ and $g_2(\eta)$ are given by:

$$\begin{aligned} g_1(\xi, \boldsymbol{\rho}) &= \left(\frac{\partial W_\xi}{\partial \xi}\right)^2 + \frac{p_\phi^2}{\xi^2} - 2\mu - \epsilon\xi^4 - 2H\xi^2 \\ g_2(\eta, \boldsymbol{\rho}) &= -\left(\frac{\partial W_\eta}{\partial \eta}\right)^2 - \frac{p_\phi^2}{\eta^2} + 2\mu - \epsilon\eta^4 + 2H\eta^2 \end{aligned} \tag{5.26}$$

From Eq. (5.26), functions $W_\xi$ and $W_\eta$ can be integrated independently.

$$W_\xi(\xi, \boldsymbol{\rho}) = \int_{\xi_0}^{\xi} \bar{\delta}_\xi \sqrt{\epsilon\xi^4 + 2H\xi^2 + (2\mu+\kappa) - \frac{p_\phi^2}{\xi^2}}\, d\xi \tag{5.27}$$

$$W_\eta(\eta, \boldsymbol{\rho}) = \int_{\eta_0}^{\eta} \bar{\delta}_\eta \sqrt{-\epsilon\eta^4 + 2H\eta^2 + (2\mu-\kappa) - \frac{p_\phi^2}{\eta^2}}\, d\eta \tag{5.28}$$

Here, $\bar{\delta}_\xi$ and $\bar{\delta}_\eta$ denote the undetermined signs of the square roots. These signs must be determined at a later stage, based on the initial conditions of the trajectory. Furthermore, $\xi_0$ and $\eta_0$ represent the initial conditions for $\xi$ and $\eta$ at $t_0$, respectively. Since the subsequent derivation of the equations of motion requires differentiating the expressions in Eqs. (5.27) and (5.28), it is sufficient to retain these expressions in their integral form at this stage.

#### Hamilton's principal function

The complete expression for Hamilton's principal function is given by a combination of functions, each depending solely on one variable.

$$S(\mathbf{q}, \boldsymbol{\rho}, t) = S'(t, \boldsymbol{\rho}) + W_\xi(\xi, \boldsymbol{\rho}) + W_\eta(\eta, \boldsymbol{\rho}) + W_\phi(\phi, \boldsymbol{\rho}) \tag{5.29}$$

Expressions for $S'$, $W_\xi$, $W_\eta$, and $W_\phi$ are given by Eqs. (5.18), (5.27), (5.28), and (5.21), respectively. Additionally, the vector of constants of motion $\boldsymbol{\rho}$ remains defined as:

$$\boldsymbol{\rho} = [H, p_\phi, \kappa] \tag{5.30}$$

## 5.4. Integration

This section is devoted to the integration of the equations of motion of the Stark problem. The procedure follows from the Hamilton-Jacobi formalism developed in Section 5.3, where Hamilton's principal function was obtained in separable form. Subsection 5.4.1 addresses the integration of the azimuthal coordinate $\phi$. Subsection 5.4.2 focuses on the integration of the radial parabolic coordinates $\xi$ and $\eta$. Subsequently, Subsection 5.4.3 concerns the integration of the azimuthal fictitious time variable $\tau_2$, establishing its relation to the radial fictitious time $\tau_1$. Finally, Subsection 5.4.4 performs the integration of $\tau_1$, yielding its connection with the physical time $t$.

### 5.4.1. Integration of $\phi$

The equations of motion for the state variables and, therefore, for coordinate $\phi$, follow from the fundamental relation between the canonical momenta and Hamilton's principal function.

$$\mathbf{p} = \frac{\partial L}{\partial \mathbf{q}} = \frac{\partial S}{\partial \mathbf{q}} \tag{5.31}$$

In the case of $\phi$, this relation can be expressed by combining the canonical momentum defined in Eq. (5.14) with the function $W_\phi$ in Eq. (5.21), which represents the component of Hamilton's principal function $S$ associated with the variable $\phi$. This leads to the following equation of motion in terms of the physical time $t$.

$$\xi^2 \eta^2 \frac{d\phi}{dt} = p_\phi \tag{5.32}$$

To facilitate the integration, the fictitious time variable $\tau_2$ is introduced as a substitute for the physical time $t$. Making use of the transformation between $\tau_2$ and $t$ provided in Eq. (5.6), Eq. (5.32) can be rewritten as:

$$\frac{d\phi}{d\tau_2} = p_\phi \tag{5.33}$$

Since $p_\phi$ is a constant of motion, the integration of Eq. (5.33) is trivial, yielding a closed-form expression for the evolution of $\phi$ as a function of $\tau_2$.

$$\phi = \phi_0 + p_\phi \tau_2 \tag{5.34}$$

### 5.4.2. Integration of $\xi$ and $\eta$

By combining the canonical momenta associated with $\xi$ and $\eta$, given in Eqs. (5.12) and (5.13), with the corresponding functions $W_\xi$ and $W_\eta$ defined in Eqs. (5.27) and (5.28), the general relation in Eq. (5.31) yields the equations of motion for $\xi$ and $\eta$ in terms of the physical time $t$.

$$\left(\xi^2 + \eta^2\right) \frac{d\xi}{dt} = \bar{\delta}_\xi \sqrt{\epsilon \xi^4 + 2H\xi^2 + (2\mu + \kappa) - \frac{p_\phi^2}{\xi^2}} \tag{5.35}$$

$$\left(\xi^2 + \eta^2\right) \frac{d\eta}{dt} = \bar{\delta}_\eta \sqrt{-\epsilon \eta^4 + 2H\eta^2 + (2\mu - \kappa) - \frac{p_\phi^2}{\eta^2}} \tag{5.36}$$

Analogous to the case of $\phi$, these expressions are simplified by introducing the fictitious time transformation between $\tau_1$ and $t$ defined in Eq. (5.5). This substitution eliminates the common factor $\xi^2 + \eta^2$, leading to the following equations of motion:

$$\frac{d\xi}{d\tau_1} = \bar{\delta}_\xi \sqrt{\epsilon\xi^4 + 2H\xi^2 + (2\mu + \kappa) - \frac{p_\phi^2}{\xi^2}} \tag{5.37}$$

$$\frac{d\eta}{d\tau_1} = \bar{\delta}_\eta \sqrt{-\epsilon\eta^4 + 2H\eta^2 + (2\mu - \kappa) - \frac{p_\phi^2}{\eta^2}} \tag{5.38}$$

Rearranging these differential equations into a form suitable for quadrature gives:

$$d\tau_1 = \bar{\delta}_\xi \frac{\xi d\xi}{\sqrt{\epsilon\xi^6 + 2H\xi^4 + (2\mu + \kappa)\,\xi^2 - p_\phi^2}} \tag{5.39}$$

$$d\tau_1 = \bar{\delta}_\eta \frac{\eta d\eta}{\sqrt{-\epsilon\eta^6 + 2H\eta^4 + (2\mu - \kappa)\,\eta^2 - p_\phi^2}} \tag{5.40}$$

The integration of Eqs. (5.39) and (5.40) is not trivial, as the resulting expressions involve sixth-order polynomials under the square root. These integrals require intermediate transformations to reduce them into standard forms suitable for resolution through elliptic functions. Since Eqs. (5.39) and (5.40) share the same mathematical structure, it is convenient to instead consider a generic form of the equation:

$$d\tau_1 = \bar{\delta} \frac{X dX}{\sqrt{P_1(X)}} \quad \textit{where} \quad P_1(X) = a_1 X^6 + a_2 X^4 + a_3 X^2 + a_4 \tag{5.41}$$

In Eq. (5.41), $X$ represents the generic variable (either $\xi$ or $\eta$), $P_1$ denotes the sixth-degree polynomial, and $a_1$, $a_2$, $a_3$, and $a_4$ are its non-zero coefficients. Since $P_1$ is an even polynomial, its order can be reduced by introducing the transformation:

$$X^2 = Y \quad \Rightarrow \quad 2X dX = dY \tag{5.42}$$

Substituting Eq. (5.42) into Eq. (5.41) yields the following:

$$d\tau_1 = \bar{\delta} \frac{dY}{2\sqrt{P_1(Y)}} \quad \textit{where} \quad P_1(Y) = a_1 Y^3 + a_2 Y^2 + a_3 Y + a_4 \tag{5.43}$$

Since $P_1(Y)$ is a cubic polynomial, it is ensured that at least one of its roots, $Y^*$, is real. Therefore, $P_1$ can be factorised as:

$$P_1(Y) = a_1 (Y - Y^*) P_2(Y) \tag{5.44}$$

Here, $P_2(Y)$ is a quadratic polynomial whose roots can be real or complex. To simplify Eq. (5.43), an additional transformation is introduced:

$$Y - Y^* = sign(a_1) Z^2 \quad \Rightarrow \quad dY = sign(a_1) 2Z dZ \tag{5.45}$$

Transformation in Eq. (5.45) allows to rewrite the polynomial in Eq. (5.44) as a function of $Z$.

$$P_1(Z) = |a_1| Z^2 P_2(Z) \tag{5.46}$$

Furthermore, applying the transformation in Eq. (5.45) to Eq. (5.43) leads to:

$$d\tau_1 = \bar{\delta} \frac{sign(a_1)\, dZ}{\sqrt{|a_1|\, P_2(Z)}} \tag{5.47}$$

The integration of Eq. (5.47) requires the explicit determination of the polynomial $P_2(Z)$, which in turn depends on the factorisation of $P_1(Y)$ and the location of its real root $Y^*$. Integration of Eq. (5.47) gives a solution for $Z$. Applying the inverse of the transformations introduced in Eqs. (5.45) and (5.42), gives the solution for $X$ as:

$$X = \sqrt{Y^* + sign(a_1) Z^2} \tag{5.48}$$

Depending on the coefficients $a_1$, $a_2$, $a_3$, and $a_4$, different cases emerge for the solutions of the cubic equation $P_1(Y) = 0$. These cases are classified according to the discriminant $D$, defined in Eq. (C.8), of the cubic equation. Appendix C provides the detailed derivation of the cubic root structure, from which the generic solution can be written as:

$$\begin{aligned} Y_1 &= -\frac{a_2}{3a_1} + (Y_1'' + Y_2'') \\ Y_2 &= -\frac{a_2}{3a_1} - \frac{1}{2}(Y_1'' + Y_2'') + i\frac{\sqrt{3}}{2}(Y_1'' - Y_2'') \\ Y_3 &= -\frac{a_2}{3a_1} - \frac{1}{2}(Y_1'' + Y_2'') - i\frac{\sqrt{3}}{2}(Y_1'' - Y_2'') \end{aligned} \tag{5.49}$$

Here, $Y_1''$ and $Y_2''$ are intermediate parameters defined in Eqs. (C.9) and (C.10), and depend on the coefficients of $P_1(Y)$.

Solutions for $D < 0$

The case $D < 0$ corresponds to three real and distinct roots. Since $Y_1''$ and $Y_2''$ are complex parameters, it is convenient to express them in exponential form. Taking the square root of $D$ as $\sqrt{D} = i\sqrt{-D}$, the parameters $Y_1''$ and $Y_2''$ can be written as:

$$\begin{aligned} Y_1'' &= \sqrt[3]{\bar{r}e^{i\bar{\theta}}} = \bar{r}^{\frac{1}{3}} e^{i\frac{\bar{\theta}}{3}} \\ Y_2'' &= \sqrt[3]{\bar{r}e^{-i\bar{\theta}}} = \bar{r}^{\frac{1}{3}} e^{-i\frac{\bar{\theta}}{3}} \end{aligned} \quad \textit{where} \quad \begin{aligned} \bar{r} &= \sqrt{-Q^3} \\ \bar{\theta} &= \arctan\left(\frac{\sqrt{-D}}{R}\right) \end{aligned} \tag{5.50}$$

Here, $\bar{r}$ and $\bar{\theta}$ represent the modulus and argument of the complex variable, respectively. The intermediate parameters $R$ and $P_2$ are defined in Eq. (C.7). Since $\bar{r}^{\frac{1}{3}} = \sqrt{-Q}$, it follows that $Y_1'' + Y_2''$ and $Y_1'' - Y_2''$ can be expressed as:

$$\begin{aligned} Y_1'' + Y_2'' &= 2\sqrt{-Q}\cos\left(\frac{\bar{\theta}}{3}\right) \\ Y_1'' - Y_2'' &= i2\sqrt{-Q}\sin\left(\frac{\bar{\theta}}{3}\right) \end{aligned} \tag{5.51}$$

Substituting these expressions into the roots given in Eq. (5.49), one obtains the three real roots corresponding to case $D < 0$:

$$\begin{aligned} Y_1 &= -\frac{a_2}{3a_1} + 2\sqrt{-Q}\cos\left(\frac{\bar{\theta}}{3}\right) \\ Y_2 &= -\frac{a_2}{3a_1} - \sqrt{-Q}\cos\left(\frac{\bar{\theta}}{3}\right) - \sqrt{3}\sqrt{-Q}\sin\left(\frac{\bar{\theta}}{3}\right) \\ Y_3 &= -\frac{a_2}{3a_1} - \sqrt{-Q}\cos\left(\frac{\bar{\theta}}{3}\right) + \sqrt{3}\sqrt{-Q}\sin\left(\frac{\bar{\theta}}{3}\right) \end{aligned} \tag{5.52}$$

To select the appropriate root $Y^*$, the three roots in Eq. (5.52) must be ordered. This requires bounding the value of $\bar{\theta}$.

$$\sqrt{-D} > 0 \quad \Rightarrow \quad \sin\bar{\theta} > 0 \quad \Rightarrow \quad \bar{\theta} \in (0, \pi] \tag{5.53}$$

Given that $\sqrt{-Q} > 0$, one can establish the relationships among the roots as:

$$\begin{aligned} Y_1 - Y_2 &= 3\sqrt{-Q}\cos\left(\frac{\bar{\theta}}{3}\right) + \sqrt{3}\sqrt{-Q}\sin\left(\frac{\theta}{3}\right) > 0 \\ Y_1 - Y_3 &= 3\sqrt{-Q}\cos\left(\frac{\bar{\theta}}{3}\right) - \sqrt{3}\sqrt{-Q}\sin\left(\frac{\bar{\theta}}{3}\right) > 0 \\ Y_2 - Y_3 &= -\sqrt{3}\sqrt{-Q}\sin\left(\frac{\bar{\theta}}{3}\right) < 0 \end{aligned} \tag{5.54}$$

From these relations, the absolute order of the roots follows as:

$$Y_1 > Y_3 > Y_2 \tag{5.55}$$

Equation (5.43) requires that $P_1(Y) > 0$. Depending on the sign of $a_1$, different valid solution intervals arise:

$$\begin{array}{lllllll} \xi: & a_1 > 0 & \Rightarrow & P_1(Y) > 0 & \Leftrightarrow & Y > Y_1 > Y_3 > Y_2 & || \quad Y_1 > Y_3 > Y > Y_2 \\ \eta: & a_1 < 0 & \Rightarrow & P_1(Y) > 0 & \Leftrightarrow & Y_1 > Y_3 > Y_2 > Y & || \quad Y_1 > Y > Y_3 > Y_2 \end{array} \tag{5.56}$$

Although two different intervals satisfy $P_1(Y) > 0$, for the case of $\eta$ with $a_1 < 0$, Eq. (5.48) imposes the restriction that $Z^2$ must remain bounded. Therefore, the interval $Y_1 > Y_3 > Y_2 > Y$ is not feasible.

Since $Z$ must be a real quantity, the condition $Z^2 > 0$ must be satisfied. The transformation in Eq. (5.45) then defines the value of $Y^*$ according to the sign of $a$:

$$\begin{array}{lllllll} \xi: & a_1 > 0 & \Rightarrow & Z^2 = +(Y - Y^*) & \Rightarrow & Y^* = Y_2 \\ \eta: & a_1 < 0 & \Rightarrow & Z^2 = -(Y - Y^*) & \Rightarrow & Y^* = Y_1 \end{array} \tag{5.57}$$

With the roots defined in Eq. (5.52), the feasible solution intervals from Eq. (5.56), and the selection of $Y^*$ in Eq. (5.57), the equation of motion in Eq. (5.47) can now be integrated. The goal is to manipulate the integral into the form of the elliptic integral of the first kind $F$, defined in [80] as:

$$F[u, K] = \int_0^u \frac{d\bar{\omega}}{\sqrt{(1-\bar{\omega}^2)(1-K^2\bar{\omega}^2)}} \quad \textit{where} \quad -1 \leq u \leq 1 \quad \& \quad 0 \leq K \leq 1 \tag{5.58}$$

Here, $u$ and $K$ denote the argument and modulus of the elliptic function. The elliptic integral of the first kind can also be expressed in terms of the inverse of the Jacobi elliptic sine function, $\mathrm{sn}$, as shown in [75].

$$F[u, K] = \mathrm{arcsn}[u, K] \tag{5.59}$$

Here, $\mathrm{arcsn}$ represents the inverse of the Jacobian elliptic sine.

The conditions on $u$ and $K$ in Eq. (5.58) determine the transformations needed to rewrite the integral in Eq. (5.47) in the required form.

For the variable $\xi$, the roots of the polynomial $P_2(Z)$ are given by:

$$\begin{aligned} Z_{1,\xi}^2 &= (Y_1 - Y_2) > 0 \\ Z_{3,\xi}^2 &= (Y_3 - Y_2) > 0 \end{aligned} \tag{5.60}$$

In Eq. (5.60), $Z_{i,\xi}$ denotes the root of $P_2(Z)$ associated with the $i$-th root of $P_1(Y)$. Substituting into Eq. (5.47), the equation of motion becomes:

$$d\tau_1 = \bar{\delta}_\xi \frac{dZ}{\sqrt{a_1}\sqrt{\left(Z^2 - Z_{1,\xi}^2\right)\left(Z^2 - Z_{3,\xi}^2\right)}} \tag{5.61}$$

For the interval $Y_1 > Y_3 > Y > Y_2$, the order of the roots of $P_2(Z)$ is as:

$$Z_{1,\xi}^2 > Z_{3,\xi}^2 > Z_{\xi,I}^2 \tag{5.62}$$

Here, $Z_{\xi,I}$ denotes the solution for case $I$ of the variable $\xi$. To match the form of Eq. (5.58), the following transformation is applied:

$$\bar{\omega} = \frac{Z_{\xi,I}}{Z_{3,\xi}} \quad \Rightarrow \quad d\bar{\omega} = \frac{1}{Z_{3,\xi}} dZ \tag{5.63}$$

From Eq. (5.62), it follows that $|\bar{\omega}| < 1$, fulfilling the condition from Eq. (5.58). After algebraic manipulation, Eq. (5.61) becomes:

$$d\tau_1 = \bar{\delta}_{\xi,I} \frac{d\bar{\omega}}{\sqrt{a_1} Z_{1,\xi} \sqrt{(1-\bar{\omega}^2)\left(1 - K_{\xi,I}^2 \bar{\omega}^2\right)}} \quad \textit{where} \quad K_{\xi,I} = \frac{Z_{3,\xi}}{Z_{1,\xi}} < 1 \tag{5.64}$$

Using Eqs. (5.58), (5.59), and (5.63), the integral can be solved to yield the solution for $Z_{\xi,I}$.

$$Z_{\xi,I} = Z_{3,\xi}\mathrm{sn}\left[u_{\xi,I}, K_{\xi,I}\right] \quad \textit{where} \quad u_{\xi,I} = \sqrt{a_1}Z_{1,\xi}\left(\bar{\delta}_{\xi,I}\tau_1 - \tau_{1,\xi,0,I}\right) \tag{5.65}$$

Equation (5.65) describes the evolution of $Z$ with respect to the fictitious time $\tau_1$ for case $I$. The initial condition $\tau_{1,\xi,0,I}$ is determined from Eq. (5.64) as:

$$\tau_{1,\xi,0,I} = -\frac{1}{\sqrt{a_1}Z_{1,\xi}}F\left[\frac{Z_{\xi,I,0}}{Z_{3,\xi}}, K_{\xi,I}\right] \tag{5.66}$$

Here, $Z_{\xi,0,I}$ is the initial value of $Z_{\xi,I}$, which is related to $\xi_0$ through Eq. (5.48). In Eq. (5.65), the sign $\bar{\delta}_{\xi,I}$ remains undetermined. To define it, the initial velocity is used. Differentiating Eq. (5.48) with respect to $\tau_1$ gives the following:

$$\xi\frac{d\xi}{d\tau_1} = Z\frac{dZ}{d\tau_1} \tag{5.67}$$

In Eq. (5.67), the derivative of $Z$ with respect to $\tau_1$ can be obtained using the derivatives for the Jacobi elliptic functions given in [75], yielding the following:

$$\frac{dZ_{\xi,I}}{d\tau_1} = Z_{3,\xi}\sqrt{a_1}Z_{1,\xi}\bar{\delta}_{\xi,I}\mathrm{cn}\left[u_{\xi,I}, K_{\xi,I}\right]\mathrm{dn}\left[u_{\xi,I}, K_{\xi,I}\right] \tag{5.68}$$

Here, $\mathrm{cn}$ and $\mathrm{dn}$ denote Jacobi elliptic cosine and delta functions, respectively. Given that $\xi, \eta > 0$, Eq. (5.5) results in $sign(\frac{d\xi}{d\tau_1}) = sign(\dot{\xi})$. Therefore, substituting Eqs. (5.65) and (5.68) into Eq. (5.67) and evaluating the expression at $\tau_1 = 0$ yields the relation between the sign of $\bar{\delta}_{\xi,I}$ and the initial velocity $\dot{\xi}_{0,I}$.

$$\bar{\delta}_{\xi,I} = sign\left(\frac{\xi_{0,I}\dot{\xi}_{0,I}}{Z_{3,\xi}^3\sqrt{a_1}Z_{1,\xi}\mathrm{sn}\left[u_{\xi,0,I}, K_{\xi,I}\right]\mathrm{cn}\left[u_{\xi,0,I}, K_{\xi,I}\right]\mathrm{dn}\left[u_{\xi,0,I}, K_{\xi,I}\right]}\right) \tag{5.69}$$

Here, $u_{\xi,0,I}$ corresponds to the value of the argument $u_{\xi,I}$ when $\tau_1 = 0$, given by:

$$u_{\xi,0,I} = -\sqrt{a_1}Z_{1,\xi}\tau_{1,\xi,0,I} \tag{5.70}$$

Since only the sign of each factor in Eq. (5.69) is relevant, positive constants can be omitted, yielding a simplified expression.

$$\bar{\delta}_{\xi,I} = sign\left(\dot{\xi}_{0,I}\mathrm{sn}\left[u_{\xi,0,I}, K_{\xi,I}\right]\mathrm{cn}\left[u_{\xi,0,I}, K_{\xi,I}\right]\right) \tag{5.71}$$

For the interval $Y > Y_1 > Y_3 > Y_2$, the same approach is employed to integrate the equation of motion. For this case, the order of the roots of $P_2\left(Z\right)$ is as:

$$Z_{\xi,III}^2 > Z_{1,\xi}^2 > Z_{3,\xi}^2 \tag{5.72}$$

Note that in Eq. (5.72), the case has been identified as $III$, skipping case $II$. Case $II$ is reserved for a later configuration, and the numbering has been chosen deliberately to preserve analogy with the Kepler problem solutions. To match the form of Eq. (5.58), the following transformation is applied:

$$\bar{\omega} = \frac{Z_{1,\xi}}{Z_{\xi,III}} \quad \Rightarrow \quad d\bar{\omega} = -\frac{Z_{1,\xi}}{Z_{\xi,III}^2}dZ \tag{5.73}$$

From Eq. (5.72), it follows that $|\bar{\omega}| < 1$, fulfilling the condition from Eq. (5.58). After algebraic manipulation, the equation of motion becomes:

$$d\tau_1 = -\bar{\delta}_{\xi,III}\frac{d\bar{\omega}}{\sqrt{a_1}Z_{1,\xi}\sqrt{\left(1-\bar{\omega}^2\right)\left(1-K_{\xi,III}^2\bar{\omega}^2\right)}} \quad \textit{where} \quad K_{\xi,III} = \frac{Z_{3,\xi}}{Z_{1,\xi}} < 1 \tag{5.74}$$

Using Eqs. (5.58), (5.59), and (5.73), the integral can be solved to yield the solution for $Z_{\xi,III}$:

$$Z_{\xi,III} = \frac{Z_{1,\xi}}{\mathrm{sn}\left[u_{\xi,III}, K_{\xi,III}\right]} \quad \textit{where} \quad u_{\xi,III} = -\sqrt{a_1}Z_{1,\xi}\left(\bar{\delta}_{\xi,III}\tau_1 - \tau_{1,\xi,0,III}\right) \tag{5.75}$$

The initial condition $\tau_{1,\xi,0,III}$ is obtained from Eq. (5.74) as:

$$\tau_{1,\xi,0,III} = \frac{1}{\sqrt{a_1} Z_{1,\xi}} F\left[\frac{Z_{1,\xi}}{Z_{\xi,III,0}}, K_{\xi,III}\right] \tag{5.76}$$

Following the same procedure as before, the relation between $\bar{\delta}_{\xi,III}$ and $\dot{\xi}_{0,III}$ is given by:

$$\bar{\delta}_{\xi,III} = sign\left(\dot{\xi}_{0,III} \mathrm{sn}\left[u_{\xi,0,III}, K_{\xi,III}\right] \mathrm{cn}\left[u_{\xi,0,III}, K_{\xi,III}\right]\right) \tag{5.77}$$

Here, $u_{\xi,0,III}$ corresponds to the value of the argument $u_{\xi,III}$ when $\tau_1 = 0$, given by:

$$u_{\xi,0,III} = \sqrt{a_1} Z_{1,\xi} \tau_{1,\xi,0,III} \tag{5.78}$$

Equations (5.65) and (5.75) give the solutions for the variable $\xi$ when $D < 0$ for cases $I$ and $III$, which depend on the initial conditions of $\xi$, $\xi_0$.

In the case of the variable $\eta$, to integrate the equation of motion, the same procedure as for $\xi$ is followed. For the variable $\eta$, the roots of the polynomial $P_2(Z)$ are given by:

$$\begin{aligned} Z_{2,\eta}^2 &= -(Y_2 - Y_1) > 0 \\ Z_{3,\eta}^2 &= -(Y_3 - Y_1) > 0 \end{aligned} \tag{5.79}$$

Substituting these roots into Eq. (5.47), the equation of motion becomes:

$$d\tau_1 = -\bar{\delta}_\eta \frac{dZ}{\sqrt{-a_1}\sqrt{\left(Z^2 - Z_{2,\eta}^2\right)\left(Z^2 - Z_{3,\eta}^2\right)}} \tag{5.80}$$

As stated before, only the interval $Y_1 > Y > Y_3 > Y_2$ is valid as a solution for $\eta$. For this case, the order of the roots of $P_2(Z)$ is:

$$Z_{2,\eta}^2 > Z_{3,\eta}^2 > Z_{\eta,I}^2 \tag{5.81}$$

Here, $Z_{\eta,I}$ denotes the solution for case $I$ of the variable $\eta$. To match the form of Eq. (5.58), the following transformation is applied:

$$\bar{\omega} = \frac{Z_{\eta,I}}{Z_{3,\eta}} \quad \Rightarrow \quad d\bar{\omega} = \frac{1}{Z_{3,\eta}} dZ \tag{5.82}$$

From Eq. (5.81), it follows that $|\bar{\omega}| < 1$, fulfilling the condition from Eq. (5.58). After algebraic manipulation, the equation of motion becomes:

$$d\tau_1 = -\bar{\delta}_\eta \frac{d\bar{\omega}}{\sqrt{-a_1} Z_{2,\eta} \sqrt{\left(1 - \bar{\omega}^2\right)\left(1 - K_{\eta,I}^2 \bar{\omega}^2\right)}} \quad \textit{where} \quad K_{\eta,I} = \frac{Z_{3,\eta}}{Z_{2,\eta}} < 1 \tag{5.83}$$

Using Eqs. (5.58), (5.59), and (5.82), the integral can be solved to yield the solution for $Z_{\eta,I}$:

$$Z_{\eta,I} = Z_{3,\eta} \mathrm{sn}\left[u_{\eta,I}, K_{\eta,I}\right] \quad \textit{where} \quad u_{\eta,I} = -\sqrt{-a_1} Z_{2,\eta}\left(\bar{\delta}_{\eta,I} \tau_1 - \tau_{1,\eta,0,I}\right) \tag{5.84}$$

The initial condition $\tau_{1,\eta,0,I}$ is obtained from Eq. (5.83) as:

$$\tau_{1,\eta,0,I} = \frac{1}{\sqrt{-a_1} Z_{2,\eta}} F\left[\frac{Z_{\eta,0,I}}{Z_{3,\eta}}, K_{\eta,I}\right] \tag{5.85}$$

Following the same procedure as before, the relation between $\bar{\delta}_{\eta,I}$ and $\dot{\eta}_{0,I}$ is given by:

$$\bar{\delta}_{\eta,I} = sign\left(\dot{\eta}_{0,I} \mathrm{sn}\left[u_{\eta,0,I}, K_{\eta,I}\right] \mathrm{cn}\left[u_{\eta,0,I}, K_{\eta,I}\right]\right) \quad \textit{where} \quad u_{\eta,0,I} = \sqrt{-a_1} Z_{1,\eta} \tau_{1,\eta,0,I} \tag{5.86}$$

Here, $u_{\eta,0,I}$ corresponds to the value of the argument $u_{\eta,I}$ when $\tau_1 = 0$, given by:

$$u_{\eta,0,I} = \sqrt{-a_1} Z_{1,\eta} \tau_{1,\eta,0,I} \tag{5.87}$$

Solutions for $D = 0$

The case $D = 0$ corresponds to the degenerate configuration in which the cubic equation possesses three real roots, with two of them being equal. From Eqs. (C.9) and (C.10), the parameters $Y_1''$ and $Y_1''$ reduce to:

$$Y_1'' = Y_2'' = \sqrt[3]{R} \tag{5.88}$$

Substituting Eq. (5.88) into Eq. (5.49) yields the three real roots associated with the case $D = 0$:

$$\begin{aligned} Y_1 &= -\frac{a_2}{3a_1} + 2\sqrt[3]{R} \\ Y_2 &= -\frac{a_2}{3a_1} - \sqrt[3]{R} \\ Y_3 &= -\frac{a_2}{3a_1} - \sqrt[3]{R} \end{aligned} \tag{5.89}$$

As in the case $D < 0$, the relative ordering of the roots can be established from:

$$Y_1 - Y_2 = Y_1 - Y_3 = 3\sqrt[3]{R} \quad \begin{cases} > 0 & \textit{If} \quad R > 0 \\ < 0 & \textit{If} \quad R < 0 \end{cases} \tag{5.90}$$

Although the ordering is informative, it is not essential for the subsequent integration, since the presence of a double root considerably simplifies the structure of the integral. Nonetheless, the admissible intervals for $P_1(Y) > 0$ still depend on the sign of $a_1$:

$$\begin{aligned} \xi: \quad a_1 > 0 \quad &\Rightarrow \quad P_1(Y) > 0 \quad \Leftrightarrow \quad Y > Y_i \quad \forall i \in [1,3] \\ \eta: \quad a_1 < 0 \quad &\Rightarrow \quad P_1(Y) > 0 \quad \Leftrightarrow \quad Y_i > Y \quad \forall i \in [1,3] \end{aligned} \tag{5.91}$$

Analogous to the case $D < 0$, the solution for $\eta$ requires $Z^2$ to be bounded. The admissible interval in Eq. (5.91) for $a_1 < 0$ does not satisfy this boundedness condition, which implies that no physically valid solution for $\eta$ exists when $D = 0$. Consequently, the case $D = 0$ is only relevant for the variable $\xi$.

For $\xi$, the simplification is achieved by setting $Y^* = Y_1$ in the transformation in Eq. (5.45), which leads to the roots of $P_2(Z)$:

$$Z_{2,\xi}^2 = Z_{3,\xi}^2 = (Y_2 - Y_1) = (Y_3 - Y_1) \tag{5.92}$$

The polynomial $P_2(Z)$ then reduces to:

$$P_2(Z) = \left(Z^2 - Z_{2,\xi}^2\right)^2 = \left(Z^2 - Z_{2,\xi}^2\right)^2 \tag{5.93}$$

Since $Z^2 > Z_i \quad \forall i \in 1,2,3$, the equation of motion in Eq. (5.47) becomes:

$$d\tau_1 = \bar{\delta}_\xi \frac{dZ}{\sqrt{a_1}\left(Z^2 - Z_2^2\right)} \tag{5.94}$$

Introducing the variable substitution:

$$\bar{\omega} = \frac{Z_{\xi,II}}{Z_{2,\xi}} \quad \Rightarrow \quad d\bar{\omega} = \frac{1}{Z_{2,\xi}} dZ \tag{5.95}$$

Here, $Z_{\xi,II}$ denotes the solution for the case $II$ of $\xi$. Eq. (5.94) transforms into:

$$d\tau_1 = \bar{\delta}_{\xi,II} \frac{d\bar{\omega}}{\sqrt{a_1} Z_{2,\xi}\left(\bar{\omega}^2 - 1\right)} \tag{5.96}$$

This integral is straightforward, yielding the solution for $Z_{\xi,II}$:

$$Z_{\xi,II} = Z_{2,\xi} \tanh\left[u_{\xi,II}\right] \quad \textit{where} \quad u_{\xi,II} = -\sqrt{a_1} Z_{2,\xi}\left(\bar{\delta}_{\xi,II}\tau_1 - \tau_{1,\xi,0,II}\right) \tag{5.97}$$

Here, $\tanh$ denotes the hyperbolic tangent, which arises as the limiting case of the Jacobi elliptic sine $\mathrm{sn}$ when $K = 1$. The initial condition $\tau_{1,\xi,0,II}$ is determined from (5.96) as:

$$\tau_{1,\xi,0,II} = -\frac{1}{\sqrt{a_1} Z_{2,\xi}} \operatorname{arctanh}\left(\frac{Z_{\xi,0,II}^2}{Z_{2,\xi}^2} - 1\right) \tag{5.98}$$

Moreover, the relation between the sign $\bar{\delta}_{\xi,II}$ and the initial velocity $\dot{\xi}_{0,II}$ follows as:

$$\bar{\delta}_{\xi,II} = sign\left(\dot{\xi}_{0,II} Z_{2,\xi} \tanh\left[u_{\xi,0,II}\right]\right) \tag{5.99}$$

Here, $u_{\xi,0,II}$ corresponds with the value of $u_{\xi,II}$ at $\tau_1 = 0$:

$$u_{\xi,0,II} = \sqrt{a_1} Z_{2,\xi} \tau_{1,\xi,0,II} \tag{5.100}$$

Equation (5.97) thus provides the closed-form solution for $Z_\xi$ in the degenerate case $D = 0$. It must be emphasized, however, that this case is of theoretical interest only. In practice, achieving the precise boundary condition between $D < 0$ and $D > 0$ is infeasible, and even more so from a numerical standpoint.

Solutions for $D > 0$

The case $D > 0$ corresponds to a scenario in which the cubic polynomial $P_1(Y)$ admits a single real root and a pair of complex conjugate roots. The real root, denoted by $Y^*$, corresponds to $Y_1$ in Eq. (5.49), where $Y_1''$ and $Y_2''$ are defined in Eqs. (C.9) and (C.10), respectively.

Given that $P_2(Y) = (Y - Y_2)(Y - Y_3)$ and the roots $Y_2, Y_3$ are complex conjugates, it follows that $P_2(Y)$ never intersects the real axis. Therefore, $P_2(Y) > 0 \; \forall Y \in \mathbb{R}$. To ensure $P_1(Y) > 0$, the condition $a_1(Y - Y_1) > 0$ must hold. This requirement leads to the following admissible intervals of solution:

$$\begin{aligned} \xi: \quad a_1 > 0 \quad &\Rightarrow \quad P_1(Y) > 0 \quad \Leftrightarrow \quad Y > Y_1 \\ \eta: \quad a_1 < 0 \quad &\Rightarrow \quad P_1(Y) > 0 \quad \Leftrightarrow \quad Y_1 > Y \end{aligned} \tag{5.101}$$

Since the solution for $\eta$ requires boundedness of $Z^2$, this case is not physically admissible when $D > 0$. Consequently, only the $\xi$ branch is relevant.

Applying the transformation in Eq. (5.48), the corresponding roots of $P_2(Z)$ are obtained as:

$$\begin{aligned} Z_{2,IV}^2 = (Y_2 - Y_1) &= \left(-\frac{3}{2}(Y_1'' + Y_2'') + i\frac{\sqrt{3}}{2}(Y_1'' - Y_2'')\right) \\ Z_{3,IV}^2 = (Y_3 - Y_1) &= \left(-\frac{3}{2}(Y_1'' + Y_2'') - i\frac{\sqrt{3}}{2}(Y_1'' - Y_2'')\right) \end{aligned} \tag{5.102}$$

These roots are complex conjugates. The goal is to reformulate $P_2(Z)$ such that the integral of motion in Eq. (5.47) reduces to the elliptic integral of the first kind in Eq. (5.58). The polynomial $P_2(Z)$ can be expressed as:

$$P_2(Z) = \left(Z^2 - Z_{2,IV}^2\right)\left(Z^2 - Z_{3,IV}^2\right) = (Z - Z_{2,IV})(Z + Z_{2,IV})(Z - Z_{3,IV})(Z + Z_{3,IV}) \tag{5.103}$$

Algebraic manipulation of Eq. (5.103) leads to:

$$P_2(Z) = \left[Z^2 - (Z_{2,IV} + Z_{3,IV})Z + Z_{2,IV}Z_{3,IV}\right]\left[Z^2 + (Z_{2,IV} + Z_{3,IV})Z + Z_{2,IV}Z_{3,IV}\right] \tag{5.104}$$

From [81], the square root of a complex number is given by:

$$\sqrt{\bar{a} + i\bar{b}} = \sqrt{\frac{\bar{a} + \sqrt{\bar{a}^2 + \bar{b}^2}}{2}} + isign\left(\bar{b}\right)\sqrt{\frac{-\bar{a} + \sqrt{\bar{a}^2 + \bar{b}^2}}{2}} \tag{5.105}$$

Taking into account the relation in Eq. (5.105), it follows after manipulation that:

$$\begin{aligned} Z_{2,IV} + Z_{3,IV} &= 2\bar{A} \\ Z_{2,IV}Z_{3,IV} &= \bar{A}^2 + \bar{B}^2 \end{aligned} \tag{5.106}$$

Here, $\bar{A}$ and $\bar{B}$ are real quantities defined by:

$$\bar{A} = \frac{1}{\sqrt{2}}\sqrt{-\frac{3}{2}(Y_1'' + Y_2'') + \sqrt{\frac{9}{4}(Y_1'' + Y_2'')^2 + \frac{3}{4}(Y_1'' - Y_2'')^2}} \tag{5.107}$$

$$\bar{B} = \frac{1}{\sqrt{2}}\sqrt{+\frac{3}{2}(Y_1'' + Y_2'') + \sqrt{\frac{9}{4}(Y_1'' + Y_2'')^2 + \frac{3}{4}(Y_1'' - Y_2'')^2}} \tag{5.108}$$

Substitution of Eq. (5.106) into Eq. (5.103) yields:

$$P_2(Z) = \left[Z^2 - 2\bar{A}Z + \left(\bar{A}^2 + \bar{B}^2\right)\right]\left[Z^2 + 2\bar{A}Z + \left(\bar{A}^2 + \bar{B}^2\right)\right] = P_{2,1}(Z)\,P_{2,2}(Z) \tag{5.109}$$

In Eq. (5.109), $P_{2,1}(Z)$ and $P_{2,2}(Z)$ possess only real coefficients. To simplify these polynomials, Cayley's reduction method [82] is applied through the transformation:

$$Z = \frac{\lambda\varphi + \nu}{\varphi + 1} \quad \Rightarrow \quad dZ = \frac{\lambda - \nu}{(\varphi+1)^2}d\varphi \tag{5.110}$$

Here, $\varphi$ is the new variable and $\lambda, \nu$ are constants that will later be selected to eliminate first-order terms. By substituting the transformation given in Eq. (5.110) into Eq. (5.109), one obtains the following representations of the polynomials $P_{2,1}(Z)$ and $P_{2,2}(Z)$ in terms of $\varphi$ as:

$$\begin{aligned} P_{2,1}(\varphi) &= \frac{(\lambda\varphi+\nu)^2 - 2\bar{A}(\lambda\varphi+\nu)(\varphi+1) + \left(\bar{A}^2+\bar{B}^2\right)(\varphi+1)^2}{(\varphi+1)^2} \\ P_{2,2}(\varphi) &= \frac{(\lambda\varphi+\nu)^2 + 2\bar{A}(\lambda\varphi+\nu)(\varphi+1) + \left(\bar{A}^2+\bar{B}^2\right)(\varphi+1)^2}{(\varphi+1)^2} \end{aligned} \tag{5.111}$$

Expanding the numerators of Eq. (5.111) and collecting terms according to the powers of $\varphi$ leads to a more explicit quadratic representation for both polynomials:

$$\begin{aligned} P_{2,1}(\varphi) &= \frac{\left[\lambda^2 - 2\bar{A}\lambda + \left(\bar{A}^2+\bar{B}^2\right)\right]\varphi^2 + 2\left[\lambda\nu - \bar{A}(\lambda+\nu) + \left(\bar{A}^2+\bar{B}^2\right)\right]\varphi + \left[\nu^2 - 2\bar{A}\nu + \left(\bar{A}^2+\bar{B}^2\right)\right]}{(\varphi+1)^2} \\ P_{2,2}(\varphi) &= \frac{\left[\lambda^2 + 2\bar{A}\lambda + \left(\bar{A}^2+\bar{B}^2\right)\right]\varphi^2 + 2\left[\lambda\nu + \bar{A}(\lambda+\nu) + \left(\bar{A}^2+\bar{B}^2\right)\right]\varphi + \left[\nu^2 + 2\bar{A}\nu + \left(\bar{A}^2+\bar{B}^2\right)\right]}{(\varphi+1)^2} \end{aligned} \tag{5.112}$$

The idea is to choose $\lambda$ and $\nu$ such that the coefficients corresponding to the first order of $\varphi$ become null. Therefore, the values for $\lambda$ and $\nu$ can be found as:

$$\begin{aligned} \lambda\nu - \bar{A}(\lambda+\nu) + \left(\bar{A}^2+\bar{B}^2\right) &= 0 \\ \lambda\nu + \bar{A}(\lambda+\nu) + \left(\bar{A}^2+\bar{B}^2\right) &= 0 \end{aligned} \quad \Rightarrow \quad \begin{cases} \lambda = +\sqrt{\bar{A}^2+\bar{B}^2} \\ \nu = -\sqrt{\bar{A}^2+\bar{B}^2} \end{cases} \tag{5.113}$$

By fixing $\nu = -\lambda$, Eq. (5.112) simplifies to the compact quadratic form:

$$\begin{aligned} P_{2,1}(\varphi) &= \frac{2\lambda\left(\lambda - \bar{A}\right)\varphi^2 + 2\lambda\left(\lambda + \bar{A}\right)}{(\varphi+1)^2} \\ P_{2,2}(\varphi) &= \frac{2\lambda\left(\lambda + \bar{A}\right)\varphi^2 + 2\lambda\left(\lambda - \bar{A}\right)}{(\varphi+1)^2} \end{aligned} \tag{5.114}$$

Further rearrangement of these polynomials yields:

$$\begin{aligned} P_{2,1}(\varphi) &= \frac{\bar{J}^2}{(\varphi+1)^2}\left(\varphi^2 + \bar{N}^2\right) \\ P_{2,2}(\varphi) &= \frac{\bar{M}^2}{(\varphi+1)^2}\left(\varphi^2 + \frac{1}{\bar{N}^2}\right) \end{aligned} \tag{5.115}$$

Here, $\bar{J}$, $\bar{M}$ and $\bar{N}$ are given by:

$$\begin{aligned} \bar{J}^2 &= 2\lambda\left(\lambda - \bar{A}\right) \\ \bar{M}^2 &= 2\lambda\left(\lambda + \bar{A}\right) \\ \bar{N}^2 &= \frac{\bar{M}^2}{\bar{J}^2} \end{aligned} \tag{5.116}$$

By applying the transformation defined in Eq. (5.110) to the generic equation of motion in Eq. (5.47), and substituting the polynomial expressions from Eq. (5.115), the differential form of the equation of motion can be expressed as:

$$d\tau_1 = \bar{\delta}_{\xi,IV}\frac{2\lambda d\varphi}{\sqrt{a_1}\bar{J}\bar{M}\sqrt{\varphi^2+\bar{N}^2}\sqrt{\varphi^2+\frac{1}{\bar{N}^2}}} \tag{5.117}$$

In order to reduce Eq. (5.117) to the canonical form of an elliptic integral of the first kind in Eq. (5.58), the following change of variable is introduced.

$$\varphi = \frac{1}{\bar{N}} \frac{\zeta}{\sqrt{1-\zeta^2}} \quad \Rightarrow \quad d\varphi = \frac{1}{\bar{N}} \frac{1}{(1-\zeta^2)^{\frac{3}{2}}} d\zeta \tag{5.118}$$

With this substitution, Eq. (5.117) becomes:

$$d\tau_1 = \bar{\delta}_{\xi,IV} \frac{2\lambda d\zeta}{\sqrt{a_1}\bar{M}^2\sqrt{1-\zeta^2}\sqrt{1-K_{\xi,IV}^2\zeta^2}} \quad \Rightarrow \quad \textit{where} \quad K_{\xi,IV}^2 = \left(1 - \frac{1}{\bar{N}^4}\right) \tag{5.119}$$

Integration of Eq. (5.119) yields the solution for $\zeta$ as:

$$\zeta = \mathrm{sn}\left[u_{\xi,IV}, K_{\xi,IV}\right] \quad \textit{where} \quad u_{\xi,IV} = \sqrt{a_1}\frac{\bar{M}^2}{2\lambda}\left(\bar{\delta}_{\xi,IV}\tau_1 - \tau_{1,\xi,0,IV}\right) \tag{5.120}$$

Applying the transformation introduced in Eq. (5.118) to the solution in Eq. (5.120) provides the explicit expression for $\varphi$ as:

$$\varphi = \frac{1}{\bar{N}} \frac{\mathrm{sn}\left[u_{\xi,IV}, K_{\xi,IV}\right]}{\mathrm{cn}\left[u_{\xi,IV}, K_{\xi,IV}\right]} \tag{5.121}$$

In this derivation, the fundamental identity $\mathrm{sn}^2\left[u,K\right] + \mathrm{cn}^2\left[u,K\right] = 1$ has been used simplifying the resulting expression. Finally, by substituting Eq. (5.121) into the Cayley transformation in Eq. (5.110), one obtains the closed-form expression for the solution $Z_{\xi,IV}$:

$$Z_{\xi,IV} = \lambda \frac{\mathrm{sn}\left[u_{\xi,IV}, K_{\xi,IV}\right] - \bar{N}\mathrm{cn}\left[u_{\xi,IV}, K_{\xi,IV}\right]}{\mathrm{sn}\left[u_{\xi,IV}, K_{\xi,IV}\right] + \bar{N}\mathrm{cn}\left[u_{\xi,IV}, K_{\xi,IV}\right]} \tag{5.122}$$

The initial condition $\tau_{1,\xi,0,IV}$ is determined from Eq. (5.119) as:

$$\tau_{1,\xi,0,IV} = \frac{2\lambda}{\sqrt{a_1}\bar{M}^2} F\left[\frac{\bar{N}\frac{\lambda+Z_{\xi,0,IV}}{\lambda-Z_{\xi,0,IV}}}{\sqrt{1+\bar{N}^2\left(\frac{\lambda+Z_{\xi,0,IV}}{\lambda-Z_{\xi,0,IV}}\right)^2}}, K_{\xi,IV}\right] \tag{5.123}$$

Here, the variable $\zeta$ has been transformed back to the original variable $Z$ using the successive transformations in Eqs. (5.118) and (5.110). To fully define solution in Eq. (5.122), the relation between the sign $\bar{\delta}_{\xi,IV}$ and the initial velocity $\dot{\xi}_{0,IV}$ is determined as:

$$\bar{\delta}_{\xi,IV} = sign\left(\dot{\xi}_{0,IV}\bar{N}\left(\mathrm{sn}^2\left[u_{\xi,0,IV}, K_{\xi,IV}\right] - \bar{N}^2\mathrm{cn}^2\left[u_{\xi,0,IV}, K_{\xi,IV}\right]\right)\right) \tag{5.124}$$

Here, $u_{\xi,0,IV}$ denotes the value of $u_{\xi,IV}$ at $\tau_1 = 0$:

$$u_{\xi,0,IV} = -\sqrt{a_1}\frac{\bar{M}^2}{2\lambda}\tau_{1,\xi,0,IV} \tag{5.125}$$

Therefore, Eq. (5.122) provides the closed-form solution for $Z_\xi$ in the case $D > 0$.

### 5.4.3. Integration of $\tau_2$

Subsection 5.4.1 provides the evolution of the variable $\phi$ with respect to the fictitious time $\tau_2$, while Subsection 5.4.2 describes the evolution of the variables $\xi$ and $\eta$ with respect to the fictitious time $\tau_1$. However, the problem cannot be fully integrated unless a relationship between $\tau_1$ and $\tau_2$ is established, due to the presence of two independent fictitious times. This subsection determines the relation linking $\tau_1$ and $\tau_2$.

From Eqs. (5.5) and (5.6), the differential connection between the fictitious times is expressed as:

$$d\tau_2 = \left(\frac{1}{\xi^2} + \frac{1}{\eta^2}\right) d\tau_1 \tag{5.126}$$

Since the terms on the right-hand side depend on distinct variables, $\xi$ and $\eta$, the integration of each term can be performed independently. Accordingly, the evolution of $\tau_2$ as a function of $\tau_1$ can be written as:

$$\tau_2 = \tau_{2,\xi}\left(\tau_1\right) + \tau_{2,\eta}\left(\tau_1\right) \tag{5.127}$$

Here, $\tau_{2,\xi}$ and $\tau_{2,\eta}$, functions of $\tau_1$, are given by:

$$\tau_{2,\xi} = \int_0^{\tau_1} \frac{1}{\xi^2} d\tau_1 \tag{5.128}$$

$$\tau_{2,\eta} = \int_0^{\tau_1} \frac{1}{\eta^2} d\tau_1 \tag{5.129}$$

The explicit forms of $\tau_{2,\xi}$ and $\tau_{2,\eta}$ depend on the case defined by the discriminant $D$ of the underlying cubic equation. Nevertheless, since the integrations are separable, the solutions for $\tau_{2,\xi}$ and $\tau_{2,\eta}$ can be obtained independently for each variable.

### Integration of $\tau_{2,\xi}$

For the variable $\xi$, the integration of $\tau_{2,\xi}$ depends on the specific solution of the associated cubic equation. Employing the solutions for $Z$ derived in Subsection 5.4.2 together with the transformation defined in Eq. (5.48), the evolution of $\xi$ can be explicitly determined for each of the four distinct cases corresponding to the different roots of the cubic equation.

For Case $I$, the solution for $Z$ given in Eq. (5.65) directly leads to the corresponding expression for $\xi$:

$$\xi_I = \sqrt{Y^*_{\xi,I} + Z^2_{3,\xi}\mathrm{sn}^2\left[u_{\xi,I}, K_{\xi,I}\right]} \tag{5.130}$$

Here, $Y^*_{\xi,I}$ corresponds to the $Y^*$ defined for the case $I$ for variable $\xi$. Substituting Eq. (5.130) into Eq. (5.128) gives the integral form of $\tau_{2,\xi,I}$:

$$\tau_{2,\xi,I} = \int_0^{\tau_1} \frac{d\tau_1}{Y^*_{\xi,I} + Z^2_{3,\xi}\mathrm{sn}^2\left[u_{\xi,I}, K_{\xi,I}\right]} \tag{5.131}$$

The objective is to manipulate the integral in Eq. (5.131) into the standard form of an elliptic integral of the third kind, $\Pi$, as defined in [83]:

$$\Pi\left[n, u, K\right] = \int_0^{u} \frac{d\bar{\omega}}{1 - n\mathrm{sn}^2\left[\bar{\omega}, K\right]} \quad \textit{where} \quad 0 \leq K \leq 1 \quad \& \quad n \neq 1 \tag{5.132}$$

Introducing the change of variable:

$$\bar{\omega} = u_{\xi,I} \quad \Rightarrow \quad d\bar{\omega} = \sqrt{a_1} Z_{1,\xi} \bar{\delta}_{\xi,I} d\tau_1 \tag{5.133}$$

Algebraic manipulation of Eq. (5.131) allows to rewrite the integral as:

$$\tau_{2,\xi,I} = \frac{1}{Y^*_{\xi,I}\sqrt{a_1} Z_{1,\xi}\bar{\delta}_{\xi,I}} \int_{u_{\xi,0,I}}^{u_{\xi,I}} \frac{d\bar{\omega}}{1 - n_{\xi,I}\mathrm{sn}\left[u_{\xi,I}, K_{\xi,I}\right]} \quad \textit{where} \quad n_{\xi,I} = -\frac{Z^2_{3,\xi}}{Y^*_{\xi,I}} \tag{5.134}$$

Equation (5.134) now takes the canonical form of an elliptic integral of the third kind. Consequently, its evaluation yields the closed-form solution for $\tau_{2,\xi,I}$:

$$\tau_{2,\xi,I} = \frac{\Pi\left[n_{\xi,I}, u_{\xi,I}, K_{\xi,I}\right] - \Pi\left[n_{\xi,I}, u_{\xi,0,I}, K_{\xi,I}\right]}{Y^*_{\xi,I}\sqrt{a_1} Z_{1,\xi}\bar{\delta}_{\xi,I}} \tag{5.135}$$

Equation (5.135) thus provides the explicit evolution of $\tau_{2,\xi,I}$ as a function of $\tau_1$ for Case $I$.

For Case $II$, the solution for $Z$ provided in Eq. (5.97) allows one to express $\xi$ as:

$$\xi_{II} = \sqrt{Y^*_{\xi,II} + Z^2_{2,\xi}\tanh^2\left[u_{\xi,II}\right]} \tag{5.136}$$

Substituting Eq. (5.136) into Eq. (5.128) yields the integral form:

$$\tau_{2,\xi,II} = \int_0^{\tau_1} \frac{d\tau_1}{Y^*_{\xi,II} + Z^2_{2,\xi} \tanh^2 [u_{\xi,II}]} \tag{5.137}$$

Although this integral is non-trivial, it can be evaluated symbolically to give a closed-form expression for $\tau_{2,\xi,II}$:

$$\tau_{2,\xi,I} = -\frac{\bar{I}[u_{\xi,I}] - \bar{I}[u_{\xi,0,I}]}{Y^*_{\xi,I}\sqrt{a_1} Z_{2,\xi} \bar{\delta}_{\xi,II}} \tag{5.138}$$

Here, $\bar{I}$ denotes the indefinite integral corresponding to Eq. (5.137), given explicitly by:

$$\bar{I}[u] = \begin{cases} \frac{u+\sqrt{n_{\xi,II}}\arctan\left(\sqrt{n_{\xi,II}}u\right)}{1+n_{\xi,II}} & \textit{If} \quad n_{\xi,II} > 0 \\ \frac{u-\sqrt{-n_{\xi,II}}\text{arctanh}\left(\sqrt{-n_{\xi,II}}u\right)}{1+n_{\xi,II}} & \textit{If} \quad n_{\xi,II} < 0 \end{cases} \quad \textit{where} \quad n_{\xi,II} = \frac{Z^2_{2,\xi}}{Y^*_{\xi,II}} \tag{5.139}$$

Equation (5.138) therefore provides the explicit evolution of $\tau_{2,\xi,II}$ as a function of $\tau_1$ for Case $II$.

For Case $III$, the solution for $Z$ given in Eq. (5.75) allows one to express $\xi$ as:

$$\xi_{III} = \sqrt{Y^*_{\xi,III} + \frac{Z^2_{1,\xi}}{\text{sn}^2 [u_{\xi,III}, K_{\xi,III}]}} \tag{5.140}$$

Substituting Eq. (5.140) into Eq. (5.128) leads to:

$$\tau_{2,\xi,III} = \int_0^{\tau_1} \frac{d\tau_1}{Y^*_{\xi,III} + \frac{Z^2_{1,\xi}}{\text{sn}^2[u_{\xi,III}, K_{\xi,III}]}} \tag{5.141}$$

Introducing the change of variable:

$$\bar{\omega} = u_{\xi,III} \quad \Rightarrow \quad d\bar{\omega} = -\sqrt{a_1} Z_{1,\xi} \bar{\delta}_{\xi,III} d\tau_1 \tag{5.142}$$

Equation (5.141) can be rewritten in the form:

$$\tau_{2,\xi,III} = -\frac{1}{\sqrt{a_1} Z^3_{1,\xi} \bar{\delta}_{\xi,III}} \int_{u_{\xi,0,III}}^{u_{\xi,III}} \frac{\text{sn}^2 [\bar{\omega}, K_{\xi,III}]\, d\bar{\omega}}{1 - n_{\xi,III} \text{sn}^2 [\bar{\omega}, K_{\xi,III}]} \quad \textit{where} \quad n_{\xi,III} = -\frac{Y^*_{\xi,III}}{Z^2_{1,\xi}} \tag{5.143}$$

According to [83], the solution of the integral in Eq. (5.143) is given by:

$$\int_0^u \frac{\text{sn}^2 [\bar{\omega}, K]\, d\bar{\omega}}{1 - n\text{sn}^2 [\bar{\omega}, K]} = \frac{1}{n} \left[\Pi [n, u, K] - F [u, K]\right] \tag{5.144}$$

Consequently, applying Eq. (5.144), the evolution of $\tau_{2,\xi,III}$ as a function of $\tau_1$ is as:

$$\tau_{2,\xi,III} = -\frac{\Pi [n_{\xi,III}, u_{\xi,III}, K_{\xi,III}] - F [u_{\xi,III}, K_{\xi,III}] - \Pi [n_{\xi,III}, u_{\xi,0,III}, K_{\xi,III}] + F [u_{\xi,0,III}, K_{\xi,III}]}{\sqrt{a_1} Z^3_{1,\xi} \bar{\delta}_{\xi,III} n_{\xi,III}} \tag{5.145}$$

Equation (5.145) thus provides the explicit evolution of $\tau_{2,\xi,III}$ with respect to $\tau_1$ for Case $III$.

For Case $IV$, the solution for $Z$ given in Eq. (5.122) allows one to express $\xi$ as:

$$\xi_{IV} = \sqrt{Y^*_{\xi,IV} + \lambda^2 \left(\frac{\text{sn}[u_{\xi,IV}, K_{\xi,IV}] - N\text{cn}[u_{\xi,IV}, K_{\xi,IV}]}{\text{sn}[u_{\xi,IV}, K_{\xi,IV}] + N\text{cn}[u_{\xi,IV}, K_{\xi,IV}]}\right)^2} \tag{5.146}$$

Substituting Eq. (5.146) into Eq. (5.128) yields:

$$\tau_{2,\xi,IV} = \int_0^{\tau_1} \frac{d\tau_1}{Y^*_{\xi,IV} + \lambda^2 \left(\frac{\text{sn}[u_{\xi,IV}, K_{\xi,IV}] - \bar{N}\text{cn}[u_{\xi,IV}, K_{\xi,IV}]}{\text{sn}[u_{\xi,IV}, K_{\xi,IV}] + \bar{N}\text{cn}[u_{\xi,IV}, K_{\xi,IV}]}\right)^2} \tag{5.147}$$

The integral in Eq. (5.147) defines the evolution of $\tau_{2,\xi,IV}$ with respect to $\tau_1$. However, due to the complexity of the integrand, closed-form analytical could not be obtained, and the expression is left in this integral form for subsequent derivations.

Integration of $\tau_{2,\eta}$

For the variable $\eta$, only Case $I$ is physically admissible. In this scenario, the solution for $Z$ given in Eq. (5.84) allows the variable $\eta$ to be expressed as:

$$\eta_I = \sqrt{Y^*_{\eta,I} - Z^2_{3,\eta}\mathrm{sn}^2\left[u_{\eta,I}, K_{\eta,I}\right]} \tag{5.148}$$

Here, $Y^*_{\eta,I}$ denotes the $Y^*$ constant associated with Case $I$ for the variable $\eta$. Substituting Eq. (5.148) into Eq. (5.129) yields:

$$\tau_{2,\eta,I} = \int_0^{\tau_1} \frac{d\tau_1}{Y^*_{\eta,I} - Z^2_{3,\eta}\mathrm{sn}^2\left[u_{\eta,I}, K_{\eta,I}\right]} \tag{5.149}$$

Introducing the change of variable:

$$\bar{\omega} = u_{\eta,I} \quad \Rightarrow \quad d\bar{\omega} = -\sqrt{-a_1} Z_{2,\eta} \bar{\delta}_{\eta,I} d\tau_1 \tag{5.150}$$

Equation (5.149) can be rewritten in the form:

$$\tau_{2,\eta,I} = -\frac{1}{Y^*_{\eta,I}\sqrt{-a_1} Z_{2,\eta}\bar{\delta}_{\eta,I}} \int_{u_{\eta,0,I}}^{u_{\eta,I}} \frac{d\bar{\omega}}{1 - n_{\eta,I}\mathrm{sn}\left[u_{\eta,I}, K_{\eta,I}\right]} \quad \textit{where} \quad n_{\eta,I} = \frac{Z^2_{3,\eta}}{Y^*_{\eta,I}} \tag{5.151}$$

The integral in Eq. (5.151) corresponds to an elliptic integral of the third kind, as defined in Eq. (5.132). Therefore, the solution for $\tau_{2,\eta,I}$ can be expressed as:

$$\tau_{2,\eta,I} = -\frac{\Pi\left[n_{\eta,I}, u_{\eta,I}, K_{\eta,I}\right] - \Pi\left[n_{\eta,I}, u_{\eta,0,I}, K_{\eta,I}\right]}{Y^*_{\eta,I}\sqrt{-a_1} Z_{2,\eta}\bar{\delta}_{\eta,I}} \tag{5.152}$$

Equation (5.152) provides the evolution of $\tau_{2,\eta,I}$ as a function of the fictitious time $\tau_1$.

### 5.4.4. Integration of $\tau_1$

Subsection 5.4.3 established the relation between the fictitious time variables $\tau_1$ and $\tau_2$, enabling the integration of the equations of motion with respect to $\tau_1$ as the independent variable. However, the connection between $\tau_1$ and the physical time $t$ remains to be determined. This subsection addresses the derivation of this relation, thereby permitting integration using the physical time $t$ as the independent variable.

Equation (5.5) provides the differential relation between $\tau_1$ and $t$. In general, the direct integration of this equation does not admit a closed-form solution. Accordingly, the inverse differential relation is considered:

$$dt = \left(\xi^2 + \eta^2\right) d\tau_1 \tag{5.153}$$

Analogous to the procedure employed for the integration of $\tau_2$, the variables $\xi$ and $\eta$ appear in separate terms on the right-hand side of Eq. (5.153). This separation allows each term to be integrated independently, yielding:

$$t = t_\xi\left(\tau_1\right) + t_\eta\left(\tau_1\right) \tag{5.154}$$

Equation (5.154) is referred to as the *Stark Equation*. This equation provides an implicit relation between the fictitious time $\tau_1$ and the physical time $t$. For a given value of $t$, the corresponding $\tau_1$ must be determined via an iterative procedure.

The Stark equation serves as the analogue of the Kepler equation in the classical Kepler problem, with the key distinction that it involves the evaluation of elliptic integrals rather than simple transcendental functions. Consequently, its computational cost is higher than that of the Kepler equation.

In Eq. (5.154), the functions $t_\xi$ and $t_\eta$ are defined as:

$$t_\xi = \int_0^{\tau_1} \xi^2 d\tau_1 \tag{5.155}$$

$$t_\eta = \int_0^{\tau_1} \eta^2 d\tau_1 \tag{5.156}$$

As in the case of $\tau_2$, the integration can be performed independently for $\xi$ and $\eta$. Different forms of $t_\xi$ and $t_\eta$ arise depending on the value of the determinant $D$ of the associated cubic equation, reflecting the distinct solution regimes for the motion.

### Integration of $t_\xi$

For the variable $\xi$, the four cases depending on the value of the discriminant $D$ and the initial conditions must be integrated.

For Case $I$, substituting the solution for $\xi$ from Eq. (5.130) into Eq. (5.155) yields:

$$t_{\xi,I} = \int_0^{\tau_1} \left(Y^*_{\xi,I} + Z^2_{3,\xi}\mathrm{sn}^2\left[u_{\xi,I}, K_{\xi,I}\right]\right) d\tau_1 \tag{5.157}$$

The term involving the constant $Y^*_{\xi,I}$ integrates trivially. The second term, containing the squared Jacobi elliptic sine, can be integrated using the standard result in [83]:

$$\int_0^u \mathrm{sn}^2\left[\bar{\omega}, K\right] d\bar{\omega} = \frac{1}{K^2}\left[u - E\left[u, K\right]\right] \tag{5.158}$$

Here, $E$ denotes the elliptic integral of the second kind. Applying the solution for the integral in Eq. (5.158), the solution for $t_{\xi,I}$ is obtained as:

$$t_{\xi,I} = Y^*_{\xi,I}\tau_1 + \frac{Z^2_{3,\xi}}{\sqrt{a_1}Z_{1,\xi}\bar{\delta}_{\xi,I}K^2_{\xi,I}}\left[u_{\xi,I} - E\left[u_{\xi,I}, K_{\xi,I}\right] - u_{\xi,0,I} + E\left[u_{\xi,0,I}, K_{\xi,I}\right]\right] \tag{5.159}$$

Equation (5.159) gives the evolution of $t_{\xi,I}$ with $\tau_1$.

For Case $II$, substituting the solution for $\xi$ from Eq. (5.136) into Eq. (5.155) yields:

$$t_{\xi,II} = \int_0^{\tau_1} \left(Y^*_{\xi,II} + Z^2_{2,\xi}\tanh^2\left[u_{\xi,II}\right]\right) d\tau_1 \tag{5.160}$$

Integral in Eq. (5.160) only involves transcendental functions. Therefore, the integration is immediate and is given by:

$$t_{\xi,II} = Y^*_{\xi,II}\tau_1 - \frac{Z_{2,\xi}}{\sqrt{a_1}\bar{\delta}_{\xi,II}}\left[u_{\xi,II} - \tanh\left[u_{\xi,II}\right] - u_{\xi,0,II} + \tanh\left[u_{\xi,0,II}\right]\right] \tag{5.161}$$

Equation (5.161) provides the evolution of $t_{\xi,II}$ as a function of the fictitious time $\tau_1$.

For Case $III$, substituting the solution for $\xi$ from Eq. (5.140) into Eq. (5.155) gives:

$$t_{\xi,III} = \int_0^{\tau_1} \left(Y^*_{\xi,III} + \frac{Z^2_{1,\xi}}{\mathrm{sn}^2\left[u_{\xi,III}, K_{\xi,III}\right]}\right) d\tau_1 \tag{5.162}$$

In Eq. (5.162), since $Y^*_{\xi,III}$ is constant, its integration is immediate. The second term involves the reciprocal of a squared Jacobi elliptic sine function. According to [83], its integral is given by:

$$\int_0^u \frac{d\bar{\omega}}{\mathrm{sn}^2\left[u, K\right]} = u - E\left[u, K\right] - \frac{\mathrm{dn}\left[u, K\right]\mathrm{cn}\left[u, K\right]}{\mathrm{sn}\left[u, K\right]} \tag{5.163}$$

Applying the solution for the integral in Eq. (5.163), the solution for $t_{\xi,III}$ is obtained as:

$$\begin{aligned} t_{\xi,III} = Y^*_{\xi,III}\tau_1 - \frac{Z_{1,\xi}}{\sqrt{a_1}\delta_{\xi,III}}\Bigg[u_{\xi,III} - E\left[u_{\xi,III}, K_{\xi,III}\right] - \frac{\mathrm{dn}\left[u_{\xi,III}, K_{\xi,III}\right]\mathrm{cn}\left[u_{\xi,III}, K_{\xi,III}\right]}{\mathrm{sn}\left[u_{\xi,III}, K_{\xi,III}\right]} \\ - u_{\xi,0,III} + E\left[u_{\xi,0,III}, K_{\xi,III}\right] + \frac{\mathrm{dn}\left[u_{\xi,0,III}, K_{\xi,III}\right]\mathrm{cn}\left[u_{\xi,0,III}, K_{\xi,III}\right]}{\mathrm{sn}\left[u_{\xi,0,III}, K_{\xi,III}\right]}\Bigg] \end{aligned} \tag{5.164}$$

Equation (5.164) describes the evolution of $t_{\xi,III}$ as a function of the fictitious time $\tau_1$.

For Case $IV$, substituting the solution for $\xi$ from Eq. (5.146) into Eq. (5.155) yields:

$$t_{\xi,IV} = \int_0^{\tau_1} \left(Y^*_{\xi,IV} + \lambda^2\left(\frac{\mathrm{sn}\left[u_{\xi,IV}, K_{\xi,IV}\right] - \bar{N}\mathrm{cn}\left[u_{\xi,IV}, K_{\xi,IV}\right]}{\mathrm{sn}\left[u_{\xi,IV}, K_{\xi,IV}\right] + \bar{N}\mathrm{cn}\left[u_{\xi,IV}, K_{\xi,IV}\right]}\right)^2\right) d\tau_1 \tag{5.165}$$

In Eq. (5.165), the integral of the constant term $Y^*_{\xi,IV}$ is immediate. The remaining term involves a non-trivial combination of Jacobi elliptic functions. Although its structure suggests that an analytical solution may exist, no closed-form expression has been identified in the present work. Therefore, the integral is retained in its unevaluated form to preserve the exactness of the representation.

Equation (5.165) provides an implicit relation for the evolution of $t_{\xi,IV}$ as a function of the fictitious time $\tau_1$.

Integration of $t_\eta$

For the variable $\eta$, only Case $I$ is physically admissible. Substituting the solution for $\eta$ from Eq. (5.148) into Eq. (5.156) yields:

$$t_{\eta,I} = \int_0^{\tau_1} \left(Y^*_{\eta,I} - Z^2_{3,\eta}\mathrm{sn}^2\left[u_{\eta,I}, K_{\eta,I}\right]\right) d\tau_1 \tag{5.166}$$

The integral in Eq. (5.166) has the same form as that for $t_{\xi,I}$ in Eq. (5.157). Utilizing the standard result for the integral of the squared Jacobi elliptic sine in Eq. (5.158), the solution can be written as:

$$t_{\eta,I} = Y^*_{\eta,I}\tau_1 + \frac{Z^2_{3,\eta}}{\sqrt{-a_1}Z_{2,\eta}\delta_{\eta,I}K^2_{\eta,I}}\left[u_{\eta,I} - E\left[u_{\eta,I}, K_{\eta,I}\right] - u_{\eta,0,I} + E\left[u_{\eta,0,I}, K_{\eta,I}\right]\right] \tag{5.167}$$

Equation (5.167) provides the evolution of $t_{\eta,I}$ as a function of the fictitious time $\tau_1$, thereby completing the integration for the $\eta$ coordinate.

## 5.5. Summary of Solutions

In Section 5.4, the integration of the equations of motion for the Stark problem was performed. The solutions obtained exhibit distinct behaviors depending on the initial conditions and the magnitude of the perturbing acceleration. This section consolidates the results, presenting all necessary expressions to propagate each case, and provides a concise discussion of the physical and mathematical characteristics of the solutions.

### 5.5.1. Case $I$

The evolution of the state variables for Case $I$ is described by the set $(\xi_I, \eta_I, \phi)$ and their corresponding time derivatives:

$$\begin{aligned}
\xi_I &= \sqrt{Y^*_{\xi,I} + Z^2_{3,\xi}\mathrm{sn}^2\left[u_{\xi,I}, K_{\xi,I}\right]} \\
\eta_I &= \sqrt{Y^*_{\eta,I} - Z^2_{3,\eta}\mathrm{sn}^2\left[u_{\eta,I}, K_{\eta,I}\right]} \\
\phi &= \phi_0 + p_\phi \tau_{2,I} \\
\dot{\xi}_I &= \frac{\sqrt{\epsilon}Z_{1,\xi}Z^2_{3,\xi}\bar{\delta}_{\xi,I}\mathrm{sn}\left[u_{\xi,I}, K_{\xi,I}\right]\mathrm{cn}\left[u_{\xi,I}, K_{\xi,I}\right]\mathrm{dn}\left[u_{\xi,I}, K_{\xi,I}\right]}{\xi_I\left(\xi_I^2 + \eta_I^2\right)} \\
\dot{\eta}_I &= \frac{\sqrt{\epsilon}Z_{2,\eta}Z^2_{3,\eta}\bar{\delta}_{\eta,I}\mathrm{sn}\left[u_{\eta,I}, K_{\eta,I}\right]\mathrm{cn}\left[u_{\eta,I}, K_{\eta,I}\right]\mathrm{dn}\left[u_{\eta,I}, K_{\eta,I}\right]}{\eta_I\left(\xi_I^2 + \eta_I^2\right)} \\
\dot{\phi} &= \frac{p_\phi}{\xi_I^2\eta_I^2}
\end{aligned} \tag{5.168}$$

In Eq. (5.168), the leading coefficient of the cubic polynomial, $a_1$, has been substituted by its relationship with $\epsilon$. To propagate Eq. (5.168), the relations between the fictitious times and the physical time are required:

$$\begin{aligned}
\tau_{2,I} &= \frac{\Pi\left[n_{\xi,I}, u_{\xi,I}, K_{\xi,I}\right] - \Pi\left[n_{\xi,I}, u_{\xi,0,I}, K_{\xi,I}\right]}{Y^*_{\xi,I}\sqrt{\epsilon}Z_{1,\xi}\bar{\delta}_{\xi,I}} - \frac{\Pi\left[n_{\eta,I}, u_{\eta,I}, K_{\eta,I}\right] - \Pi\left[n_{\eta,I}, u_{\eta,0,I}, K_{\eta,I}\right]}{Y^*_{\eta,I}\sqrt{\epsilon}Z_{2,\eta}\bar{\delta}_{\eta,I}} \\
t_I &= \left(Y^*_{\xi,I} + Y^*_{\eta,I}\right)\tau_1 + \frac{Z^2_{3,\xi}}{\sqrt{\epsilon}Z_{1,\xi}\delta_{\xi,I}K^2_{\xi,I}}\left[u_{\xi,I} - E\left[u_{\xi,I}, K_{\xi,I}\right] - u_{\xi,0,I} + E\left[u_{\xi,0,I}, K_{\xi,I}\right]\right] \\
&\quad + \frac{Z^2_{3,\eta}}{\sqrt{\epsilon}Z_{2,\eta}\delta_{\eta,I}K^2_{\eta,I}}\left[u_{\eta,I} - E\left[u_{\eta,I}, K_{\eta,I}\right] - u_{\eta,0,I} + E\left[u_{\eta,0,I}, K_{\eta,I}\right]\right]
\end{aligned} \tag{5.169}$$

Equations (5.168) and (5.169) are functions of the following parameters:

$$\begin{aligned}
K_{\xi,I} &= \frac{Z_{3,\xi}}{Z_{1,\xi}} \\
K_{\eta,I} &= \frac{Z_{3,\eta}}{Z_{2,\eta}} \\
n_{\xi,I} &= -\frac{Z_{3,\xi}^2}{Y_{\xi,I}^*} \\
n_{\eta,I} &= \frac{Z_{3,\eta}^2}{Y_{\eta,I}^*} \\
u_{\xi,I} &= \sqrt{\epsilon} Z_{1,\xi} \left(\bar{\delta}_{\xi,I}\tau_1 - \tau_{1,\xi,0,I}\right) \\
u_{\eta,I} &= -\sqrt{\epsilon} Z_{2,\eta} \left(\bar{\delta}_{\eta,I}\tau_1 - \tau_{1,\eta,0,I}\right) \\
u_{\xi,0,I} &= -\sqrt{\epsilon} Z_{1,\xi}\tau_{1,\xi,0,I} \\
u_{\eta,0,I} &= \sqrt{\epsilon} Z_{1,\eta}\tau_{1,\eta,0,I} \\
\bar{\delta}_{\xi,I} &= sign\left(\dot{\xi}_{0,I}\mathrm{sn}\left[u_{\xi,0,I}, K_{\xi,I}\right]\mathrm{cn}\left[u_{\xi,0,I}, K_{\xi,I}\right]\right) \\
\bar{\delta}_{\eta,I} &= sign\left(\dot{\eta}_{0,I}\mathrm{sn}\left[u_{\eta,0,I}, K_{\eta,I}\right]\mathrm{cn}\left[u_{\eta,0,I}, K_{\eta,I}\right]\right) \\
\tau_{1,\xi,0,I} &= -\frac{1}{\sqrt{\epsilon} Z_{1,\xi}} F\left[\frac{Z_{\xi,I,0}}{Z_{3,\xi}}, K_{\xi,I}\right] \\
\tau_{1,\eta,0,I} &= \frac{1}{\sqrt{\epsilon} Z_{2,\eta}} F\left[\frac{Z_{\eta,0,I}}{Z_{3,\eta}}, K_{\eta,I}\right]
\end{aligned} \tag{5.170}$$

Since the Jacobi elliptic functions are periodic, the solution for Case $I$ corresponds to bounded, periodic motion. Therefore, this case represents the Stark problem analogue of the elliptic motion in the classical Kepler problem.

### 5.5.2. Case $II$

The evolution of the state variables for Case $II$ is described by the set $(\xi_{II}, \eta_I, \phi)$ and their corresponding derivatives:

$$\begin{aligned}
\xi_{II} &= \sqrt{Y_{\xi,II}^* + Z_{2,\xi}^2 \tanh^2\left[u_{\xi,II}\right]} \\
\eta_I &= \sqrt{Y_{\eta,I}^* - Z_{3,\eta}^2 \mathrm{sn}^2\left[u_{\eta,I}, K_{\eta,I}\right]} \\
\phi &= \phi_0 + p_\phi \tau_{2,II} \\
\dot{\xi}_{II} &= -\frac{\sqrt{\epsilon} Z_{2,\xi}^3 \bar{\delta}_{\xi,II} \tanh\left[u_{\xi,II}\right]\left(1 - \tanh^2\left[u_{\xi,II}\right]\right)}{\xi_{II}\left(\xi_{II}^2 + \eta_I^2\right)} \\
\dot{\eta}_I &= \frac{\sqrt{\epsilon} Z_{2,\eta} Z_{3,\eta}^2 \bar{\delta}_{\eta,I} \mathrm{sn}\left[u_{\eta,I}, K_{\eta,I}\right]\mathrm{cn}\left[u_{\eta,I}, K_{\eta,I}\right]\mathrm{dn}\left[u_{\eta,I}, K_{\eta,I}\right]}{\eta_I\left(\xi_{II}^2 + \eta_I^2\right)} \\
\dot{\phi} &= \frac{p_\phi}{\xi_{II}^2 \eta_I^2}
\end{aligned} \tag{5.171}$$

The corresponding relations between the fictitious times and the physical time are:

$$\begin{aligned}
\tau_{2,II} &= -\frac{\bar{I}\left[u_{\xi,II}\right] - \bar{I}\left[u_{\xi,0,II}\right]}{Y_{\xi,II}^* \sqrt{\epsilon} Z_{2,\xi} \bar{\delta}_{\xi,II}} - \frac{\Pi\left[n_{\eta,I}, u_{\eta,I}, K_{\eta,I}\right] - \Pi\left[n_{\eta,I}, u_{\eta,0,I}, K_{\eta,I}\right]}{Y_{\eta,I}^* \sqrt{\epsilon} Z_{2,\eta} \bar{\delta}_{\eta,I}} \\
t_{II} &= \left(Y_{\xi,II}^* + Y_{\eta,I}^*\right)\tau_1 - \frac{Z_{2,\xi}}{\sqrt{\epsilon}\bar{\delta}_{\xi,II}}\left[u_{\xi,II} - \tanh\left[u_{\xi,II}\right] - u_{\xi,0,II} + \tanh\left[u_{\xi,0,II}\right]\right] \\
&\quad + \frac{Z_{3,\eta}^2}{\sqrt{\epsilon} Z_{2,\eta} \delta_{\eta,I} K_{\eta,I}^2}\left[u_{\eta,I} - E\left[u_{\eta,I}, K_{\eta,I}\right] - u_{\eta,0,I} + E\left[u_{\eta,0,I}, K_{\eta,I}\right]\right]
\end{aligned} \tag{5.172}$$

Equations (5.171) and (5.172) are functions of the following parameters:

$$
\begin{aligned}
K_{\eta,I} &= \frac{Z_{3,\eta}}{Z_{2,\eta}} \\
n_{\xi,II} &= \frac{Z_{2,\xi}^2}{Y_{\xi,II}^*} \\
n_{\eta,I} &= \frac{Z_{3,\eta}^2}{Y_{\eta,I}^*} \\
u_{\xi,II} &= -\sqrt{\epsilon} Z_{2,\xi} \left( \bar{\delta}_{\xi,II} \tau_1 - \tau_{1,\xi,0,II} \right) \\
u_{\eta,I} &= -\sqrt{\epsilon} Z_{2,\eta} \left( \bar{\delta}_{\eta,I} \tau_1 - \tau_{1,\eta,0,I} \right) \\
u_{\xi,0,II} &= \sqrt{\epsilon} Z_{2,\xi} \tau_{1,\xi,0,II} \\
u_{\eta,0,I} &= \sqrt{\epsilon} Z_{1,\eta} \tau_{1,\eta,0,I} \\
\bar{\delta}_{\xi,II} &= sign \left( \dot{\xi}_{0,II} Z_{2,\xi} \tanh \left[ u_{\xi,0,II} \right] \right) \\
\bar{\delta}_{\eta,I} &= sign \left( \dot{\eta}_{0,I} \mathrm{sn} \left[ u_{\eta,0,I}, K_{\eta,I} \right] \mathrm{cn} \left[ u_{\eta,0,I}, K_{\eta,I} \right] \right) \\
\tau_{1,\xi,0,II} &= -\frac{1}{\sqrt{\epsilon} Z_{2,\xi}} \mathrm{arctanh} \left( \frac{Z_{\xi,0,II}^2}{Z_{2,\xi}^2} - 1 \right) \\
\tau_{1,\eta,0,I} &= \frac{1}{\sqrt{\epsilon} Z_{2,\eta}} F \left[ \frac{Z_{\eta,0,I}}{Z_{3,\eta}}, K_{\eta,I} \right] \\
\bar{I}\left[ u \right] &= \begin{cases} \frac{u + \sqrt{n_{\xi,II}} \arctan\left( \sqrt{n_{\xi,II}} u \right)}{1 + n_{\xi,II}} & \textit{If} \quad n_{\xi,II} > 0 \\ \frac{u - \sqrt{-n_{\xi,II}} \mathrm{arctanh}\left( \sqrt{-n_{\xi,II}} u \right)}{1 + n_{\xi,II}} & \textit{If} \quad n_{\xi,II} < 0 \end{cases} \quad \textit{where} \quad n_{\xi,II} = \frac{Z_{2,\xi}^2}{Y_{\xi,II}^*}
\end{aligned}
\tag{5.173}
$$

Since $\tanh\left[u\right] \in [-1, 1]$ for $u \in (-\infty, \infty)$, Eq. (5.171) indicates that the solution for Case $II$ corresponds to bounded, asymptotic motion: $\xi$ evolves toward a finite asymptotic value, while $\eta$ remains periodic. Moreover, because $\bar{I}$ involves the $\mathrm{arctanh}\left[u\right]$ function, defined only for $u \in (-1, 1)$, the entire range of physical times $t$ is mapped to a finite range of the fictitious time $\tau_1$.

Therefore, Case $II$ represents the analogue of the parabolic trajectory in the Kepler problem. The key distinction is that, unlike the unbounded parabolic motion in the Kepler problem, the Stark problem yields a bounded trajectory, with one coordinate asymptotically approaching a finite value while the other remains periodic.

### 5.5.3. Case $III$

The evolution of solutions corresponding to Case $III$ is described by the set $(\xi_{III}, \eta_I, \phi)$ and their derivatives:

$$
\begin{aligned}
\xi_{III} &= \sqrt{Y_{\xi,III}^* + \frac{Z_{1,\xi}^2}{\mathrm{sn}^2\left[u_{\xi,III}, K_{\xi,III}\right]}} \\
\eta_I &= \sqrt{Y_{\eta,I}^* - Z_{3,\eta}^2 \mathrm{sn}^2\left[u_{\eta,I}, K_{\eta,I}\right]} \\
\phi &= \phi_0 + p_\phi \tau_{2,III} \\
\dot{\xi}_{III} &= \frac{\sqrt{\epsilon} Z_{1,\xi}^3 \bar{\delta}_{\xi,III} \mathrm{cn}\left[u_{\xi,III}, K_{\xi,III}\right] \mathrm{dn}\left[u_{\xi,III}, K_{\xi,III}\right]}{\xi_{III} \left(\xi_{III}^2 + \eta_I^2\right) \mathrm{sn}^3\left[u_{\xi,III}, K_{\xi,III}\right]} \\
\dot{\eta}_I &= \frac{\sqrt{\epsilon} Z_{2,\eta} Z_{3,\eta}^2 \bar{\delta}_{\eta,I} \mathrm{sn}\left[u_{\eta,I}, K_{\eta,I}\right] \mathrm{cn}\left[u_{\eta,I}, K_{\eta,I}\right] \mathrm{dn}\left[u_{\eta,I}, K_{\eta,I}\right]}{\eta_I \left(\xi_{III}^2 + \eta_I^2\right)} \\
\dot{\phi} &= \frac{p_\phi}{\xi_{III}^2 \eta_I^2}
\end{aligned}
\tag{5.174}
$$

Propagation of Eq. (5.174) requires the relations between the fictitious times and the physical time, which are expressed as:

$$\begin{aligned}
\tau_{2,III} = &-\frac{\Pi\left[n_{\xi,III}, u_{\xi,III}, K_{\xi,III}\right] - F\left[u_{\xi,III}, K_{\xi,III}\right] - \Pi\left[n_{\xi,III}, u_{\xi,0,III}, K_{\xi,III}\right] + F\left[u_{\xi,0,III}, K_{\xi,III}\right]}{\sqrt{\epsilon} Z_{1,\xi}^3 \bar{\delta}_{\xi,III} n_{\xi,III}} \\
&- \frac{\Pi\left[n_{\eta,I}, u_{\eta,I}, K_{\eta,I}\right] - \Pi\left[n_{\eta,I}, u_{\eta,0,I}, K_{\eta,I}\right]}{Y_{\eta,I}^* \sqrt{\epsilon} Z_{2,\eta} \bar{\delta}_{\eta,I}} \\
t_{III} = &\left(Y_{\xi,III}^* + Y_{\eta,I}^*\right)\tau_1 - \frac{Z_{1,\xi}}{\sqrt{\epsilon}\delta_{\xi,III}}\left[u_{\xi,III} - E\left[u_{\xi,III}, K_{\xi,III}\right] - \frac{\mathrm{dn}\left[u_{\xi,III}, K_{\xi,III}\right]\mathrm{cn}\left[u_{\xi,III}, K_{\xi,III}\right]}{\mathrm{sn}\left[u_{\xi,III}, K_{\xi,III}\right]}\right. \\
&\left. - u_{\xi,0,III} + E\left[u_{\xi,0,III}, K_{\xi,III}\right] + \frac{\mathrm{dn}\left[u_{\xi,0,III}, K_{\xi,III}\right]\mathrm{cn}\left[u_{\xi,0,III}, K_{\xi,III}\right]}{\mathrm{sn}\left[u_{\xi,0,III}, K_{\xi,III}\right]}\right] \\
&+ \frac{Z_{3,\eta}^2}{\sqrt{\epsilon} Z_{2,\eta}\delta_{\eta,I} K_{\eta,I}^2}\left[u_{\eta,I} - E\left[u_{\eta,I}, K_{\eta,I}\right] - u_{\eta,0,I} + E\left[u_{\eta,0,I}, K_{\eta,I}\right]\right]
\end{aligned} \tag{5.175}$$

Equations (5.174) and (5.175) depend on the following variables and parameters:

$$\begin{aligned}
K_{\xi,III} &= \frac{Z_{3,\xi}}{Z_{1,\xi}} \\
K_{\eta,I} &= \frac{Z_{3,\eta}}{Z_{2,\eta}} \\
n_{\xi,III} &= -\frac{Y_{\xi,III}^*}{Z_{1,\xi}^2} \\
n_{\eta,I} &= \frac{Z_{3,\eta}^2}{Y_{\eta,I}^*} \\
u_{\xi,III} &= -\sqrt{\epsilon} Z_{1,\xi}\left(\bar{\delta}_{\xi,III}\tau_1 - \tau_{1,\xi,0,III}\right) \\
u_{\eta,I} &= -\sqrt{\epsilon} Z_{2,\eta}\left(\bar{\delta}_{\eta,I}\tau_1 - \tau_{1,\eta,0,I}\right) \\
u_{\xi,0,III} &= \sqrt{\epsilon} Z_{1,\xi}\tau_{1,\xi,0,III} \\
u_{\eta,0,I} &= \sqrt{\epsilon} Z_{1,\eta}\tau_{1,\eta,0,I} \\
\bar{\delta}_{\xi,III} &= sign\left(\dot{\xi}_{0,III}\mathrm{sn}\left[u_{\xi,0,III}, K_{\xi,III}\right]\mathrm{cn}\left[u_{\xi,0,III}, K_{\xi,III}\right]\right) \\
\bar{\delta}_{\eta,I} &= sign\left(\dot{\eta}_{0,I}\mathrm{sn}\left[u_{\eta,0,I}, K_{\eta,I}\right]\mathrm{cn}\left[u_{\eta,0,I}, K_{\eta,I}\right]\right) \\
\tau_{1,\xi,0,III} &= \frac{1}{\sqrt{\epsilon} Z_{1,\xi}} F\left[\frac{Z_{1,\xi}}{Z_{\xi,III,0}}, K_{\xi,III}\right] \\
\tau_{1,\eta,0,I} &= \frac{1}{\sqrt{\epsilon} Z_{2,\eta}} F\left[\frac{Z_{\eta,0,I}}{Z_{3,\eta}}, K_{\eta,I}\right]
\end{aligned} \tag{5.176}$$

Equation (5.174) indicates that Case $III$ corresponds to unbounded motion. In particular, because $\mathrm{sn}\left[u_{\xi,III}, K_{\xi,III}\right]$ appears in the denominator, the physical time $t$ spans an infinite range while the corresponding fictitious time $\tau_1$ remains finite, analogous to Case $II$. Consequently, Case $III$ represents the hyperbolic analogue in the Stark problem, corresponding to the unbounded hyperbolic trajectories in the Kepler problem.

### 5.5.4. Case $IV$

The evolution of solutions corresponding to Case $IV$ is described by the set $(\xi_{IV}, \eta_I, \phi)$ and their derivatives:

$$\begin{aligned}
\xi_{IV} &= \sqrt{Y^*_{\xi,IV} + \lambda^2 \left( \frac{\mathrm{sn}\left[u_{\xi,IV}, K_{\xi,IV}\right] - \bar{N}\mathrm{cn}\left[u_{\xi,IV}, K_{\xi,IV}\right]}{\mathrm{sn}\left[u_{\xi,IV}, K_{\xi,IV}\right] + \bar{N}\mathrm{cn}\left[u_{\xi,IV}, K_{\xi,IV}\right]} \right)^2} \\
\eta_I &= \sqrt{Y^*_{\eta,I} - Z^2_{3,\eta}\mathrm{sn}^2\left[u_{\eta,I}, K_{\eta,I}\right]} \\
\phi &= \phi_0 + p_\phi \tau_{2,IV} \\
\dot{\xi}_{IV} &= \frac{\sqrt{\epsilon}\lambda\bar{N}\bar{M}^2\bar{\delta}_{\xi,IV}\mathrm{dn}\left[u_{\xi,IV}, K_{\xi,IV}\right]\left(\mathrm{sn}\left[u_{\xi,IV}, K_{\xi,IV}\right] - \bar{N}\mathrm{cn}\left[u_{\xi,IV}, K_{\xi,IV}\right]\right)}{2\xi_{IV}\left(\xi^2_{IV} + \eta^2_I\right)\left(\mathrm{sn}\left[u_{\xi,IV}, K_{\xi,IV}\right] + \bar{N}\mathrm{cn}\left[u_{\xi,IV}, K_{\xi,IV}\right]\right)^3} \\
\dot{\eta}_I &= \frac{\sqrt{\epsilon}Z_{2,\eta}Z^2_{3,\eta}\bar{\delta}_{\eta,I}\mathrm{sn}\left[u_{\eta,I}, K_{\eta,I}\right]\mathrm{cn}\left[u_{\eta,I}, K_{\eta,I}\right]\mathrm{dn}\left[u_{\eta,I}, K_{\eta,I}\right]}{\eta_I\left(\xi^2_{IV} + \eta^2_I\right)} \\
\dot{\phi} &= \frac{p_\phi}{\xi^2_{IV}\eta^2_I}
\end{aligned} \tag{5.177}$$

Propagation of Eq. (5.177) requires the relation between the fictitious times and the physical time, given by:

$$\begin{aligned}
\tau_{2,IV} &= \int_0^{\tau_1} \frac{d\tau_1}{Y^*_{\xi,IV} + \lambda^2\left(\frac{\mathrm{sn}[u_{\xi,IV},K_{\xi,IV}] - \bar{N}\mathrm{cn}[u_{\xi,IV},K_{\xi,IV}]}{\mathrm{sn}[u_{\xi,IV},K_{\xi,IV}] + \bar{N}\mathrm{cn}[u_{\xi,IV},K_{\xi,IV}]}\right)^2} - \frac{\Pi\left[n_{\eta,I}, u_{\eta,I}, K_{\eta,I}\right] - \Pi\left[n_{\eta,I}, u_{\eta,0,I}, K_{\eta,I}\right]}{Y^*_{\eta,I}\sqrt{\epsilon}Z_{2,\eta}\bar{\delta}_{\eta,I}} \\
t_{IV} &= \left(Y^*_{\xi,IV} + Y^*_{\eta,I}\right)\tau_1 + \int_0^{\tau_1} \lambda^2\left(\frac{\mathrm{sn}\left[u_{\xi,IV}, K_{\xi,IV}\right] - \bar{N}\mathrm{cn}\left[u_{\xi,IV}, K_{\xi,IV}\right]}{\mathrm{sn}\left[u_{\xi,IV}, K_{\xi,IV}\right] + \bar{N}\mathrm{cn}\left[u_{\xi,IV}, K_{\xi,IV}\right]}\right)^2 d\tau_1 \\
&\quad + \frac{Z^2_{3,\eta}}{\sqrt{\epsilon}Z_{2,\eta}\delta_{\eta,I}K^2_{\eta,I}}\left[u_{\eta,I} - E\left[u_{\eta,I}, K_{\eta,I}\right] - u_{\eta,0,I} + E\left[u_{\eta,0,I}, K_{\eta,I}\right]\right]
\end{aligned} \tag{5.178}$$

Equations (5.177) and (5.178) are functions of the following parameters:

$$\begin{aligned}
K_{\xi,IV} &= \sqrt{1 - \frac{1}{\bar{N}^4}} \\
K_{\eta,I} &= \frac{Z_{3,\eta}}{Z_{2,\eta}} \\
n_{\eta,I} &= \frac{Z^2_{3,\eta}}{Y^*_{\eta,I}} \\
u_{\xi,IV} &= \sqrt{\epsilon}\frac{\bar{M}^2}{2\lambda}\left(\bar{\delta}_{\xi,IV}\tau_1 - \tau_{1,\xi,0,IV}\right) \\
u_{\eta,I} &= -\sqrt{\epsilon}Z_{2,\eta}\left(\bar{\delta}_{\eta,I}\tau_1 - \tau_{1,\eta,0,I}\right) \\
u_{\xi,0,IV} &= -\sqrt{\epsilon}\frac{\bar{M}^2}{2\lambda}\tau_{1,\xi,0,IV} \\
u_{\eta,0,I} &= \sqrt{\epsilon}Z_{1,\eta}\tau_{1,\eta,0,I} \\
\bar{\delta}_{\xi,IV} &= sign\left(\dot{\xi}_{0,IV}\bar{N}\left(\mathrm{sn}^2\left[u_{\xi,0,IV}, K_{\xi,IV}\right] - \bar{N}^2\mathrm{cn}^2\left[u_{\xi,0,IV}, K_{\xi,IV}\right]\right)\right) \\
\bar{\delta}_{\eta,I} &= sign\left(\dot{\eta}_{0,I}\mathrm{sn}\left[u_{\eta,0,I}, K_{\eta,I}\right]\mathrm{cn}\left[u_{\eta,0,I}, K_{\eta,I}\right]\right) \\
\tau_{1,\xi,0,IV} &= \frac{2\lambda}{\sqrt{\epsilon}\bar{M}^2}F\left[\frac{\bar{N}\frac{\lambda + Z_{\xi,0,IV}}{\lambda - Z_{\xi,0,IV}}}{\sqrt{1 + \bar{N}^2\left(\frac{\lambda + Z_{\xi,0,IV}}{\lambda - Z_{\xi,0,IV}}\right)^2}}, K_{\xi,IV}\right] \\
\tau_{1,\eta,0,I} &= \frac{1}{\sqrt{\epsilon}Z_{2,\eta}}F\left[\frac{Z_{\eta,0,I}}{Z_{3,\eta}}, K_{\eta,I}\right]
\end{aligned} \tag{5.179}$$

Equation (5.177) indicates that Case $IV$ corresponds to unbounded motion. Unlike previous cases, the integral appearing in $\tau_{2,IV}$ and $t_{IV}$ involves a non-trivial combination of Jacobi elliptic functions for which no closed-form expression could be obtained. Therefore, these relations are left in integral form, representing an implicit dependence of the fictitious and physical times on $\tau_1$. As in Case $III$, Case $IV$ corresponds to hyperbolic-type solutions in the Stark problem, analogous to the hyperbolic trajectories in the Kepler problem.

# 6

# Research Paper

AAS XX-XXX

# ANALYTICAL PLANET-CENTRED SOLAR-SAIL TRAJECTORY PREDICTION WITH THE STARK MODEL

**Federico Fructuoso Vidal-Aragón***

Planet-centred solar sailing offers a propellantless way of sustaining non-Keplerian motion for Earth-centred missions. For preliminary mission design and broad trade-space exploration, rapid yet accurate trajectory propagation tools are required. This work evaluates the performance of the Stark model, an analytical formulation that represents the dynamics as two-body motion subject to a uniform perturbing acceleration, applied to controlled solar-sail trajectories and benchmarked against classical numerical integration. Two control strategies for the sail are considered: (i) constant cone-angle laws, for which the Stark solution enables direct state evaluation, and (ii) time-varying locally optimal steering laws designed to target individual Keplerian elements. Performance is assessed in terms of positional accuracy and computational cost over representative one-day propagations. For constant control laws, accuracy is shown to improve with increasing perturbation magnitude, corresponding to larger sail lightness numbers and smaller cone angles. Sensitivity analyses reveal that smaller semi-major axes and larger eccentricities lead to faster dynamical regimes, resulting in increased position error and higher computational cost. For time-varying control laws, the Stark model's performance depends strongly on the smoothness of the control law: smooth profiles (semi-major axis-, eccentricity-, and argument of periapsis-raising) yield broader regions of superiority in the accuracy-cost trade space compared to numerical integration, whereas abrupt profiles (inclination- and right ascension of the ascending node-raising) significantly reduce these regions. Furthermore, larger lightness numbers diminish the model's ability to capture rapid dynamics, owing to the restriction of fixed step sizes. Overall, the results demonstrate that the Stark model provides a computationally efficient alternative for preliminary planet-centred solar-sail trajectory design, with advantages over classical numerical integration methods in specific regions of the accuracy-cost trade-off space, particularly for smooth control regimes.

## INTRODUCTION

Solar sailing has emerged as a relevant propulsion concept due to its propellantless nature. The mechanism relies on solar radiation pressure (SRP), whereby incident solar photons reflect off the sail surface, imparting momentum to the spacecraft.[1] While the majority of research to date has focused on heliocentric applications, there is growing interest in planet-centred solar sailing. In this context, SRP can be exploited to achieve sustained non-Keplerian behaviour, enabling concepts such as displaced orbits, pole-sitter configurations, orbit precession for persistent coverage, and propellantless station-keeping.[1–3] These applications provide complementary benefits to the more widely studied heliocentric use cases.

In astrodynamics, mission design is a central process concerned with determining trajectories and control strategies that meet mission requirements in an efficient manner.[4] The standard workflow

*Graduate Master's Student, Department of Astrodynamics and Space Missions, Faculty of Aerospace Engineering, ffructuosovida@tudelf.nl.

begins with a global optimisation across a large design space using low-fidelity dynamical models, which allows the rapid identification of promising regions.[4,5] The most viable candidates are then refined through local optimisation with higher-fidelity models, ultimately yielding optimal or near-optimal solutions suitable for mission proposals.[4]

Both global and local optimisation typically require extensive trajectory simulations. To mitigate computational cost, low-fidelity models and relaxed numerical integration tolerances are employed during global searches. In contrast, local optimisation demands higher accuracy, and therefore higher fidelity and tighter tolerances.

While for most dynamical models trajectory propagation can only be achieved through numerical integration, there are cases where analytical or semi-analytical solutions are available and may offer compelling computational advantages with respect to classical numerical integration methods. They can reduce the per-evaluation cost of trajectory propagation and steering-law evaluation, enabling larger parameter sweeps and faster optimization loops compared to brute-force numerical propagation.[4–6]

The most notable example is the two-body problem (TBP), for which the Keplerian solution provides exact analytical propagation at a fraction of the computational expense of numerical integration.[5,7] Moreover, extensive analytical treatments exist for several perturbation models. The $J_2$ perturbation has been analysed for both single-satellite motion[8–13] and relative dynamics.[14–16] Similar analytical or semi-analytical formulations have been developed for atmospheric drag and third-body perturbations, particularly in regimes where these effects dominate.[17–21]

Analytical approaches to solar-sail dynamics have predominantly been studied in heliocentric contexts. The literature includes formulations for conic-like trajectories, linear perturbation-based solutions, and shape-based approaches, among others.[1,22–27] By contrast, planet-centred solar-sail dynamics remain largely unexplored from an analytical standpoint. One of the few early efforts is by Isayev, who analysed the motion of a planet-bound satellite subject to SRP using a formulation now referred to as the Stark model.[28] The Stark model provides an analytically tractable framework that captures first-order deviations from Keplerian motion while allowing closed- or semi-closed-form solutions.[29–32]

Historically, the Stark model has been studied mainly in the context of low-thrust propulsion.[33] More recently, Hatten et al. extended the model to include time-varying perturbations, specifically $J_2$ and atmospheric drag, and compared its performance to classical numerical integration methods.[34,35] Their findings indicate that within specific regions of the accuracy-efficiency trade space, the Stark model can outperform traditional numerical integrators.

Despite this progress, the application of the Stark model to preliminary mission design in planet-centred solar sailing remains unexamined. The objective of this work is to assess the feasibility of employing the Stark model as an alternative to numerical integration in this context. Specifically, the study evaluates the performance of the Stark model against conventional numerical methods to determine whether it offers a viable framework for preliminary mission design.

Improving the efficiency of preliminary mission design is of particular importance as solar-sailing concepts transition from theoretical studies to practical mission proposals. Analytical frameworks such as the Stark model could enable faster trade-off analyses, reduce computational demands in optimisation loops, and expand the range of feasible design studies. Establishing the viability of such methods is therefore a critical step toward enabling more rapid and robust mission design workflows for future solar-sail missions.

The remainder of this work is organised as follows. First, the dynamical model underlying the problem is formulated in detail. Next, the Stark model is introduced and derived, beginning with the equations of motion and proceeding to their solution through Hamiltonian formalism. The subsequent part of the paper presents the numerical results obtained from applying the model, together with a comparative assessment of its performance relative to conventional numerical integration methods. Finally, the study concludes with a summary of the key findings and the main contributions of the work.

## DYNAMICAL MODEL

This section provides a description of the dynamical model under consideration. The employed reference frames are introduced first. Subsequently, the acceleration model is defined and the corresponding equations of motion are presented. Finally, the derivation of the locally optimal control laws for planet-centred solar sailing are outlined.

### Reference Frames

The following reference frames are employed in this work.

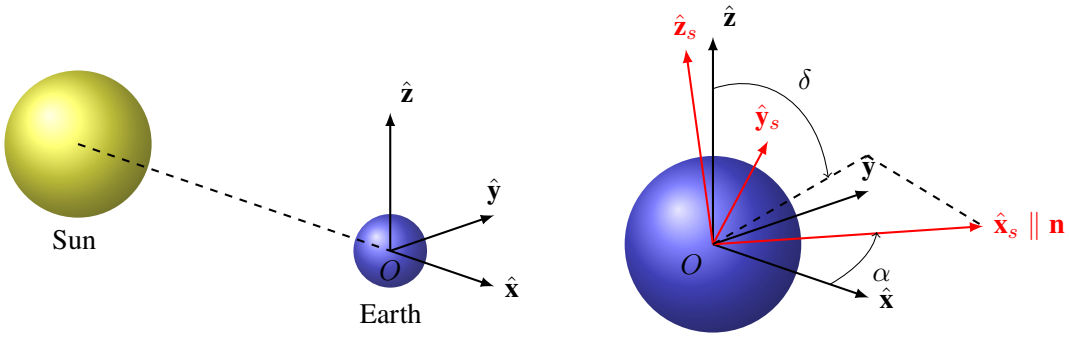


(a) ECI Reference Frame (b) SECI Reference Frame

**Figure 1**: ECI and SECI Reference Frames

*Earth Centred Inertial.* The Earth Centred Inertial (ECI) reference frame, $O_{xyz}$, is defined with its origin $O$ fixed at the centre of the Earth and three non-rotating axes $\hat{\mathbf{x}}$, $\hat{\mathbf{y}}$, and $\hat{\mathbf{z}}$ (see Fig. 1a). The $\hat{\mathbf{x}}$-axis is aligned with the Sun-Earth direction, pointing away from the Sun. The $\hat{\mathbf{y}}$-axis lies in the ecliptic plane, perpendicular to $\hat{\mathbf{x}}$, and is oriented in the prograde direction. The $\hat{\mathbf{z}}$-axis is perpendicular to both $\hat{\mathbf{x}}$ and $\hat{\mathbf{z}}$, completing the right-handed trihedron.

*Stark Earth Centred Inertial.* The Stark Earth Centred Inertial (SECI) reference frame, $O_{x_s y_s z_s}$, is an inertial frame with its origin $O$ at the centre of the Earth and three non-rotating axes $\hat{\mathbf{x}}_s$, $\hat{\mathbf{y}}_s$, and $\hat{\mathbf{z}}_s$ (see Fig. 1b). It is introduced to facilitate the transformation between the coordinates used in the Stark model and those of the ECI frame. The $\hat{\mathbf{x}}_s$-axis is aligned with the sail normal vector $\mathbf{n}$. The $\hat{\mathbf{z}}_s$-axis is the unit vector normal to the plane defined by $\hat{\mathbf{x}}$ and $\hat{\mathbf{x}}_s$, that is, $\hat{\mathbf{z}}_s = \frac{\hat{\mathbf{x}} \times \hat{\mathbf{x}}_s}{\|\hat{\mathbf{x}} \times \hat{\mathbf{x}}_s\|}$. The $\hat{\mathbf{y}}_s$-axis is orthogonal to both, completing the right-handed trihedron.

The cone, $\alpha$, and clock, $\delta$, angles of the three-dimensional solar-sail acceleration model, see below,

in the ECI frame define the transformation between the two frames as:

$$\mathbf{X}_s = R^{ECI}_{SECI}\mathbf{X} \quad \textit{where} \quad R^{ECI}_{SECI} = \begin{bmatrix} \cos\alpha & \sin\alpha\sin\delta & \sin\alpha\cos\delta \\ -\sin\alpha & \cos\alpha\sin\delta & \cos\alpha\cos\delta \\ 0 & -\cos\delta & \sin\delta \end{bmatrix} \tag{1}$$

Here, $R^{ECI}_{SECI}$ is the rotation matrix from the ECI frame to the SECI frame, corresponding to a rotation by $\delta$ about the $\hat{\mathbf{x}}$-axis followed by a rotation by $\alpha$ about the $\hat{\mathbf{z}}_s$-axis.

Angles $\alpha$ and $\delta$, as defined in Fig. 1b, differ from the true cone and clock angles of the solar-sail acceleration model, since the cone angle is measured relative to the Sun-satellite direction rather than the Sun-Earth direction. However, for near-Earth orbits, the assumption of parallel solar rays justifies this approximation.

*Radial-AlongTrack-CrossTrack.* The Radial-AlongTrack-CrossTrack (RSW) frame, $B_{RSW}$, is a body frame with its origin $B$ at the centre of mass of the solar sail and three moving axes $\hat{\mathbf{R}}$, $\hat{\mathbf{S}}$, and $\hat{\mathbf{W}}$. The $\hat{\mathbf{R}}$-axis is aligned with the radial direction, pointing away from the Earth, $\hat{\mathbf{R}} = \frac{\mathbf{r}}{r}$, where $\mathbf{r}$ is the position vector in the ECI frame. The $\hat{\mathbf{W}}$-axis is normal to the orbital plane, pointing along the orbital angular momentum vector, $\hat{\mathbf{W}} = \frac{\mathbf{r}\times\mathbf{v}}{||\mathbf{r}\times\mathbf{v}||}$, where $\mathbf{v}$ is the velocity vector in the ECI frame. Finally, the $\hat{\mathbf{S}}$-axis is orthogonal to both $\hat{\mathbf{R}}$ and $\hat{\mathbf{W}}$, completing the right-handed trihedron, $\hat{\mathbf{S}} = \hat{\mathbf{W}} \times \hat{\mathbf{R}}$.

**Acceleration Model**

The acceleration model adopted in this work corresponds to the simplest solar-sail acceleration formulation. This choice enables a direct comparison between the Stark model and numerical propagation while avoiding additional dynamical complexities. Accordingly, only Earth point-mass gravity and SRP accelerations are considered.

The SRP acceleration model is further simplified by the following assumptions: (i) the Sun-sail distance is taken as constant along the orbit and equal to the mean Sun-Earth distance, such that the acceleration magnitude depends only on the sail orientation; (ii) solar flux is modelled under the parallel rays approximation; (iii) eclipses are neglected; and (iv) the sail is assumed to possess ideal optical properties, resulting in perfect reflectivity. Under these assumptions, the SRP acceleration in a planet-centred orbit is expressed as:

$$\mathbf{a}_{SRP} = 2P\frac{A}{m}\left(\mathbf{n}\cdot\hat{\mathbf{x}}\right)^2\mathbf{n} \tag{2}$$

Here, $P$ denotes the SRP, $A$ the sail area, and $m$ the spacecraft mass. Note that the formulation in Eq. (2) differs from the classical heliocentric expression, where $(\mathbf{n}\cdot\hat{\mathbf{r}})$ is used instead of $(\mathbf{n}\cdot\hat{\mathbf{x}})$. The distinction arises because, in the heliocentric case, the direction of sunlight is radial, $\hat{\mathbf{r}}$, whereas in the planet-centred case it coincides with the $\hat{\mathbf{x}}$-axis of the ECI frame. Introducing the sail loading $\sigma = \frac{m}{A}$, together with the SRP definition $P = \frac{L_\odot}{4\pi r_E^2 c}$, where $L_\odot$ is the solar luminosity and $r_E$ the mean heliocentric distance of the Earth, and noting that $(\mathbf{n}\cdot\hat{\mathbf{x}}) = \cos\alpha$, the SRP acceleration becomes:

$$\mathbf{a}_{SRP} = \beta\frac{GM_\odot}{r_E^2}\cos^2\alpha\mathbf{n} \tag{3}$$

Here, $\beta$ denotes the sail lightness number, defined as:

$$\beta = \frac{\sigma^*}{\sigma} \quad \textit{where} \quad \sigma^* = \frac{L_\odot}{2\pi GM_\odot c} \tag{4}$$

Thus, for a given cone angle $\alpha$, the SRP acceleration has constant magnitude: $a_{SRP} = \beta \frac{GM_\odot}{r_E^2} \cos^2 \alpha$. The resulting equations of motion in the ECI frame are given by:

$$\begin{aligned} \ddot{x} &= -\mu \frac{x}{r^3} + a_{SRP} \cos \alpha \\ \ddot{y} &= -\mu \frac{y}{r^3} + a_{SRP} \sin \alpha \sin \delta \\ \ddot{z} &= -\mu \frac{z}{r^3} + a_{SRP} \sin \alpha \cos \delta \end{aligned} \tag{5}$$

Here, $\mu$ denotes the standard gravitational parameter of the Earth. Applying the rotation matrix in Eq. (1), the equations in the SECI frame are obtained as

$$\begin{aligned} \ddot{x}_s &= -\mu \frac{x_s}{r^3} + a_{SRP} \\ \ddot{y}_s &= -\mu \frac{y_s}{r^3} \\ \ddot{z}_s &= -\mu \frac{z_s}{r^3} \end{aligned} \tag{6}$$

The form in Eq. (6) corresponds to the Stark problem. In this frame, for given cone and clock angles, the SRP perturbation is constant both in magnitude and direction, which forms the basis for the integration of the model.

**Planet-Centred Solar-Sailing Locally Optimal Control Laws**

Locally optimal control laws (LOCLs) aim to maximise the instantaneous rate of change of a chosen orbital element, providing analytical expressions for the control that depend solely on the current state. Although such laws do not yield globally optimal trajectories, they avoid the need for numerical optimisation and enable simple manoeuvres, such as orbit raising. The derivations shown below concern the planet-centred solar-sailing LOCLs first derived by Macdonald and McInnes.[36]

Consider the Lagrange variational equation for the orbital element of interest, $k$, which is given by:

$$\frac{dk}{dt} = \mathbf{f} \cdot \boldsymbol{\lambda}_k \tag{7}$$

Here, $\mathbf{f}$ denotes the SRP force and $\boldsymbol{\lambda}_k$ a vector depending on the current state. Maximising the rate of change of $k$ is equivalent to maximising the projection $\mathbf{f} \cdot \boldsymbol{\lambda}_k$. To this end, $\boldsymbol{\lambda}$ can be defined as a unit vector expressed in terms of its own cone and clock angles, $\tilde{\alpha}$ and $\tilde{\delta}$:

$$\boldsymbol{\lambda} = \cos \tilde{\alpha} \hat{\mathbf{x}} + \sin \tilde{\alpha} \sin \tilde{\delta} \hat{\mathbf{y}} + \sin \tilde{\alpha} \cos \tilde{\delta} \hat{\mathbf{z}} \tag{8}$$

Note that the subindex $k$ has been dropped for simplicity. For a given state, $\tilde{\alpha}$ and $\tilde{\delta}$ are then determined as:

$$\begin{aligned} \tilde{\alpha} &= \arccos \lambda_x \\ \tilde{\delta} &= \arctan \left( \frac{\lambda_y}{\lambda_z} \right) \end{aligned} \tag{9}$$

The projection of the SRP force on $\boldsymbol{\lambda}$, obtained from Eq. (2), is given by:

$$f_\lambda = 2PA \left( \mathbf{n} \cdot \hat{\mathbf{x}} \right)^2 \mathbf{n} \cdot \boldsymbol{\lambda} \tag{10}$$

Expressed in terms of the cone and clock angles of $\mathbf{n}$ and $\boldsymbol{\lambda}$, Eq. (10) becomes:

$$f_\lambda = 2PA\cos^2\alpha\left[\cos\alpha\cos\tilde{\alpha} + \sin\alpha\sin\tilde{\alpha}\cos\left(\delta - \tilde{\delta}\right)\right] \tag{11}$$

From Eq. (11), it follows that the projection is maximised when $\delta = \tilde{\delta}$. The optimal cone angle is then obtained by solving $\frac{\partial f_\lambda}{\partial \alpha} = 0$. After algebraic simplification, the locally optimal cone and clock angles are given by:

$$\begin{aligned}\delta^* &= \tilde{\delta} \\ \alpha^* &= \arctan\left(\frac{-3\cos\tilde{\alpha} + \sqrt{9\cos^2\tilde{\alpha} + 8\sin^2\tilde{\alpha}}}{4\sin\tilde{\alpha}}\right)\end{aligned} \tag{12}$$

These analytical expressions depend only on $\tilde{\alpha}$ and $\tilde{\delta}$, which in turn are functions of the spacecraft state, $\hat{\mathbf{x}}$, at a given epoch and of the chosen orbital element $k$.

## STARK MODEL

This section addresses the bounded case of the three-dimensional Stark model according to the approach developed by Lantoine.[29,30] The equations of motion of the Stark problem are first presented, followed by the definition of the variable transformations employed in the formulation. The Hamilton-Jacobi formalism is then applied to obtain the integrals of motion, which are subsequently integrated.

### Stark Problem

The Stark problem corresponds to the particular case of the perturbed TBP in which the perturbation is constant in both magnitude and direction. The equations of motion are therefore those of the TBP, $\ddot{\mathbf{r}} = -\mu\frac{\mathbf{r}}{r^3}$, with the addition of a constant acceleration $\epsilon$ along one coordinate axis:

$$\begin{aligned}\ddot{x} &= -\mu\frac{x}{r^3} \\ \ddot{y} &= -\mu\frac{y}{r^3} \\ \ddot{z} &= -\mu\frac{z}{r^3} + \epsilon\end{aligned} \tag{13}$$

Here, the constant perturbation is introduced in the $z$-direction. However, any arbitrary direction in $\mathbb{R}^3$ can be reduced to this form through a suitable rotation. This corresponds to the equations of motion of the SRP acceleration in the SECI frame given in Eq. (6).

### Variable Changes

To integrate the equations derived from the Hamilton-Jacobi formalism, changes of variables are required for both the state and the time.

*State* The state transformation consists of converting Cartesian coordinates into three-dimensional parabolic coordinates. Taking the $z$-direction as the direction of the perturbation, as in Eq. (13), the transformation is given by:

$$\begin{aligned}x &= \xi\eta\cos\phi \\ y &= \xi\eta\sin\phi \\ z &= \frac{1}{2}\left(\xi^2 - \eta^2\right)\end{aligned} \quad \Rightarrow \quad \begin{aligned}\dot{x} &= \left(\dot{\xi}\eta + \xi\dot{\eta}\right)\cos\phi - \xi\eta\dot{\phi}\sin\phi \\ \dot{y} &= \left(\dot{\xi}\eta + \xi\dot{\eta}\right)\sin\phi + \xi\eta\dot{\phi}\cos\phi \\ \dot{z} &= \xi\dot{\xi} - \eta\dot{\eta}\end{aligned} \tag{14}$$

The inverse transformation is as:

$$\begin{aligned} \xi &= \sqrt{r+z} \\ \eta &= \sqrt{r-z} \\ \phi &= \arctan\left(\frac{x}{y}\right) \end{aligned} \quad \Rightarrow \quad \begin{aligned} \dot{\xi} &= \frac{\dot{r}+\dot{z}}{2\sqrt{r+z}} \\ \dot{\eta} &= \frac{\dot{r}-\dot{z}}{2\sqrt{r-z}} \\ \dot{\phi} &= \frac{x\dot{y}-\dot{x}y}{x^2+y^2} \end{aligned} \tag{15}$$

*Time* To motivate the time transformation, consider the velocity in parabolic coordinates:

$$v^2 = \dot{x}^2 + \dot{y}^2 + \dot{z}^2 = \left(\xi^2+\eta^2\right)\left(\dot{\xi}^2+\dot{\eta}^2\right) + \xi^2\eta^2\dot{\phi}^2 \tag{16}$$

From Eq. (16), it is evident that the contributions associated with $\xi$ and $\eta$ scale with $(\xi^2+\eta^2)$, whereas the contribution associated with $\phi$ scales with $\xi^2\eta^2$. This motivates the introduction of the following time variables:

$$d\tau_1 = \frac{1}{\xi^2+\eta^2}dt \tag{17}$$

$$d\tau_2 = \frac{1}{\xi^2\eta^2}dt \tag{18}$$

Here, $\tau_1$ and $\tau_2$ represent the radial and azimuthal fictitious times, respectively. These transformations facilitate the integration of the equations of motion, as will be demonstrated later.

**Hamilton-Jacobi Formalism**

To obtain a solution to the Stark problem, this subsection approaches the integration of the equations of motion within the framework of the Hamilton-Jacobi formalism. The objective is to construct Hamilton's principal function in a form that admits separation of variables, thereby enabling the integration of the equations of motion. Derivations and statements regarding analytical mechanics concerns follow *Analytical mechanics: an introduction* from Fasano and Marmi.[37]

The starting point is the Hamilton-Jacobi equation, which establishes the relation between Hamilton's principal function, $S$, and the Hamiltonian, $H$, of the system:

$$H\left(\mathbf{q}, \mathbf{p}=\frac{\partial S}{\partial \mathbf{q}}, t\right) + \frac{\partial S}{\partial t} = 0 \quad \text{where} \quad S = S\left(\mathbf{q}, \boldsymbol{\rho}, t\right) \tag{19}$$

Here, $\mathbf{q}$ denotes the vector of generalised coordinates, $\mathbf{p}$ the vector of associated canonical momenta, and $\boldsymbol{\rho}$ a vector of constants of motion. To solve Hamilton-Jacobi equation, it is first necessary to formulate the Hamiltonian, which is related to the Lagrangian, $L$, of the system by:

$$H = \sum p_i \dot{q}_i\left(\mathbf{p}, \mathbf{q}, t\right) - L\left(\mathbf{q}, \dot{\mathbf{q}}\left(\mathbf{p}, \mathbf{q}, t\right), t\right) \tag{20}$$

Since the Lagrangian is defined as the difference between the kinetic $\tilde{K}$ and potential $U$ energies, the first step is to express these quantities in parabolic coordinates.

$$\tilde{K} = \frac{1}{2}\left(\dot{x}^2+\dot{y}^2+\dot{z}^2\right) = \frac{1}{2}\left[\left(\xi^2+\eta^2\right)\left(\dot{\xi}^2+\dot{\eta}^2\right) + \xi^2\eta^2\dot{\phi}^2\right] \tag{21}$$

$$U = -\frac{\mu}{r} - \epsilon z = -\frac{2\mu}{\xi^2+\eta^2} - \frac{1}{2}\epsilon\left(\xi^2-\eta^2\right) \tag{22}$$

The Lagrangian then follows as:

$$L = \tilde{K} - U = \frac{1}{2}\left[\left(\xi^2+\eta^2\right)\left(\dot{\xi}^2+\dot{\eta}^2\right)+\xi^2\eta^2\dot{\phi}^2\right] + \frac{2\mu}{\xi^2+\eta^2} + \frac{1}{2}\epsilon\left(\xi^2-\eta^2\right) \tag{23}$$

From Eq. (23), the canonical momenta are obtained as:

$$\begin{aligned} p_\xi &= \frac{\partial L}{\partial \xi} = \left(\xi^2+\eta^2\right)\dot{\xi} \\ p_\eta &= \frac{\partial L}{\partial \eta} = \left(\xi^2+\eta^2\right)\dot{\eta} \\ p_\phi &= \frac{\partial L}{\partial \phi} = \xi^2\eta^2\dot{\phi} \end{aligned} \tag{24}$$

The time transformation introduced earlier is implicitly recovered in these expressions. Substituting Eqs. (23) and (24) into Eq. (20) yields the expression for the Hamiltonian in terms of the generalised coordinates and their canonical momenta.

$$H = \frac{1}{2}\frac{p_\xi^2+p_\eta^2}{\xi^2+\eta^2} + \frac{1}{2}\frac{p_\phi^2}{\xi^2\eta^2} - \frac{2\mu}{\xi^2+\eta^2} - \frac{1}{2}\epsilon\left(\xi^2-\eta^2\right) \tag{25}$$

With the Hamiltonian in Eq. (25), the Hamilton-Jacobi equation can be solved by applying the separation of variables technique to determine Hamilton's principal function.

*Separation of variables on $t$* Since the Hamiltonian does not explicitly depend on time, the variable $t$ can be separated into an independent contribution $S'\left(t,\boldsymbol{\rho}\right)$. This immediately implies that the Hamiltonian is conserved, $H =$ constant. From Eq. (19), the time-dependent part of Hamilton's principal function follows as:

$$S'\left(t,\boldsymbol{\rho}\right) = -H\left(t-t_0\right) \tag{26}$$

Here, $t_0$ corresponds to the initial condition of the time variable.

*Separation of variables on $\phi$* Analogous to the time variable, the Hamiltonian does not explicitly depend on $\phi$. This allows for the separation of the $\phi$-dependent part of Hamilton's main function as $W_\phi(\phi)$. Since $\phi$ is thus a cyclic coordinate, its conjugate momentum $p_\phi$ is conserved, $p_\phi = constant$. Recalling that $p_\phi = \frac{\partial S}{\partial \phi}$, the corresponding contribution to the principal function is

$$W_\phi\left(\phi,\boldsymbol{\rho}\right) = p_\phi\left(\phi-\phi_0\right) \tag{27}$$

Here, $\phi_0$ corresponds to the initial condition of $\phi$.

*Separation of variables on $\xi$ and $\eta$* After the separation in $t$ and $\phi$, the principal function can be expressed as $S = S'\left(t,\boldsymbol{\rho}\right) + W_\phi\left(\phi,\boldsymbol{\rho}\right) + W'\left(\xi,\eta,\boldsymbol{\rho}\right)$. Using the definitions of the canonical momenta, $\mathbf{p} = \frac{\partial S}{\partial \mathbf{q}}$, the Hamilton-Jacobi equation can be expanded. After algebraic manipulation, it becomes

$$\frac{1}{2}\frac{1}{\xi^2+\eta^2}\left[\left(\frac{\partial W'}{\partial \xi}\right)^2+\left(\frac{\partial W'}{\partial \eta}\right)^2\right] + \frac{1}{2}\frac{1}{\xi^2\eta^2}p_\phi^2 - \frac{2\mu}{\xi^2+\eta^2} - \frac{1}{2}\epsilon\left(\xi^2-\eta^2\right) - H = 0 \tag{28}$$

Multiplying both sides by $2(\xi^2+\eta^2)$ yields:

$$\left(\frac{\partial W'}{\partial \xi}\right)^2 + \frac{p_\phi^2}{\xi^2} - 2\mu - \epsilon\xi^4 - 2H\xi^2 = -\left(\frac{\partial W'}{\partial \eta}\right)^2 - \frac{p_\phi^2}{\eta^2} + 2\mu - \epsilon\eta^4 + 2H\eta^2 = \kappa \tag{29}$$

Equation (29) shows that the left-hand side depends only on $\xi$, while the right-hand side depends only on $\eta$. The only consistent solution is that both sides are equal and constant, allowing to identify a constant of motion, $\kappa$. Therefore, separation of variables can be applied to $W'(\xi, \eta, \boldsymbol{\rho})$. Each contribution can then be integrated independently:

$$W_\xi(\xi, \boldsymbol{\rho}) = \int_{\xi_0}^{\xi} \bar{\delta}_\xi \sqrt{\epsilon\xi^4 + 2H\xi^2 + (2\mu + \kappa) - \frac{p_\phi^2}{\xi^2}} d\xi \tag{30}$$

$$W_\eta(\eta, \boldsymbol{\rho}) = \int_{\eta_0}^{\eta} \bar{\delta}_\eta \sqrt{-\epsilon\eta^4 + 2H\eta^2 + (2\mu - \kappa) - \frac{p_\phi^2}{\eta^2}} d\eta \tag{31}$$

Here, $\bar{\delta}_\xi$ and $\bar{\delta}_\eta$ denote the undetermined sign of the square root. These signs must be determined at a later stage, based on the initial conditions of the trajectory. Since the subsequent derivations of the equations of motion require differentiating the expressions in Eqs. (30) and (31), it is sufficient to retain these expressions in their integral form at this stage.

*Hamilton's Principal Function* The complete expression for Hamilton's principal function is given by a combination of functions, each depending solely on one variable.

$$S(\mathbf{q}, \boldsymbol{\rho}, t) = S'(t, \boldsymbol{\rho}) + W_\xi(\xi, \boldsymbol{\rho}) + W_\eta(\eta, \boldsymbol{\rho}) + W_\phi(\phi, \boldsymbol{\rho}) \tag{32}$$

Furthermore, the vector of constants of motion $\boldsymbol{\rho}$ remains defined.

$$\boldsymbol{\rho} = [H, p_\phi, \kappa] \tag{33}$$

**Integration**

To integrate the equations of motion, the expressions for the canonical momenta given in Eq. (24) are combined with their definition in terms of Hamilton's principal function:

$$\mathbf{p} = \frac{\partial L}{\partial \mathbf{q}} = \frac{\partial S}{\partial \mathbf{q}} \tag{34}$$

This relation provides a direct connection between the separated contributions of $S$ and the evolution of the parabolic coordinates. Consequently, three equations of motion are obtained, one for each of the variables $\xi$, $\eta$, and $\phi$.

*Integration of $\phi$* For the case of $\phi$, the equation of motion in terms of the physical time $t$ is given by:

$$\xi^2\eta^2 \frac{d\phi}{dt} = p_\phi \tag{35}$$

To facilitate the integration, the fictitious time variable $\tau_2$ is introduced by applying the transformation in Eq. (18).

$$\frac{d\phi}{d\tau_2} = p_\phi \tag{36}$$

Since $p_\phi$ is a constant of motion, integration of Eq. (36) is given by:

$$\phi = \phi_0 + p_\phi \tau_2 \tag{37}$$

*Integration of $\xi$ and $\eta$* For the case of $\xi$ and $\eta$ the equations of motion attain a more complex form:

$$\left(\xi^2+\eta^2\right)\frac{d\xi}{dt}=\bar{\delta}_\xi\sqrt{\epsilon\xi^4+2H\xi^2+(2\mu+k)-\frac{p_\phi^2}{\xi^2}} \tag{38}$$

$$\left(\xi^2+\eta^2\right)\frac{d\eta}{dt}=\bar{\delta}_\eta\sqrt{-\epsilon\eta^4+2H\eta^2+(2\mu-k)-\frac{p_\phi^2}{\eta^2}} \tag{39}$$

As for the variable $\phi$, with the use of the transformation in Eq. (17), Eqs. (38) and (39) can be simplified as:

$$d\tau_1=\bar{\delta}_\xi\frac{\xi d\xi}{\sqrt{\epsilon\xi^6+2H\xi^4+(2\mu+k)\,\xi^2-p_\phi^2}} \tag{40}$$

$$d\tau_1=\bar{\delta}_\eta\frac{\eta d\eta}{\sqrt{-\epsilon\eta^6+2H\eta^4+(2\mu-k)\,\eta^2-p_\phi^2}} \tag{41}$$

Since these integrals share the same mathematical structure, it is convenient to instead consider a generic form of the equation:

$$d\tau_1=\bar{\delta}\frac{XdX}{\sqrt{P_1(X)}}\quad \textit{where}\quad P_1(X)=a_1X^6+a_2X^4+a_3X^2+a_4 \tag{42}$$

Since $P_1(X)$ is an even polynomial, its order can be reduced by introducing the transformation:

$$X^2=Y\quad\Rightarrow\quad 2XdX=dY \tag{43}$$

Substituting Eq. (43) into Eq. (42) yields the following:

$$d\tau_1=\bar{\delta}\frac{dY}{2\sqrt{P_1(Y)}}\quad \textit{where}\quad P_1(Y)=a_1Y^3+a_2Y^2+a_3Y+a_4 \tag{44}$$

Depending on the coefficients of the polynomial, different cases arise in the Stark model. In this work, only the bounded case is considered, for which the discriminant of the cubic equation is given by:

$$D=R^2+Q^3<0\quad\text{where}\quad R=-\frac{2a_2^3-9a_1a_2a_3+27a_1a_4^2}{54a_1^3}\quad\&\quad Q=\frac{3a_1a_3-a_2^2}{9a_1^2} \tag{45}$$

Solving the cubic equation yields the three roots of $P_1(Y)$ for the bounded case, all of which are real.

$$\begin{aligned}
Y_1&=-\frac{a_2}{3a_1}+2\sqrt{-Q}\cos\left(\frac{\bar{\theta}}{3}\right)\\
Y_2&=-\frac{a_2}{3a_1}-\sqrt{-Q}\cos\left(\frac{\bar{\theta}}{3}\right)-\sqrt{3}\sqrt{-Q}\sin\left(\frac{\bar{\theta}}{3}\right)\\
Y_2&=-\frac{a_2}{3a_1}-\sqrt{-Q}\cos\left(\frac{\bar{\theta}}{3}\right)+\sqrt{3}\sqrt{-Q}\sin\left(\frac{\bar{\theta}}{3}\right)
\end{aligned} \tag{46}$$

Here, $\bar{\theta} = \arctan\left(\frac{\sqrt{-D}}{R}\right)$. Consequently, the cubic polynomial $P_1(Y)$ can be factorised as:

$$P_1(Y) = a_1(Y - Y_1)(Y - Y_2)(Y - Y_3) \tag{47}$$

From Eq. (46), it follows that $Y_1 > Y_3 > Y_2$. For the integral to be feasible, it is required that $P_1(Y) > 0$. Depending on the sign of $a_1$, this condition defines different intervals corresponding to the bounded solution.

$$\begin{aligned} \xi: \quad a_1 > 0 \quad &\Rightarrow \quad Y_{1,\xi} > Y_{3,\xi} > Y_\xi > Y_{2,\xi} \\ \eta: \quad a_1 < 0 \quad &\Rightarrow \quad Y_{1,\eta} > Y_\eta > Y_{3,\eta} > Y_{2,\eta} \end{aligned} \tag{48}$$

Introducing the change of variable:

$$Y - Y^* = sign(a_1) Z^2 \quad \Rightarrow \quad dY = sign(a_1) 2Z dZ \tag{49}$$

Here, $Y^*$ has to be chosen such that $a_1(Y - Y^*) > 0$. Therefore, the change of variable for $\xi$ and $\eta$ is given by:

$$\begin{aligned} \xi: \quad a_1 > 0 \quad &\Rightarrow \quad Z_\xi^2 = +(Y_\xi - Y_\xi^*) \quad \textit{where} \quad Y_\xi^* = Y_{2,\xi} \\ \eta: \quad a_1 < 0 \quad &\Rightarrow \quad Z_\eta^2 = -(Y_\eta - Y_\eta^*) \quad \textit{where} \quad Y_\eta^* = Y_{1,\eta} \end{aligned} \tag{50}$$

Defining $P_1(Y) = a_1(Y - Y^*) P_2(Y)$, the transformation in Eq. (49) allows to rewrite the integral in Eq. (44) as:

$$d\tau_1 = \bar{\delta} \frac{sign(a_1) dZ}{\sqrt{|a_1|}\sqrt{P_2(Z)}} \tag{51}$$

Furthermore, applying the changes of variable in Eqs. (43) and (49), the solution for $X$ is given by:

$$X = \sqrt{Y^* + sign(a_1) Z^2} \tag{52}$$

To integrate Eq. (51), the polynomial $P_2(Z)$ must be manipulated such that the resulting integral takes the form of an elliptic integral of the first kind, $F$. Furthermore, $F$ is equivalent to the inverse Jacobi elliptic sine, arcsn. The relation between these functions is given by:[38,39]

$$F[u, K] = \int_0^u \frac{d\bar{\omega}}{\sqrt{(1 - \bar{\omega}^2)(1 - K^2\bar{\omega}^2)}} = \text{arcsn}[u, K] \quad \textit{where} \quad \begin{cases} -1 \leq u \leq 1 \\ 0 \leq K \leq 1 \end{cases} \tag{53}$$

Through algebraic manipulation of the equations of motion for both $\xi$ and $\eta$, the final form of the integrated solution for $Z$ can be obtained as:

$$Z_\xi = Z_{3,\xi} \text{sn}[u_\xi, K_\xi] \quad \textit{where} \quad u_\xi = \sqrt{\epsilon} Z_{1,\xi} \left(\bar{\delta}_\xi \tau_1 - \tau_{1,0,\xi}\right) \quad \& \quad K_\xi = \frac{Z_{3,\xi}}{Z_{1,\xi}} \tag{54}$$

$$Z_\eta = Z_{3,\eta} \text{sn}[u_\eta, K_\eta] \quad \textit{where} \quad u_\eta = -\sqrt{\epsilon} Z_{2,\eta} \left(\bar{\delta}_\eta \tau_1 - \tau_{1,0,\eta}\right) \quad \& \quad K_\eta = \frac{Z_{3,\eta}}{Z_{2,\eta}} \tag{55}$$

Note that $|a_1|$ has already been substituted by $\epsilon$, which is the perturbation parameter in the Stark problem. The values of $\tau_{1,0}$ are determined from evaluating the integral at the initial conditions. The $\bar{\delta}$ parameters are determined by differentiating the final solutions for $\xi$ and $\eta$ with respect to time at

$t = 0$ and solving for the corresponding sign. With these considerations, the resulting expressions are given by:

$$\tau_{1,0,\xi} = -\frac{1}{\sqrt{\epsilon} Z_{1,\xi}} F\left[\frac{Z_{\xi,0}}{Z_{3,\xi}}, K_\xi\right] \tag{56}$$

$$\tau_{1,0,\eta} = \frac{1}{\sqrt{\epsilon} Z_{2,\eta}} F\left[\frac{Z_{\eta,0}}{Z_{3,\eta}}, K_\eta\right] \tag{57}$$

$$\bar{\delta}_\xi = sign\left(\dot{\xi}_0 \text{sn}\left[u_{\xi,0}, K_\xi\right] \text{cn}\left[u_{\xi,0}, K_\xi\right]\right) \quad \textit{where} \quad u_{\xi,0} = -\sqrt{\epsilon} Z_{1,\xi} \tau_{1,0,\xi} \tag{58}$$

$$\bar{\delta}_\eta = sign\left(\dot{\eta}_0 \text{sn}\left[u_{\eta,0}, K_\eta\right] \text{cn}\left[u_{\eta,0}, K_\eta\right]\right) \quad \textit{where} \quad u_{\eta,0} = \sqrt{\epsilon} Z_{2,\eta} \tau_{1,0,\eta} \tag{59}$$

Here, sn and cn are the Jacobi elliptic sine and cosine, respectively. The final expressions for the evolution of $\xi$ and $\eta$ is with respect to $\tau_1$ is given by:

$$\xi = \sqrt{Y_\xi^* + Z_\xi^2} \tag{60}$$

$$\eta = \sqrt{Y_\eta^* - Z_\eta^2} \tag{61}$$

*Integration of* $\tau_2$ Although the equations of motion have already been integrated, the relation between the two fictitious time variables, $\tau_1$ and $\tau_2$, has not yet been established. Without this relation, a consistent integration with two different independent variables is not possible. To resolve this issue, the connection between $\tau_1$ and $\tau_2$ must be derived. From Eqs. (17) and (18), one obtains a differential relation between $\tau_1$ and $\tau_2$ as:

$$d\tau_2 = \left(\frac{1}{\xi^2} + \frac{1}{\eta^2}\right) d\tau_1 \tag{62}$$

Since $\xi$ and $\eta$ appear in separate terms, each contribution can be integrated independently. Substituting their integrated expressions into Eq. (62) leads to:

$$d\tau_2 = \frac{1}{Y_\xi^* + Z_{3,\xi}^2 \text{sn}^2\left[u_\xi, K_\xi\right]} d\tau_1 + \frac{1}{Y_\eta^* + Z_{3,\eta}^2 \text{sn}^2\left[u_\eta, K_\xi\right]} d\tau_1 \tag{63}$$

The integrals in Eq. (63) can be manipulated into the form of an elliptic integral of the third kind, $\Pi$, defined as:[40]

$$\Pi\left[n, u, K\right] = \int_0^u \frac{d\bar{\omega}}{1 - n\text{sn}^2\left[\bar{\omega}, K\right]} \quad \textit{where} \quad 0 \leq K \leq 1 \quad \& \quad n \neq 1 \tag{64}$$

After algebraic manipulation of Eq. (62), the integrated expression for $\tau_2$ becomes:

$$\tau_2 = \frac{\Pi\left[-\frac{Z_{3,\xi}^2}{Y_\xi^*}, u_\xi, K_\xi\right] - \Pi\left[-\frac{Z_{3,\xi}^2}{Y_\xi^*}, u_{\xi,0}, K_\xi\right]}{Y_\xi^* \sqrt{\epsilon} Z_{1,\xi} \bar{\delta}_\xi} - \frac{\Pi\left[\frac{Z_{3,\eta}^2}{Y_\eta^*}, u_\eta, K_\eta\right] - \Pi\left[\frac{Z_{3,\eta}^2}{Y_\eta^*}, u_{\eta,0}, K_\eta\right]}{Y_\eta^* \sqrt{\epsilon} Z_{2,\eta} \bar{\delta}_\eta} \tag{65}$$

*Integration of* $\tau_1$ Having expressed $\tau_2$ as a function of $\tau_1$, it is now possible to use $\tau_1$ as the independent variable and propagate the equations of motion accordingly. However, the relation between the physical time $t$ and the fictitious time $\tau_1$ remains to be established. To obtain this relation,

Eq. (17) must be employed. In this case, the integration can only be carried out after inverting the equation. Substituting the integrated expressions of $\xi$ and $\eta$ then yields the following form.

$$dt = \left(Y_\xi^* + Z_{3,\xi}^2 \mathrm{sn}^2\left[u_\xi, K_\xi\right]\right) d\tau_1 + \left(Y_\eta^* + Z_{3,\eta}^2 \mathrm{sn}^2\left[u_\eta, K_\eta\right]\right) d\tau_1 \tag{66}$$

To integrate Eq. (66), the integral of the squared Jacobian elliptic cosine is required, which is given by:[40]

$$\int_0^u \mathrm{sn}^2\left[\bar{\omega}, K\right] d\bar{\omega} = \frac{1}{K^2}\left(u - E\left[u, K\right]\right) \tag{67}$$

Here, $E$ represents the incomplete elliptic integral of the second kind. Applying Eq. (67), the integral in Eq. (66) can be solved as:

$$\begin{aligned} t = {} & \left(Y_\xi^* + Y_\eta^*\right)\tau_1 + \frac{Z_{3,\xi}^2}{\sqrt{\epsilon} Z_{1,\xi} \bar{\delta}_\xi K_\xi^2}\left(u_\xi - u_{\xi,0} - E\left[u_\xi, K_\xi\right] + E\left[u_{\xi,0}, K_\xi\right]\right) \\ & + \frac{Z_{3,\eta}^2}{\sqrt{\epsilon} Z_{2,\eta} \bar{\delta}_\eta K_\eta^2}\left(u_\eta - u_{\eta,0} - E\left[u_\eta, K_\eta\right] + E\left[u_{\eta,0}, K_\eta\right]\right) \end{aligned} \tag{68}$$

Equation (68) is referred to as the *Stark equation*. This equation provides an implicit relation between the fictitious time $\tau_1$ and the physical time $t$. The Stark equation serves as the analogue of the Kepler equation in the classical Kepler problem, with the key distinction that it involves the evaluation of elliptic integrals rather than simple transcendental functions. Consequently, its computational cost is higher than that of the Kepler equation.

## RESULTS

This section presents and analyses the results with the aim of comparing the performance of the Stark model against classical numerical integration in the context of planet-centred solar sailing. First, the simulation setup is described. Next, the performance of the Stark model under constant-control scenarios is evaluated. Finally, the analysis is extended to time-varying control laws.

### Simulation Setup

This subsection describes the simulation parameters and the adopted numerical integration methodology.

The parameters employed in the simulations are grouped into three categories: (i) reference constants, (ii) initial conditions of the reference orbit, and (iii) sets of values used in the parametric analyses.

Table 1 lists the standard gravitational parameters of the Sun, $\mu_\odot$, and Earth, $\mu_E$, together with the lightness number of the Advanced Composite Solar Sail System (ACS3) sail.[41,42] The initial conditions of the reference orbit, expressed in both Cartesian coordinates and Keplerian elements within the ECI frame, are shown in Table 2. For the parametric analyses, different ranges of sail and orbital parameters were explored. Table 3 summarizes the intervals, number of elements, and distributions adopted for the sail-related variables. Similarly, Table 4 details the corresponding values for the orbital parameters. The benchmark numerical integration was determined by performing numerical integrations at different tolerances. The solution obtained at a given tolerance was compared against that computed with a tolerance one order of magnitude smaller, thereby providing an estimate of the integration error at the larger tolerance. This approach enables the identification of

**Table 1**: Reference values: solar standard gravitational parameter $\mu_\odot$, Earth's standard gravitational parameter $\mu_E$, and solar-sail lightness number $\beta$.

| $\mu_\odot$ [m$^3$/s$^2$] | $\mu_E$ [m$^3$/s$^2$] | $\beta_{ACS3}$ [-] |
|---|---|---|
| 1.327e+20 | 3.986e+14 | 0.0077 |

**Table 2**: Initial conditions of the reference orbit in the ECI frame, given in Cartesian and Keplerian form. The data is derived from a two-line element set (TLE) with epoch 6 July 2025, 22:10:15.44 UTC.[43]

| $x$ [km] | $y$ [km] | $z$ [km] | $v_x$ [km/s] | $v_y$ [km/s] | $v_z$ [km/s] |
|---|---|---|---|---|---|
| -2.132e+03 | -7.006e+03 | -8.606e+01 | -3.635 | 1.080 | 6.341 |
| $a$ [km] | $e$ [-] | $i$ [deg] | $\Omega$ [deg] | $\omega$ [deg] | $\theta$ [deg] |
| 7.346e+03 | 7.414e-03 | 120.9 | 252.7 | 65.52 | 293.7 |

**Table 3**: Sail parameters employed in the parametric analyses: intervals, number of elements, and distributions.

| **Parameter** | $\beta$ [$\beta_{ACS3}$] | $\alpha$ [deg] |
|---|---|---|
| **Interval** | $[10^{-1}, 10^{1}]$ | $[0, 89]$ |
| **Elements** | 21 | 90 |
| **Distribution** | Logarithmic | Linear |

**Table 4**: Orbital parameters employed in the parametric analyses: intervals, number of elements, and distributions.

| **Parameter** | $a$ [km] | $e$ [-] | $i$ [deg] | $\Omega$ [deg] | $\omega$ [deg] | $\theta$ [deg] |
|---|---|---|---|---|---|---|
| **Interval** | $[6971, 100000]$ | $[10^{-3}, 0.9]$ | $[1, 179]$ | $[1, 359]$ | $[0, 360]$ | $[0, 360]$ |
| **Elements** | 100 | 100 | 100 | 100 | 100 | 100 |
| **Distribution** | Linear | Linear | Linear | Linear | Linear | Linear |

the tolerance value for which the truncation error, introduced by the integration scheme, equals the round-off error caused by floating point arithmetic limitations.[44]

The scheme selected for the numerical integration is the Runge-Kutta 45 (RK45), due to its robustness and efficiency, stemming from its step-size adaptability, which makes it particularly suitable for trajectory propagation problems.[45] Based on the benchmarking methodology, the tolerance adopted for the reference integrations is of $tol = 10^{-14}$.

All trajectories were propagated for one day. The performance of the Stark model is evaluated in terms of computational efficiency and maximum position error with respect to the benchmark numerical integration. The maximum position error is selected as the accuracy metric due to the noisy nature of the model solution, as will be shown later. Although velocity errors were also computed, they are not reported here, as they exhibit trends similar to those observed in the position errors.

$$\Delta r_{max} = \max\left(||\mathbf{r}_{t,A} - \mathbf{r}_{t,N}||\right) \tag{69}$$

Equation (69) defines the maximum position error, $\Delta r_{max}$, as the maximum norm of the difference between the analytical trajectory position vector, $\mathbf{r}_{t,A}$, and the numerical trajectory position vector, $\mathbf{r}_{t,N}$.

**Constant Control Law**

The Stark model integrates the equations of motion under the assumption that the perturbation has constant magnitude and direction. These conditions are satisfied under a constant control law, enabling the model to propagate the trajectory over an indefinite time interval in a single step. Consequently, the computational cost of the Stark model is inherently lower than that of numerical integration, which requires intermediate steps to reach the final propagation time. Therefore, the analysis focuses on the maximum position error relative to the numerical benchmark, while reporting the average computational time required for a single-step propagation with the Stark model.

Since the governing equations are expressed in terms of the fictitious time $\tau_1$, two possible independent variables can be used for the integration: the physical time $t$ and the fictitious time $\tau_1$. When integrating with $t$, the Stark equation (Eq. (68)) must be solved iteratively to obtain the fictitious times corresponding to the desired physical times. Conversely, integration with $\tau_1$ allows for direct evaluation at specified values of the fictitious time. However, in this case, the Stark equation is still required to recover the corresponding physical times at which the benchmark solution must be evaluated.

The results of the parametric analysis with $t$ as the independent variable are presented in Fig. 2. The figure shows the position error relative to the benchmark (Fig. 2a) and the average computational time per evaluation (Fig. 2b) for different combinations of the sail cone angle $\alpha$ and lightness number $\beta$. For the ranges of sail cone angle and lightness number considered, position errors range between $\Delta r_{max} \in \left[10^{-3}, 10^{3}\right]$ m while the computational time per evaluation ranges between CPU Time $\in [1, 3] \times 10^{-4}$ s.

The results indicate that both the position error and the computational time per evaluation increase for larger $\alpha$ and smaller $\beta$. This behaviour reflects the dependence of accuracy and computational effort on the perturbation magnitude $\epsilon = ||\mathbf{a}_{SRP}||$: both metrics worsen as $\epsilon$ decreases. The reciprocal of the perturbation magnitude, $\epsilon^{-1}$, for each pair $(\alpha, \beta)$ is plotted in Fig. 3. The contour patterns match those observed in Fig. 2, further confirming the correlation between error growth, computational time, and decreasing perturbation magnitude. This result appears counter-intuitive, since larger values of the perturbation magnitude increase the influence of the perturbation on the dynamics for time-varying perturbations, thus reducing the controllability and increasing the stiffness of the system. However, for a constant perturbation, controllability and stiffness remain unaffected, with the perturbation simply shifting the dynamics. The observed relation between the perturbation magnitude and the performance of the Stark model arises from numerical noise introduced in the evaluation of intermediate functions, as discussed in detail below.

When integrating with $\tau_1$ as the independent variable, the parametric results are shown in Fig. 4. As before, the position error increases for larger $\alpha$ and smaller $\beta$. However, in contrast to the $t$-based case, the computational time per evaluation shows no direct dependence on either parameter. These results indicate that the position error is still inversely correlated with $\epsilon$, but computational time is unaffected by sail parameters when $\tau_1$ is used as the independent variable.

A comparison of Figs. 2a and 4a reveals that the choice of independent variable has negligible impact on the maximum position error. This suggests that errors introduced during the inversion of the Stark equation are not the dominant source of inaccuracy. In contrast, Figs. 2b and 4b show that the inversion substantially increases computational cost, by up to two orders of magnitude. This effect is more pronounced for small $\epsilon$, where the root-finding algorithm requires more iterations to compute the corresponding fictitious time. Since the differences associated with the choice of inde-

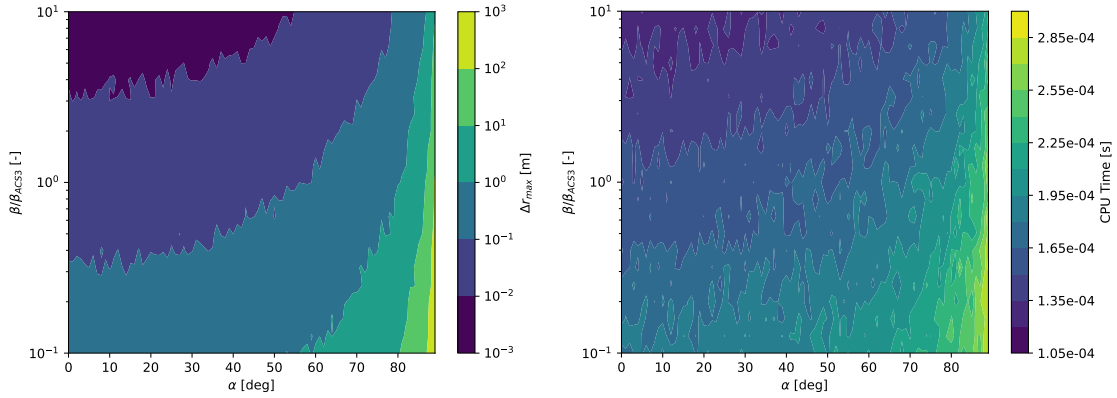


(a) (b)

**Figure 2**: Position error (a) with respect to the numerical benchmark and computational time per evaluation (b) of the Stark model for different combinations of cone angle $\alpha$ and lightness number $\beta$, integrating with the physical time $t$ as the independent variable.

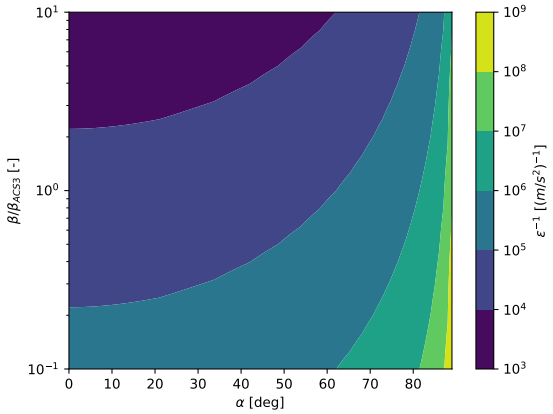


**Figure 3**: Reciprocal perturbation magnitude $\epsilon^{-1}$ for different combinations of cone angle $\alpha$ and lightness number $\beta$.

pendent variable have been established, subsequent analyses will adopt the same integration strategy. Although using the fictitious time $\tau_1$ has shown greater computational efficiency, its relation to the physical time $t$ is both non-linear and dependent on the initial conditions and perturbation magnitude. Consequently, the correspondence between discretisation in $\tau_1$ and $t$ cannot be determined *a priori*. For consistency, all subsequent analyses are therefore performed using the physical time $t$ as the independent variable.

The observed inverse correlation between position error and perturbation magnitude suggests that the dominant error source is numerical noise introduced by intermediate operations, such as the evaluation of elliptic integrals. This noise is amplified by a negative power of $\epsilon$. To illustrate this issue, Fig. 5 shows the error in the calculation of the elliptic integral of the first kind $F$ (Fig. 5a), used in computing the initial fictitious times $\tau_{1,0}$ in Eqs. (56) and (57), with respect to Wolfram Mathematica 14.2,[46] and the corresponding error in the physical time $t$ recovered in the Stark model

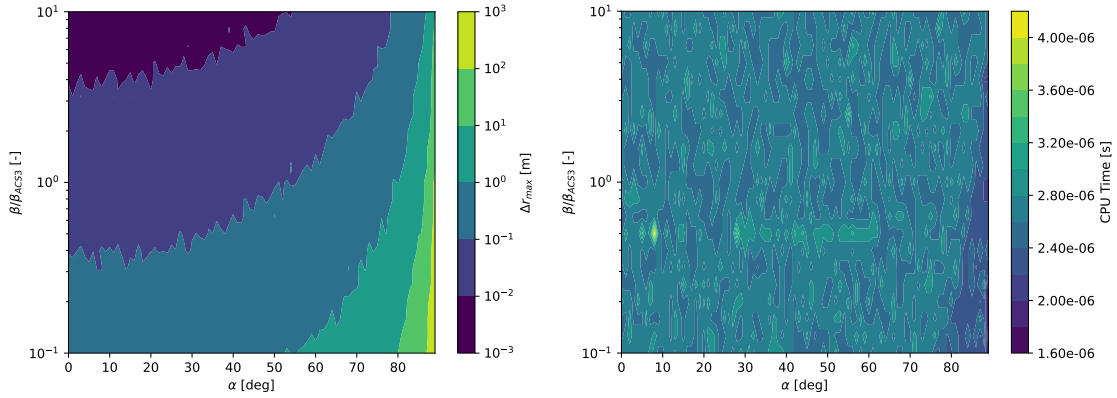


(a) Position Error (b) Computational Time

**Figure 4**: Position error (a) with respect to the numerical benchmark and computational time (b) of the Stark model for different combinations of cone angle, $\alpha$, and lightness number, $\beta$, integrating with the fictitious time $\tau_1$ as the independent variable.

integration (Fig. 5b). The results, obtained for $\beta = \beta_{ACS3}$, $\alpha = 0°$, and the initial orbit in Table 2, show that the noise in the evaluation of intermediate functions, in this case the elliptic integral of the first kind, grows with physical time. Since this noise is then multiplied by a negative power of $\epsilon$ (see Eqs. (56) and (57)), it propagates into the evaluation of the Stark equation (Eq. (68)), ultimately leading to a mismatch between the target and actual physical times at which the solution is obtained. This time discrepancy propagates into position errors, as shown in Fig. 6. The figure

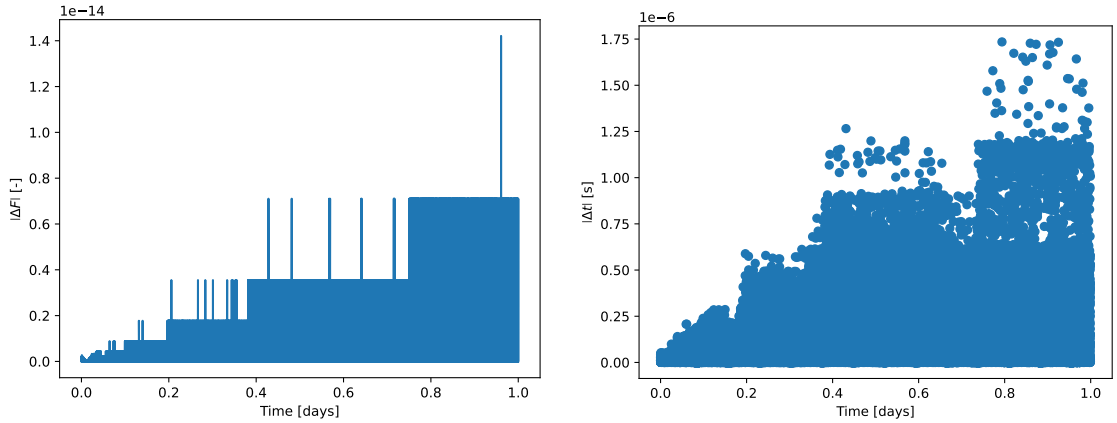


(a) (b)

**Figure 5**: (a) Error in the calculation of the elliptic function of the first kind $F$ relative to Wolfram Mathematica 14.2,[46] $\Delta F$, and (b) error in the the physical time $t$, $\Delta t$, in the Stark model integration for $\beta = \beta_{ACS3}$, $\alpha = 0°$, and the reference initial conditions.

compares the position error relative to the benchmark for both the analytical integration (blue) and the numerical integration (orange), which corresponds to the numerical benchmark evaluated at the physical times derived from the inversion of the Stark equation. The results show that the time

discrepancy is also translated into a position error in the numerical integration, which increases with physical time. While the error magnitudes differ between the two approaches, their evolution exhibits the same trend, confirming that the dominant error source is the numerical evaluation of intermediate functions.

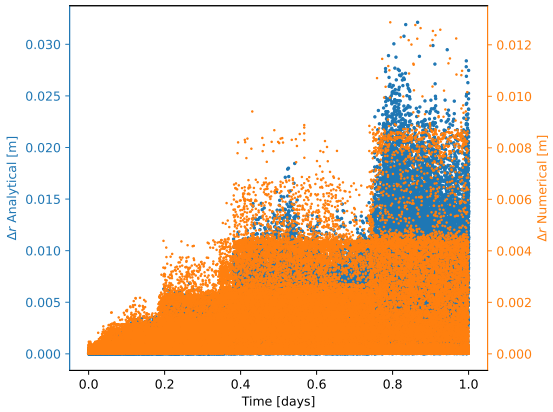


**Figure 6**: Position error relative to the benchmark propagation for analytical (blue) and numerical (orange) integrations, both evaluated at the physical time obtained via inversion of the Stark equation.

The influence of the initial orbital elements on model performance is examined in Fig. 7, where $t$ is used as the independent variable. The figure shows the position error (blue) and computational time per evaluation (orange) as each Keplerian element is varied independently across the ranges specified in Table 4. The results show negligible sensitivity to $i$, $\Omega$, $\omega$, and $\theta$. By contrast, the position error and computational cost both decrease with increasing semi-major axis $a$, and increase with increasing eccentricity $e$. This behavior arises because smaller $a$ and larger $e$ correspond to faster orbital dynamics, so the same time mismatch translates into larger spatial errors. Since the reference orbit is nearly circular (Table 2), the apparent independence of accuracy and computational cost on $\omega$ may not be representative. To verify the independence of the Stark model performance from the argument of periapsis of the initial orbit, simulations were repeated with the same reference orbit but eccentricity set to $e = 0.5$. The results confirmed that accuracy and computational cost remain unaffected by $\omega$, even for non-circular orbits.

### Time-Varying Control Law

For constant control laws, the Stark model permits integration up to any desired time instant in a single step. This property no longer holds for time-varying control laws, as both the magnitude and direction of the SRP acceleration change throughout the trajectory. Consequently, the integration must follow a numerical-like approach: the control law is approximated as piecewise constant, discretising the trajectory into intervals where the control is assumed constant. For each interval, the model is reinitialised and the trajectory propagated over the corresponding time span.

This subsection analyses the performance of the Stark model under time-varying control laws, using numerical integration as a benchmark. The laws considered correspond to planet-centred solar-sailing LOCLs discussed on page 5. The analysis is divided into two parts. First, since the present implementation of the Stark model does not support step-size adaptability, its performance is evaluated for different fixed step sizes and compared against numerical integrations conducted with

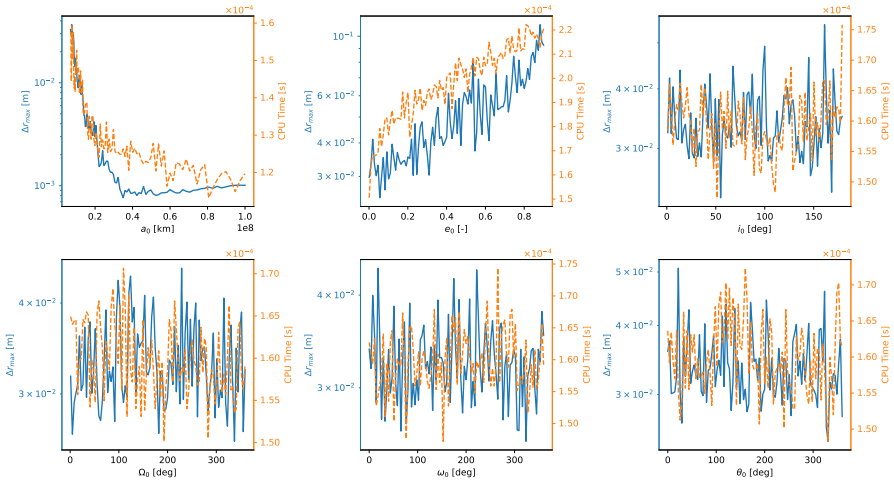


**Figure 7**: Position error (blue) and computational time per evaluation (orange) as a function of the initial Keplerian elements, varied one at a time across the ranges in Table 4, with the remaining elements set to the reference orbit in Table 1.

varying tolerances. Second, the control laws are studied using the variable-step-size discretisation provided by the numerical integrations under the considered tolerances.

*Fixed Step Size* The performance of the Stark model with fixed step sizes is evaluated by comparing its accuracy and computational cost against numerically integrated simulations. In the analytical case, different step sizes are considered, while in the numerical case different integration tolerances are employed. Table 5 summarises the intervals, number of elements, and distributions of tolerances and step sizes used in the parametric analysis. The simulations are conducted for each control law and for several values of the lightness number (see Table 3) to assess how sail performance affects the Stark model under time-varying perturbations. The effect of the initial orbit is not studied, since at each step the error is assumed to scale with the initial Keplerian elements, as previously shown in Fig. 7.

**Table 5**: Intervals, number of elements, and distributions of tolerances and step sizes employed for the parametric analysis with fixed step size.

| **Parameter** | Tolerance [-] | $\Delta t$ [s] |
|---|---|---|
| **Interval** | $[10^{-13}, 10^{-4}]$ | $[1, 100]$ |
| **Elements** | 11 | 33 |
| **Distribution** | Logarithmic | Divisors of 86400 (1 day) |

For each control law and lightness number, simulations are performed with the integration tolerances (numerical propagation) and step sizes (analytical propagation) shown in Table 5. This enables comparison in the computational time-accuracy space, identifying the regions where the Stark model outperforms numerical propagation and where the opposite holds. As an example, Fig. 8 shows the computational time-accuracy space for the simulations carried out for $\beta = 10^{-1}\beta_{ACS3}$. Numerical simulations exhibit an approximately linear relation between accuracy and computational cost with respect to tolerance. In contrast, the performance of the Stark model depends strongly on the

step size, which significantly influences computational cost, but to a lesser extent the accuracy for the step sizes considered. For certain step sizes, the Stark model achieves higher accuracy at lower computational cost than numerical propagation.

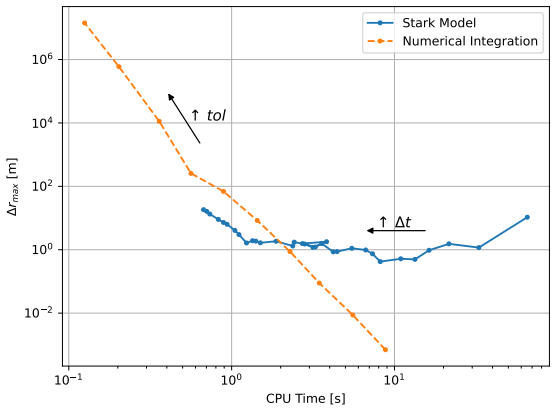


**Figure 8**: Computational time-accuracy space for the SMA-raising LOCL with $\beta = 10^{-1}\beta_{ACS3}$.

To assess the combinations of step size $\Delta t$ and lightness number $\beta$ for which the Stark model surpasses numerical integration in the time-accuracy space, a dedicated metric is introduced. Specifically, for each pair $(\Delta t, \beta)$, the aim is to determine whether the analytical solution achieves superior performance in terms of accuracy, computational cost, or both, when compared to numerical integrations carried out at different tolerances for the same $\beta$. The metric must therefore capture both computational time and position error. For example, in Fig. 8, Stark model points located to the left of the numerical integration curve are considered superior, since they achieve lower computational cost for a comparable accuracy. Conversely, points to the right are always outperformed by some numerical integration tolerance.

Consider all simulations, analytical (subscript $A$) and numerical (subscript $N$), for a fixed lightness number. Because both the computational time $\bar{t}$ and the position error $\bar{e}$ span several orders of magnitude, it is convenient to work with their logarithmic values:

$$\begin{aligned} \bar{\bar{t}} &= \log_{10}(\bar{t}) \\ \bar{\bar{e}} &= \log_{10}(\bar{e}) \end{aligned} \tag{70}$$

The computational time and position error are first normalised to allow a consistent comparison across simulations. To obtain a final metric bounded within a standard range, a min-max normalisation is applied as follows:

$$\begin{aligned} \bar{T} &= \frac{\bar{\bar{t}} - \min(\bar{\bar{t}})}{\max(\bar{\bar{t}}) - \min(\bar{\bar{t}})} \\ \bar{E} &= \frac{\bar{\bar{e}} - \min(\bar{\bar{e}})}{\max(\bar{\bar{e}}) - \min(\bar{\bar{e}})} \end{aligned} \tag{71}$$

Normalisation ensures $\bar{T}, \bar{E} \in [0, 1]$, where values close to zero correspond to low computational cost and low error. A cost function with equal weight to both contributions is then defined:

$$C = \frac{\bar{T} + \bar{E}}{2} \tag{72}$$

For each analytical simulation $j$, the Euclidean distance in the time-accuracy plane to each numerical simulation $i$ is computed as:

$$d_i = \sqrt{\left(\bar{T}_{N,i} - \bar{T}_{A,j}\right)^2 + \left(\bar{E}_{N,i} - \bar{E}_{A,j}\right)^2} \tag{73}$$

The closest numerical simulation $i^*$ is then identified, and the metric for the analytical simulation is defined as:

$$M_j = C_{N,i^*} - C_{A,j} \tag{74}$$

The metric $M_j$ defined in Eq. (74) quantifies the performance of the analytical simulation $j$ relative to the nearest numerical simulation $i^*$ in the time-accuracy plane. Its interpretation is as follows:

- $M_j > 0$: The analytical simulation outperforms the closest numerical simulation.
- $M_j = 0$: The analytical and closest numerical simulation perform equivalently.
- $M_j < 0$: The analytical simulation is outperformed by the closest numerical simulation.

Relating this definition of the metric $M$ to Fig. 8, points to the left of the numerical solutions' curve correspond to $M_j > 0$, points on the curve to $M_j = 0$, and points to the right to $M_j < 0$.

Figure 9 shows the values of the metric $M$ for different combinations of step size and lightness number for the LOCLs concerning the raising of the Keplerian elements: semi-major axis (SMA, Fig. 9a), eccentricity (Fig. 9b), inclination (Fig. 9c), right ascension of the ascending node (RAAN, Fig. 9d) and argument of periapsis (Fig. 9e). Furthermore, in these figures, the black dashed line indicates $M = 0$, along which the tolerances of the closest numerical solutions are annotated. The results show that for all LOCLs there exists a region where the Stark model outperforms numerical propagation. This region is smaller for out-of-plane control laws (inclination and RAAN). Moreover, smaller lightness numbers yield larger regions of outperformance. These results indicate that fixed step sizes penalise large perturbations due to loss of dynamical information, and especially penalise control laws involving sudden changes in perturbation direction. This issue is the case for inclination- and RAAN-raising control laws, for which the sail attitude changes abruptly when crossing the line of nodes. Finally, it is worth noting that, while under constant control laws larger lightness numbers reduce the position error (see Fig. 2), for time-varying perturbations they lead to less efficient solutions (see Fig. 9) because of increased loss of dynamical information.

*Variable Step Size* Following the same procedure as for the fixed-step-size analysis, the performance of the Stark model is compared against numerical integrations and assessed with the metric $M$. Each numerical integration under the tolerances in Table 5 provides a variable-step discretisation generated by the step-size adaptation algorithm of the RK45 scheme. These discretisations are then provided as inputs to the Stark model, which performs the analytical propagations using the same step distributions, each corresponding to a different tolerance. This approach enables the study of the Stark model under variable-step discretisations, which the analytical model itself cannot generate intrinsically.

Figure 10 shows the values of the metric $M$ for different combinations of the numerical-integration-tolerance discretisation and lightness number for the LOCLs concerning the raising of the Keplerian elements: SMA (Fig. 10a), eccentricity (Fig. 10b), inclination (Fig. 10c), RAAN (Fig. 10d) and argument of periapsis (Fig. 10e). Furthermore, in these figures, the black dashed line indicates $M = 0$, along which the tolerances of the closest numerical solutions are annotated.

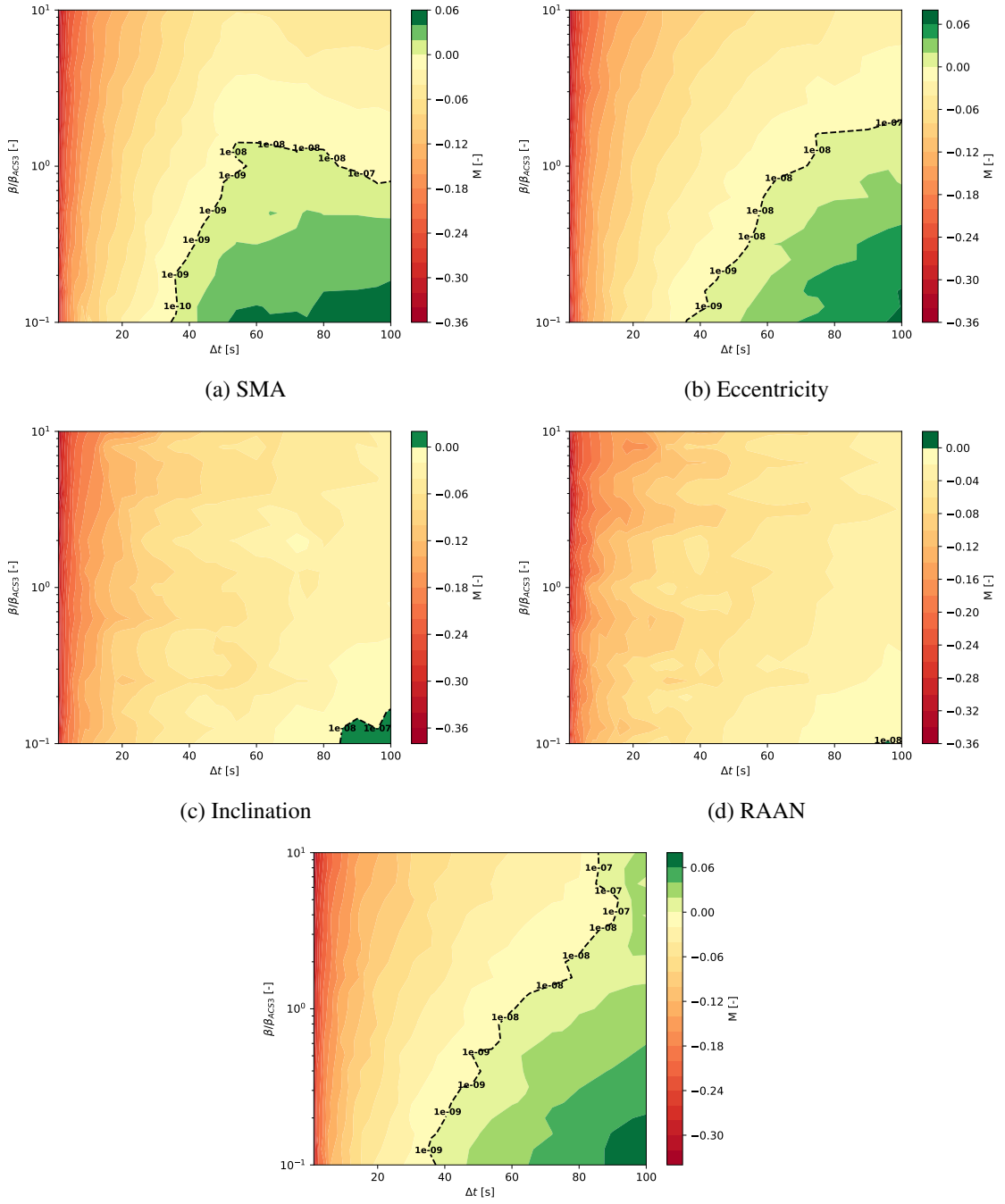


(a) SMA

(b) Eccentricity

(c) Inclination

(d) RAAN

(e) Argument of Periapsis

**Figure 9**: Metric $M$ for different combinations of $\Delta t$ and $\beta$ for various LOCLs: SMA (a), eccentricity (b), inclination (c), RAAN (d), and argument of periapsis (e). The black dashed line indicates $M = 0$, along which the tolerances of the closest numerical solutions are annotated.

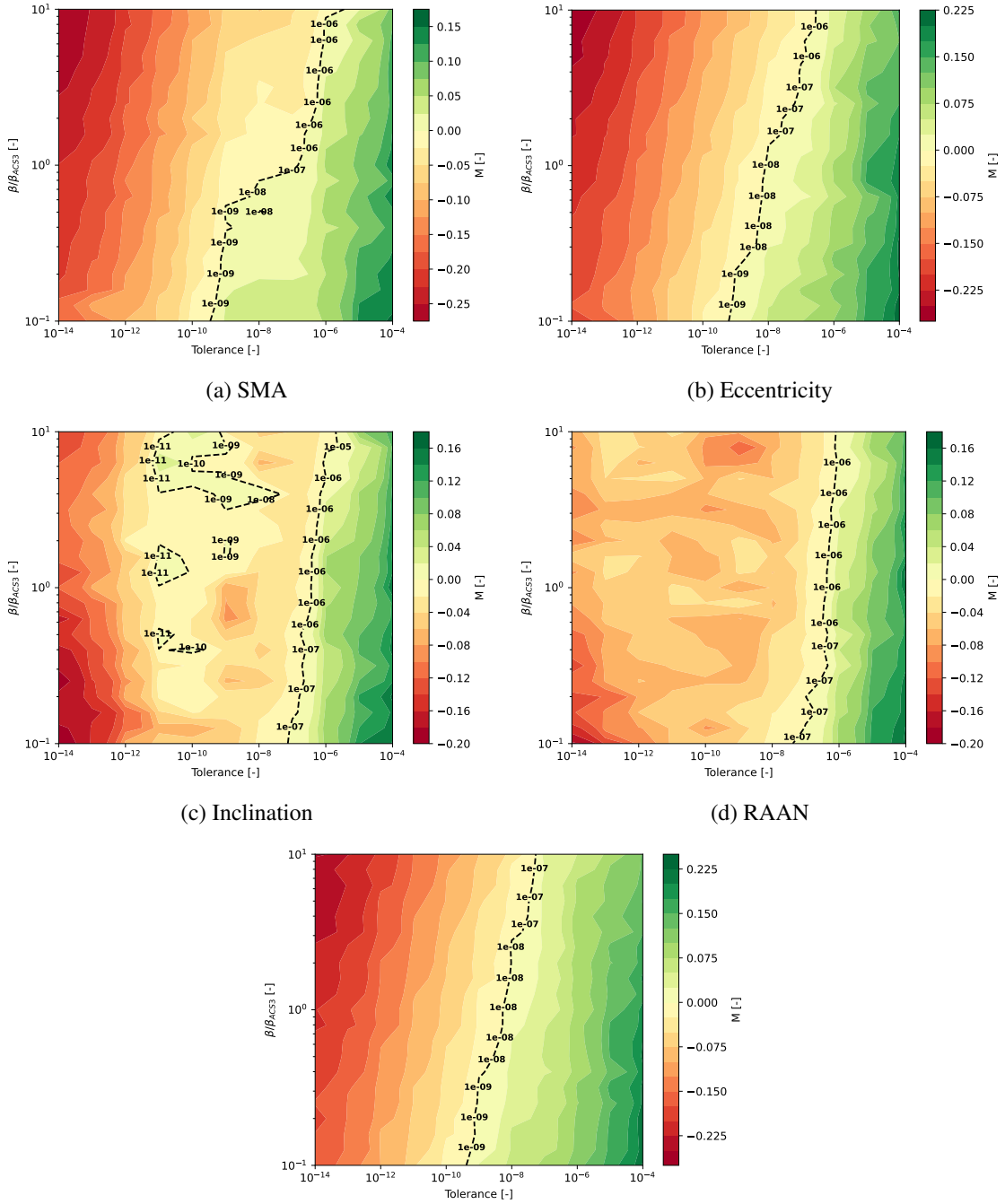


(a) SMA

(b) Eccentricity

(c) Inclination

(d) RAAN

(e) Argument of Periapsis

**Figure 10**: Metric $M$ for different combinations of the numerical-integration-tolerance discretisation and $\beta$ for various LOCLs: SMA (a), eccentricity (b), inclination (c), RAAN (d), and argument of periapsis (e). The black dashed line indicates $M = 0$, along which the tolerances of the closest numerical solutions are annotated.

As for the fixed-step analysis, the results show that for all LOCLs there exists a region where the Stark model outperforms numerical propagation. The general trend indicates that larger tolerances favour the Stark model relative to numerical integration. For out-of-plane control laws (inclination- and RAAN-raising), this trend is less uniform, allowing to find isolated regions for the inclination-raising control law on which the Stark model outperforms the numerical solution for tolerances of $tol \in \left[10^{-11}, 10^{-8}\right]$. Moreover, while smaller lightness numbers yield larger regions of outperformance, the effect is less pronounced than in the fixed-step analysis (see Fig. 9).

Overall, the use of variable-step discretisations allows the Stark model to outperform numerical solutions for tolerances in the range $tol \in \left[10^{-9}, 10^{-4}\right]$, range that varies depending on the control law. This behaviour arises because smaller tolerances lead to larger step sizes, where RK45 suffers from truncation errors due to its series formulation, while the Stark model preserves full dynamical accuracy regardless of step size. Control laws with abrupt changes in perturbation direction (inclination- and RAAN-raising) particularly benefit from variable discretisation, producing well-defined regions of outperformance. Similarly, larger lightness numbers also gain accuracy from variable-step propagation, as it improves the resolution of the underlying dynamics.

It should be noted, however, that these discretisations were externally provided to the Stark model. Thus, the computational overhead of step-size adaptation, included in the numerical integrations but not in the analytical propagations, is absent from the comparison. Consequently, the computational cost of the Stark model in this analysis is optimistic, leading to a slightly unfair performance assessment. Nonetheless, it still provides a qualitative indication of the Stark model's performance under variable-step propagation.

## CONCLUSION

This work has investigated the applicability of the Stark model as an analytical alternative to numerical integration methods for the simulation of controlled solar-sail trajectories in Earth orbit under solar radiation pressure. The motivation arises from the high computational cost of trajectory propagation during preliminary mission design, where efficient yet accurate propagation schemes are required.

The analysis demonstrates that the Stark model can outperform classical numerical integration methods in defined regions of the computational time-accuracy space. For constant control laws, the model consistently provided lower computational cost due to its ability to propagate the state at any given instant without sequential integration, while maintaining competitive accuracy. Position errors were found to range between $\Delta r_{\text{max}} \in [10^{-3}, 10^{3}]$, m for perturbation magnitudes of $\epsilon \in [10^{-9}, 10^{-3}]$, m/s$^2$. For time-varying, locally optimal control laws, performance strongly depended on the control strategy when a fixed-step discretisation strategy was considered. Smooth laws, such as semi-major axis-, eccentricity-, and argument of periapsis-raising, allowed the identification of step-size regions where the Stark model outperformed numerical integration. In contrast, abrupt control changes, such as inclination- and right ascension of ascending node-raising, significantly reduced the regions of outperformance due to the fixed-step limitation of the analytical formulation. With a variable-step discretisation strategy, the dynamics were captured more accurately, yielding solid regions of outperformance independently of the control law smoothness. Nonetheless, as the variable-step discretisations were provided externally, the Stark model did not account for the overhead of the step-size adaptation algorithm, resulting in optimistic computational times. Consequently, the variable-step analysis is considered qualitative.

The study further revealed that the solar-sail lightness number plays a dual role: larger values improve accuracy under constant control laws by reducing integration errors, but degrade performance for time-varying cases where fixed step sizes fail to capture more dynamic perturbations. Orbital parameters were also shown to influence the model's performance: semi-major axis and eccentricity have a direct impact on error growth and computational time, while angular elements, such as inclination or right ascension of the ascending node, were found to be negligible in this context.

Overall, the findings confirm that the Stark model constitutes a valuable analytical tool for preliminary solar-sail trajectory design, particularly in scenarios governed by smooth control laws. Future work should focus on overcoming the fixed-step limitation to better handle strongly time-varying perturbations and on extending the dynamical model to incorporate additional effects such as $J_2$, atmospheric drag, third-body perturbations, and eclipses. These advancements would enhance both the accuracy and the applicability of the Stark model in realistic mission design contexts.

## REFERENCES


[1] C. R. McInnes, *Solar sailing: technology, dynamics and mission applications*. Springer Science & Business Media, 2004.

[2] J. Heiligers, *Non-Keplerian Orbits Using Hybrid Solar Sail Propulsion for Earth Applications*. Phd thesis, University of Strathclyde, Department of Mechanical and Aerospace Engineering, 2012.

[3] M. Macdonald, C. McInnes, D. Alexander, and A. Sandman, "GeoSail: Exploring the magnetosphere using a low-cost solar sail," *Acta Astronautica*, Vol. 59, No. 8-11, 2006, pp. 757–767.

[4] J. R. Wertz, D. F. Everett, and J. J. Puschell, eds., *Space Mission Engineering: The New SMAD*. Hawthorne, CA: Microcosm Press, 2011.

[5] J. E. Prussing and B. A. Conway, *Orbital mechanics*. Oxford University Press, 1993.

[6] V. R. Bond and M. C. Allman, "Modern astrodynamics: fundamentals and perturbation methods," 2021.

[7] D. A. Vallado, *Fundamentals of astrodynamics and applications*, Vol. 12. Springer Science & Business Media, 2001.

[8] Z. Yu, W. Chen, and W. Yu, "Analytical trajectory prediction of high-eccentricity spacecraft transfer orbits considering J2 perturbation," *Aerospace Science and Technology*, Vol. 153, 2024, p. 109462.

[9] D. Arnas, "Analytic frozen and other low eccentric orbits under J2 perturbation," *arXiv preprint arXiv:2212.09958*, 2022.

[10] G. Linyu, W. Nan, M. Fankun, and H. Jiaying, "A analytical method of trajectory prediction considering J 2 perturbations and including short-period terms," *2018 4th International Conference on Control, Automation and Robotics (ICCAR)*, IEEE, 2018, pp. 498–503.

[11] K. Hernandez, J. L. Read, T. A. Elgohary, J. D. Turner, and J. L. Junkins, "Analytic power series solutions for two-body and J2–J6 trajectories and state transition models," *Advances in Astronautical Sciences: AAS/AIAA Astrodynamics Specialist Conference*, 2015.

[12] D. J. Jezewski, "A noncanonical analytic solution to the J 2 perturbed two-body problem," *Celestial mechanics*, Vol. 30, No. 4, 1983, pp. 343–361.

[13] V. R. Bond, "An Analytical Singularity-Free Solution to the J2 Perturbation Problem," tech. rep., 1979.

[14] B. Kuiack and S. Ulrich, "Nonlinear Analytical Equations of Relative Motion on J 2-Perturbed Eccentric Orbits," *Journal of Guidance, Control, and Dynamics*, Vol. 41, No. 12, 2018, pp. 2666–2677.

[15] Z. Yang, Y.-Z. Luo, and J. Zhang, "Second-Order Analytical Solution of Relative Motion in J 2-Perturbed Elliptic Orbits," *Journal of Guidance, Control, and Dynamics*, Vol. 41, No. 10, 2018, pp. 2258–2270.

[16] S. R. Vadali, "Model for linearized satellite relative motion about a J2-perturbed mean circular orbit," *Journal of guidance, control, and dynamics*, Vol. 32, No. 5, 2009, pp. 1687–1691.

[17] S. Breiter and A. Jackson, "Unified analytical solutions to two-body problems with drag," *Monthly Notices of the Royal Astronomical Society*, Vol. 299, No. 1, 1998, pp. 237–243.

[18] D. Mittleman and D. Jezewski, "An analytic solution to the classical two-body problem with drag," *Celestial mechanics*, Vol. 28, 1982, pp. 401–413.

[19] T. Nie, S. Zhang, T. Yi, and J. Ren, "Analytical Solution for Third-Body Perturbations with Double Averaging," *Journal of Guidance, Control, and Dynamics*, Vol. 48, No. 2, 2025, pp. 384–392.

[20] T. Nie, P. Gurfil, and S. Zhang, "Semi-analytical model for third-body perturbations including the inclination and eccentricity of the perturbing body," *Celestial Mechanics and Dynamical Astronomy*, Vol. 131, 2019, pp. 1–31.

[21] C. R. H. Solórzano, A. Prado, and H. Kuga, "Third-body perturbation using a single averaged model," *Advances in Space Dynamics*, Vol. 4, 2002, pp. 47–56.

[22] R. Jin, Z. Fan, M. Huo, Y. Xu, and N. Qi, "Analytical Trajectory of Solar Sail With Fixed Pitch Angle From Elliptical Orbits," *IEEE Transactions on Aerospace and Electronic Systems*, Vol. 60, No. 3, 2024, pp. 2833–2842.

[23] J. Qi, R. Jin, C. Zhao, Z. Gao, W. Feng, Z. Fan, and M. Huo, "Optimal multi-segment trajectory of solar sail with analytical approximation," *Aerospace Science and Technology*, Vol. 153, 2024, p. 109384.

[24] M. Bassetto, A. A. Quarta, G. Mengali, and V. Cipolla, "Spiral trajectories induced by radial thrust with applications to generalized sails," *Astrodynamics*, Vol. 5, 2021, pp. 121–137.

[25] M. Bassetto, A. A. Quarta, and G. Mengali, "Generalized sail trajectory approximation with applications to MagSails," *Aerospace Science and Technology*, Vol. 118, 2021, p. 106991.

[26] J. Van Der Ha and V. Modi, "Long-term evaluation of three-dimensional heliocentric solar sail trajectories with arbitrary fixed sail setting," *Celestial mechanics*, Vol. 19, 1979, pp. 113–138.

[27] B. Stewart, P. Palmer, and M. Roberts, "An analytical description of three-dimensional heliocentric solar sail orbits," *Celestial Mechanics and Dynamical Astronomy*, Vol. 128, No. 1, 2017, pp. 61–74.

[28] Y. Isayev and A. Kunitsyn, "To the problem of satellite's perturbed motion under the influence of solar radiation pressure," *Celestial mechanics*, Vol. 6, No. 1, 1972, pp. 44–51.

[29] G. Lantoine and R. P. Russell, "The Stark Model: an exact, closed-form approach to low-thrust trajectory optimization," *21st International Symposium on Space Flight Dynamics*, 2009.

[30] G. Lantoine and R. P. Russell, "Complete closed-form solutions of the Stark problem," *Celestial Mechanics and Dynamical Astronomy*, Vol. 109, 2011, pp. 333–366.

[31] F. Biscani and D. Izzo, "The Stark problem in the Weierstrassian formalism," *Monthly Notices of the Royal Astronomical Society*, Vol. 439, No. 1, 2014, pp. 810–822.

[32] E. Pellegrini, R. P. Russell, and V. Vittaldev, "F and G Taylor series solutions to the Stark and Kepler problems with Sundman transformations," *Celestial Mechanics and Dynamical Astronomy*, Vol. 118, No. 4, 2014, pp. 355–378.

[33] D. Rufer, "Trajectory optimization by making use of the closed solution of constant thrust-acceleration motion," *Celestial mechanics*, Vol. 14, No. 1, 1976, pp. 91–103.

[34] N. Hatten and R. P. Russell, "Application of the stark problem to space trajectories with time-varying perturbations," *methods*, Vol. 6, p. 12.

[35] N. Hatten and R. P. Russell, "Comparison of three Stark problem solution techniques for the bounded case," *Celestial Mechanics and Dynamical Astronomy*, Vol. 121, No. 1, 2015, pp. 39–60.

[36] M. Macdonald and C. R. McInnes, "Analytical control laws for planet-centered solar sailing," *Journal of Guidance, Control, and Dynamics*, Vol. 28, No. 5, 2005, pp. 1038–1048.

[37] A. Fasano and S. Marmi, *Analytical mechanics: an introduction*. OUP Oxford, 2006.

[38] B. C. Carlson, "Elliptic integrals.," *NIST Handbook of Mathematical Functions*, Vol. 1, 2010, pp. 485–522.

[39] W. P. Reinhardt and P. L. Walker, "Jacobian elliptic functions.," *NIST Handbook of Mathematical Functions*, Vol. 1, 2010, pp. 549–568.

[40] P. F. Byrd and M. D. Friedman, *Handbook of elliptic integrals for engineers and physicists*, Vol. 67. Springer, 2013.

[41] K. F. Wakker, "Fundamentals of astrodynamics," *TU Delft Repository, Delft*, 2015, pp. 604–612.

[42] K. Wilkie and J. Fernandez, "Advanced Composite Solar Sail System (ACS3) Mission Update," *The 6th International Symposium on Space Sailing*, 2023.

[43] U.S. Space Command, "Space-Track.org," `https://www.space-track.org/`. Accessed: 7 July 2025.

[44] S. C. Chapra, R. P. Canale, *et al.*, *Numerical methods for engineers*, Vol. 1221. Mcgraw-hill New York, 2011.

[45] Analytical and Computational Mathematics, Inc., "Application and Analysis of Satellite Orbit Prediction Techniques," jsc internal note no. 77-fm-19, NASA Johnson Space Center, Houston, TX, 1977. JSC Task Monitor: George A. Weisskopf.

[46] I. Wolfram Research, "Mathematica, Version 14.2," `https://www.wolfram.com/mathematica`. Champaign, IL, 2025.

# 7

# Conclusions and Recommendations for Future Work

This chapter finalises the work by presenting the main conclusions derived from the research and outlining recommendations for future developments. Section 7.1 revisits the research objective and systematically answers the main research question and sub-questions, based on the results obtained. Section 7.2 then proposes directions for future work, taking into account both the findings and the limitations identified.

## 7.1. Conclusions

While heliocentric solar sailing has traditionally attracted the most attention, Earth-centred solar sailing is emerging as a promising concept. In particular, solar radiation pressure (SRP) enables sustained non-Keplerian behaviour that can be exploited for novel mission applications.

Mission design requires extensive simulations, which result in significant computational cost. During the preliminary design phase, low-fidelity models are typically used to reduce this cost. Analytical models can further provide efficient alternatives to such numerical approaches. Among these, the Stark model offers a convenient analytical framework to capture first-order deviations from Keplerian motion, such as SRP perturbations, while still admitting closed- or semi-closed-form solutions.

On this basis, the research objective of this thesis was formulated as:

> *Investigate the performance, in terms of accuracy and computational cost, of the Stark model in the context of a controlled solar sail orbiting around Earth, under the effect of point-mass gravity and solar radiation pressure, for different simulation scenarios.*

The Stark model was implemented following a Hamilton-Jacobi formulation of the SRP-perturbed two-body problem (TBP). A numerical acceleration model was also implemented as a reference. Both analytical and numerical formulations assume:

- The Sun-sail distance is constant and equal to the mean Sun-Earth distance.
- The solar flux is modelled under the parallel-rays approximation.
- Orbital eclipses are neglected.
- The solar sail is considered ideal.

In order to address the controlled aspect of the problem, both a constant control law and planet-centred solar-sail locally optimal control laws (LOCLs) were considered. The latter correspond to the raising of the following orbital elements: semi-major axis (SMA), eccentricity, inclination, right ascension of the ascending node (RAAN), and argument of periapsis.

The research objective is studied through the answering of the research question and its sub-questions, which are presented and answered below.

**Research Question**

Can the Stark model serve as a reliable alternative to numerical integration methods for preliminary design of controlled solar-sail trajectories around Earth under the effect of point-mass gravity and solar radiation pressure?

The analysis demonstrates that the Stark model can indeed outperform conventional numerical integration methods within certain regions of the computational time-accuracy space.

For constant control laws, the Stark model consistently provided superior computational efficiency, as it allows direct propagation of the state at any time instant. Accuracy depends on the perturbation magnitude: larger perturbations yield smaller errors, with position errors spanning $\Delta r_{max} \in \left[10^{-3}, 10^{3}\right]$ m, for perturbation magnitudes in the range of $\epsilon \in \left[10^{-9}, 10^{-3}\right]$ m/s$^2$.

For time-varying control laws, the regions of outperformance strongly depend on the chosen control law under a fixed-step discretisation. Laws characterised by abrupt directional changes, such as inclination- and RAAN-raising, significantly reduce the regions where the Stark model outperforms numerical integration. Conversely, smooth laws, such as SMA-, eccentricity-, and argument of periapsis-raising, allow broader regions of advantage. Analytical solutions that attained comparable or better performance than numerical solutions were only found for numerical integrations with tolerances $tol \in \left[10^{-10}, 10^{-7}\right]$. The associated numerical integration errors in these cases were bounded by $\Delta r_{max} \in \left[10^{-1}, 10^{3}\right]$ m. Under a variable-step discretisation strategy, the improved accuracy in capturing the dynamics led to solid regions of where the Stark model outperforms the numerical integration, independent of control law smoothness. Nonetheless, this analysis remains qualitative, as the variable-step discretisations were provided externally, yielding optimistic computational cost estimates.

**Sub-question 1**

How does the performance of the Stark model compare to numerical integration methods when simulating solar-sail trajectories governed by a constant control law?

The Stark model predicts the state of a solar-sail trajectory governed by a constant control law in a single integration step. The maximum position error increases with integration time and depends on the perturbation magnitude. For perturbations of $\epsilon \in \left[10^{-9}, 10^{-3}\right]$ m/s$^2$, one-day trajectories exhibit maximum position errors in the range of $\Delta r_{max} \in \left[10^{-3}, 10^{3}\right]$ m.

These errors originate from inaccuracies in the evaluation of intermediate functions, such as elliptic integrals, that grow with increasing integration time. This translates into a mismatch between the physical time at which the Stark model evaluates the solution and the reference time of the numerical solution, thereby producing state deviations. Similar behaviour in accuracy was observed regardless of whether the integration used physical time $t$ or fictitious time $\tau_1$.

In terms of computational efficiency, integration in physical time requires on the order of $10^{-4}$ s per evaluation, compared to $10^{-6}$ s for fictitious time. The difference arises from the need to invert the implicit Stark equation when using physical time as the independent variable.

**Sub-question 2**

How does the performance of the Stark model compare to numerical integration methods when simulating solar-sail trajectories governed by time-varying locally optimal control laws?

The performance of the Stark model under time-varying control laws depends strongly on the nature of the law. Since the model requires fixed integration steps and does not allow adaptive step-size control, its efficiency is reduced compared to numerical methods in cases involving rapid variations.

For smooth laws (SMA-, eccentricity-, and argument of periapsis-raising), the Stark model outperformed numerical methods in regions corresponding to step sizes of $\Delta t \in [36, 100]$ s, with numerical methods requiring tolerances of $tol \in \left[10^{-10}, 10^{-7}\right]$ to achieve similar accuracy. For abruptly changing laws (inclination- and RAAN-raising), the region of outperformance is much narrower with step sizes of $\Delta t \in [90, 100]$ s and associated numerical tolerances of $tol \in \left[10^{-8}, 10^{-7}\right]$.

Additional analyses were performed by supplying the Stark model with the variable-step discretisations generated by the step-size adaptation algorithm of the numerical integration scheme. The results showed improved accuracy in capturing the dynamics, with the Stark model outperforming numerical integration for all control laws over tolerance ranges of $tol \in \left[10^{-9}, 10^{-4}\right]$ (slightly varying with the control law). These findings highlight a key model limitation: the inability to internally adapt step sizes under time-varying perturbations.

**Sub-question 3**

How does the solar-sail lightness number affect the performance of the Stark model?

The effect of the lightness number $\beta$ is twofold. Under constant control laws, larger values of the lightness number improve performance, since stronger SRP perturbations lead to smaller relative errors. Conversely, under time-varying control laws, larger values of the lightness number worsen performance, as the stronger perturbations hinder the fixed-step Stark model's ability to capture the dynamics accurately.

For inclination- and RAAN-raising laws, regions of outperformance were only found at smaller lightness number values $\beta \approx 10^{-1}\beta_{ACS3}$, with $\beta_{ACS3} = 0.0077$. For SMA- and eccentricity-raising laws, these regions extended to $\beta \in \left[10^{-1}, 10^{0}\right] \beta_{ACS3}$, while for argument of periapsis-raising laws, outperformance was observed across the entire studied interval, $\beta \in \left[10^{-1}, 10^{1}\right] \beta_{ACS3}$.

In the variable-step analysis for time-varying control laws, this dependence was less pronounced, with regions of outperformance for all control laws over the entire range of lightness numbers.

**Sub-question 4**

How do orbit parameters affect the performance of the Stark model?

The influence of orbital parameters on performance was found to be selective. Angular parameters (inclination, RAAN, argument of periapsis, and true anomaly) do not affect either accuracy or computational time, as they do not alter the orbital dynamics. In contrast, SMA and eccentricity strongly influence both. Smaller SMA and larger eccentricities, which correspond to faster orbital dynamics, increase both position errors and computational time per evaluation. This behaviour is attributed to greater sensitivity to small time deviations between the Stark model and numerical solutions in fast-dynamic regimes.

## 7.2. Recommendations for Future Work

The conclusions in Section 7.1 have highlighted several limitations of the Stark model, which in turn suggest potential directions for future research. As the performance assessment was carried out separately for constant and time-varying control laws, the recommendations are likewise structured according to this distinction.

For constant control laws (and, by extension, for each individual step in the integration of time-varying perturbations), the main limitation arises from numerical noise in the evaluation of intermediate functions. This noise is amplified by the reciprocal of the perturbation magnitude, ultimately constraining accuracy. Since the origin of this limitation is the finite precision of floating-point arithmetic, it cannot be fully eliminated. A straightforward mitigation strategy is to employ higher-precision arithmetic, trading computational cost for improved accuracy. This additional cost could, however, be partially offset by using the fictitious time $\tau_1$ as the independent variable instead of the physical time $t$, allowing for a reduction in the computational time per evaluation by approximately two orders of magnitude.

In the case of time-varying control laws, the primary limitation is the inability of the Stark model to cap-

ture the underlying dynamics with a fixed step size. Classical numerical integration schemes achieve step-size adaptability by exploiting error estimates between solutions of different orders, a feature not directly transferable to the analytical solution provided by the Lantoine formulation [35, 70]. One possible avenue to address this issue is the Pellegrini formulation [73], which employs a series expansion to solve the Stark problem. Although this approach restricts the maximum step size, it provides higher accuracy for smaller step sizes [74]. Moreover, the series expansion framework may enable the development of adaptive step-size schemes for the Stark model.

In the context of time-varying perturbations, future work could also aim to expand the acceleration model to include additional perturbations such as $J_2$, atmospheric drag, or third-body effects. Depending on the cumulative effect of these perturbations, the accuracy of the model may improve due to the larger effective perturbation magnitude. Furthermore, in the context of planet-centred solar sailing, incorporating the effect of orbital eclipses would be particularly valuable, as eclipses are especially relevant in low-Earth orbit regimes.

In summary, the recommendations outlined above address two complementary aspects: mitigating numerical limitations inherent to the Stark model and extending its applicability through a broader dynamical framework. Together, these directions define a clear path towards enhancing both the accuracy and versatility of the Stark model for future solar-sail trajectory design studies.

# References


[1] C. R. McInnes, *Solar sailing: technology, dynamics and mission applications*. Springer Science & Business Media, 2004.

[2] J. L. Wright, *Space sailing*. Taylor & Francis, 1992.

[3] K. Wilkie and J. Fernandez, "Advanced composite solar sail system (ACS3) mission update," in *The 6th International Symposium on Space Sailing*, 2023.

[4] B. Dachwald *et al.*, "Potential solar sail degradation effects on trajectory and attitude control," in *AIAA guidance, navigation, and control conference and exhibit*, 2005, p. 6172.

[5] B. Dachwald, M. Macdonald, C. R. McInnes, G. Mengali, and A. A. Quarta, "Impact of optical degradation on solar sail mission performance," *Journal of Spacecraft and Rockets*, vol. 44, no. 4, pp. 740–749, 2007.

[6] J. Kepler, *Ioannis Kepleri mathematici Cæsarei Dissertatio cum Nuncio sidereo: nuper ad mortales misso à Galilæo Galilæo mathematico Patavino*. H.F. Schulz in Kommission, 1610.

[7] J. C. Maxwell, *A Treatise on Electricity and Magnetism*. Oxford: Clarendon Press, 1873, vol. 1.

[8] M. Urbanczyk, "Solar sails-a realistic propulsion for spacecraft," Redstone Scientific Information Center, U.S. Army Missile Command, Tech. Rep., 1967.

[9] W. A. Hollerman, "The physics of solar sails," *The 2002 NASA Faculty Fellowship Program Research Reports*, 2003.

[10] F. A. Tsander, *From a Scientific Heritage*. Washington D.C.: NASA, 1969, NASA Technical Translation TT-F-541. [Online]. Available: `https://epizodyspace.ru/bibl/inostr-yazyki/nasa/Tsander_From_a_Scientific_Heritage_1969.pdf`.

[11] D. S. Chronicle, "A chronology of deep space and planetary probes 1958–2000," *Siddiqi, AA*, 2002.

[12] D. J. O'Shaughnessy, J. V. McAdams, K. E. Williams, and B. R. Page, "Fire sail: Messenger's use of solar radiation pressure for accurate mercury flybys," *Advances in the Astronautical Sciences*, vol. 133, no. Part I, 2009.

[13] Y. Tsuda *et al.*, "Achievement of ikaros—japanese deep space solar sail demonstration mission," *Acta Astronautica*, vol. 82, no. 2, pp. 183–188, 2013.

[14] G. Vulpetti, L. Johnson, G. L. Matloff, G. Vulpetti, L. Johnson, and G. L. Matloff, "The nanosail-d2 nasa mission," *Solar Sails: A Novel Approach to Interplanetary Travel*, pp. 173–178, 2015.

[15] T. P. Society, *The planetary society: Advancing space exploration*, Accessed: 8 February 2025., 2025. [Online]. Available: `https://www.planetary.org`.

[16] eoPortal, *Lightsail missions of the planetary society*, Last updated: 1 June 2012; Accessed: 8 February 2025., 2025. [Online]. Available: `https://www.eoportal.org/satellite-missions/lightsail`.

[17] D. A. Spencer, B. Betts, J. M. Bellardo, A. Diaz, B. Plante, and J. R. Mansell, "The lightsail 2 solar sailing technology demonstration," *Advances in Space Research*, vol. 67, no. 9, pp. 2878–2889, 2021.

[18] E. Ancona and R. Y. Kezerashvili, "Recent advances in space sailing missions and technology: Review of the 6th international symposium on space sailing (isss 2023)," *arXiv preprint arXiv:2411.12492*, 2024.

[19] NASA, "Advanced composite solar sail system (ACS3)," National Aeronautics and Space Administration, Tech. Rep., 2025, Accessed: 8 February 2025. [Online]. Available: `https://www.nasa.gov/smallspacecraft/what-is-acs3`.

[20] J. R. Mansell, J. M. Bellardo, B. Betts, B. Plante, and D. A. Spencer, “Lightsail 2 solar sail control and orbit evolution,” *Aerospace*, vol. 10, no. 7, p. 579, 2023.

[21] Y. Tsuda *et al.*, “Flight status of ikaros deep space solar sail demonstrator,” *Acta astronautica*, vol. 69, no. 9-10, pp. 833–840, 2011.

[22] C. R. McInnes, “Solar sail mission applications for non-keplerian orbits,” *Acta Astronautica*, vol. 45, no. 4-9, pp. 567–575, 1999.

[23] L. Johnson *et al.*, “The nasa solar cruiser mission – solar sail propulsion enabling heliophysics missions,” in *Proceedings of the 36th Annual Small Satellite Conference*, 2022.

[24] M. Macdonald, C. McInnes, D. Alexander, and A. Sandman, “Geosail: Exploring the magnetosphere using a low-cost solar sail,” *Acta Astronautica*, vol. 59, no. 8-11, pp. 757–767, 2006.

[25] J. Heiligers, “Non-keplerian orbits using hybrid solar sail propulsion for earth applications,” PhD thesis, University of Strathclyde, Department of Mechanical and Aerospace Engineering, 2012.

[26] M. Planck, *Zur Theorie des Gesetzes der Energieverteilung im Normalspektrum*. Verhandlungen der Deutschen Physikalischen Gesellschaft, 1900, Original derivation of Planck’s law and energy quanta.

[27] A. Einstein, “Ist die trägheit eines körpers von seinem energieinhalt abhängig?” *Annalen der Physik*, vol. 18, pp. 639–641, 1905, First formulation of mass-energy equivalence, $E = mc^2$. DOI: 10.1002/andp.19053231314.

[28] M. Planck, “Zur dynamik bewegter systeme,” *Annalen der Physik*, vol. 325, pp. 1–34, 1906, First derivation of the energy–momentum relation in relativistic dynamics. DOI: 10.1002/andp.19063250506.

[29] S. M. Thompson, N. Pushparaj, and C. Cappelletti, “Reflective and transmissive solar sails: Dynamics, flight regimes and applications,” *Acta Astronautica*, vol. 220, pp. 478–494, 2024.

[30] S. Pyykol, N. Joswig, L. Ruotsalainen, *et al.*, “Non-lambertian surfaces and their challenges for visual slam,” *IEEE Open Journal of the Computer Society*, 2024.

[31] M. Macdonald and C. R. McInnes, “Analytical control laws for planet-centered solar sailing,” *Journal of Guidance, Control, and Dynamics*, vol. 28, no. 5, pp. 1038–1048, 2005.

[32] L. Carzana, P. Visser, and J. Heiligers, “Locally optimal control laws for earth-bound solar sailing with atmospheric drag,” *Aerospace Science and Technology*, vol. 127, p. 107 666, 2022.

[33] I. Newton, *Philosophiae naturalis principia mathematica*. G. Brookman, 1833, vol. 1.

[34] H. Varvoglis, C. Vozikis, and K. Wodnar, “The two fixed centers: An exceptional integrable system,” *Celestial Mechanics and Dynamical Astronomy*, vol. 89, no. 4, pp. 343–356, 2004.

[35] G. Lantoine and R. P. Russell, “The stark model: An exact, closed-form approach to low-thrust trajectory optimization,” in *21st International Symposium on Space Flight Dynamics*, 2009.

[36] E. Hairer, G. Wanner, and S. P. Nørsett, *Solving ordinary differential equations I: Nonstiff problems*. Springer, 1993.

[37] J. C. Butcher, *Numerical methods for ordinary differential equations*. John Wiley & Sons, 2016.

[38] W. H. Press, *Numerical recipes 3rd edition: The art of scientific computing*. Cambridge university press, 2007.

[39] L. F. Shampine and M. W. Reichelt, “The matlab ode suite,” *SIAM journal on scientific computing*, vol. 18, no. 1, pp. 1–22, 1997.

[40] J. Stoer, R. Bulirsch, R. Bartels, W. Gautschi, and C. Witzgall, *Introduction to numerical analysis*. Springer, 1980, vol. 1993.

[41] J. E. Prussing and B. A. Conway, *Orbital mechanics*. Oxford University Press, 1993.

[42] J. R. Wertz, D. F. Everett, and J. J. Puschell, Eds., *Space Mission Engineering: The New SMAD*. Hawthorne, CA: Microcosm Press, 2011, ISBN: 978-1-881883-15-9.

[43] D. A. Vallado, *Fundamentals of astrodynamics and applications*. Springer Science & Business Media, 2001, vol. 12.

[44] V. R. Bond and M. C. Allman, “Modern astrodynamics: Fundamentals and perturbation methods,” 2021.

[45] A. H. Nayfeh, *Perturbation methods*. John Wiley & Sons, 2024.

[46] Z. Yu, W. Chen, and W. Yu, “Analytical trajectory prediction of high-eccentricity spacecraft transfer orbits considering j2 perturbation,” *Aerospace Science and Technology*, vol. 153, p. 109 462, 2024.

[47] D. Arnas, “Analytic frozen and other low eccentric orbits under j2 perturbation,” *arXiv preprint arXiv:2212.09958*, 2022.

[48] G. Linyu, W. Nan, M. Fankun, and H. Jiaying, “A analytical method of trajectory prediction considering j 2 perturbations and including short-period terms,” in *2018 4th International Conference on Control, Automation and Robotics (ICCAR)*, IEEE, 2018, pp. 498–503.

[49] K. Hernandez, J. L. Read, T. A. Elgohary, J. D. Turner, and J. L. Junkins, “Analytic power series solutions for two-body and j2–j6 trajectories and state transition models,” in *Advances in Astronautical Sciences: AAS/AIAA Astrodynamics Specialist Conference*, 2015.

[50] D. J. Jezewski, “A noncanonical analytic solution to the j 2 perturbed two-body problem,” *Celestial mechanics*, vol. 30, no. 4, pp. 343–361, 1983.

[51] V. R. Bond, “An analytical singularity-free solution to the j2 perturbation problem,” Tech. Rep., 1979.

[52] B. Kuiack and S. Ulrich, “Nonlinear analytical equations of relative motion on j 2-perturbed eccentric orbits,” *Journal of Guidance, Control, and Dynamics*, vol. 41, no. 12, pp. 2666–2677, 2018.

[53] Z. Yang, Y.-Z. Luo, and J. Zhang, “Second-order analytical solution of relative motion in j 2-perturbed elliptic orbits,” *Journal of Guidance, Control, and Dynamics*, vol. 41, no. 10, pp. 2258–2270, 2018.

[54] S. R. Vadali, “Model for linearized satellite relative motion about a j2-perturbed mean circular orbit,” *Journal of guidance, control, and dynamics*, vol. 32, no. 5, pp. 1687–1691, 2009.

[55] S. Breiter and A. Jackson, “Unified analytical solutions to two-body problems with drag,” *Monthly Notices of the Royal Astronomical Society*, vol. 299, no. 1, pp. 237–243, 1998.

[56] D. Mittleman and D. Jezewski, “An analytic solution to the classical two-body problem with drag,” *Celestial mechanics*, vol. 28, pp. 401–413, 1982.

[57] T. Nie, S. Zhang, T. Yi, and J. Ren, “Analytical solution for third-body perturbations with double averaging,” *Journal of Guidance, Control, and Dynamics*, vol. 48, no. 2, pp. 384–392, 2025.

[58] T. Nie, P. Gurfil, and S. Zhang, “Semi-analytical model for third-body perturbations including the inclination and eccentricity of the perturbing body,” *Celestial Mechanics and Dynamical Astronomy*, vol. 131, pp. 1–31, 2019.

[59] C. R. H. Solórzano, A. Prado, and H. Kuga, “Third-body perturbation using a single averaged model,” *Advances in Space Dynamics*, vol. 4, pp. 47–56, 2002.

[60] R. Jin, Z. Fan, M. Huo, Y. Xu, and N. Qi, “Analytical trajectory of solar sail with fixed pitch angle from elliptical orbits,” *IEEE Transactions on Aerospace and Electronic Systems*, vol. 60, no. 3, pp. 2833–2842, 2024.

[61] J. Qi *et al.*, “Optimal multi-segment trajectory of solar sail with analytical approximation,” *Aerospace Science and Technology*, vol. 153, p. 109 384, 2024.

[62] M. Bassetto, A. A. Quarta, G. Mengali, and V. Cipolla, “Spiral trajectories induced by radial thrust with applications to generalized sails,” *Astrodynamics*, vol. 5, pp. 121–137, 2021.

[63] M. Bassetto, A. A. Quarta, and G. Mengali, “Generalized sail trajectory approximation with applications to magsails,” *Aerospace Science and Technology*, vol. 118, p. 106 991, 2021.

[64] J. Van Der Ha and V. Modi, “Long-term evaluation of three-dimensional heliocentric solar sail trajectories with arbitrary fixed sail setting,” *Celestial mechanics*, vol. 19, pp. 113–138, 1979.

[65] B. Stewart, P. Palmer, and M. Roberts, “An analytical description of three-dimensional heliocentric solar sail orbits,” *Celestial Mechanics and Dynamical Astronomy*, vol. 128, no. 1, pp. 61–74, 2017.

[66] Y. Isayev and A. Kunitsyn, “To the problem of satellite’s perturbed motion under the influence of solar radiation pressure,” *Celestial mechanics*, vol. 6, no. 1, pp. 44–51, 1972.

[67] J. L. Lagrange, *Mécanique analytique*. Mallet-Bachelier, 1853, vol. 1.

[68] U. Kirchgraber, “A problem of orbital dynamics, which is separable in ks-variables,” *Celestial mechanics*, vol. 4, no. 3-4, pp. 340–347, 1971.

[69] D. Rufer, “Trajectory optimization by making use of the closed solution of constant thrust-acceleration motion,” *Celestial mechanics*, vol. 14, no. 1, pp. 91–103, 1976.

[70] G. Lantoine and R. P. Russell, “Complete closed-form solutions of the stark problem,” *Celestial Mechanics and Dynamical Astronomy*, vol. 109, pp. 333–366, 2011.

[71] N. Hatten and R. P. Russell, “Application of the stark problem to space trajectories with time-varying perturbations,” *methods*, vol. 6, p. 12,

[72] F. Biscani and D. Izzo, “The stark problem in the weierstrassian formalism,” *Monthly Notices of the Royal Astronomical Society*, vol. 439, no. 1, pp. 810–822, 2014.

[73] E. Pellegrini, R. P. Russell, and V. Vittaldev, “F and G taylor series solutions to the stark and kepler problems with sundman transformations,” *Celestial Mechanics and Dynamical Astronomy*, vol. 118, no. 4, pp. 355–378, 2014.

[74] N. Hatten and R. P. Russell, “Comparison of three stark problem solution techniques for the bounded case,” *Celestial Mechanics and Dynamical Astronomy*, vol. 121, no. 1, pp. 39–60, 2015.

[75] W. P. Reinhardt and P. L. Walker, “Jacobian elliptic functions.,” *NIST Handbook of Mathematical Functions*, vol. 1, pp. 549–568, 2010.

[76] K. L. Sala, “Transformations of the jacobian amplitude function and its calculation via the arithmetic-geometric mean,” *SIAM Journal on Mathematical Analysis*, vol. 20, no. 6, pp. 1514–1528, 1989.

[77] T. Fukushima, “Fast computation of jacobian elliptic functions and incomplete elliptic integrals for constant values of elliptic parameter and elliptic characteristic,” *Celestial Mechanics and Dynamical Astronomy*, vol. 105, pp. 245–260, 2009.

[78] T. Fukushima, “Fast computation of complete elliptic integrals and jacobian elliptic functions,” *Celestial Mechanics and Dynamical Astronomy*, vol. 105, pp. 305–328, 2009.

[79] A. Fasano and S. Marmi, *Analytical mechanics: an introduction*. OUP Oxford, 2006.

[80] B. C. Carlson, “Elliptic integrals.,” *NIST Handbook of Mathematical Functions*, vol. 1, pp. 485–522, 2010.

[81] S. Rabinowitz, “How to find the square root of a complex number,” *Mathematics and Informatics Quarterly*, vol. 3, no. 54-56, p. 126, 1993.

[82] F. Bowman, “Introduction to elliptic functions with applications,” *(No Title)*, 1953.

[83] P. F. Byrd and M. D. Friedman, *Handbook of elliptic integrals for engineers and physicists*. Springer, 2013, vol. 67.

[84] J. L. C. Rodríguez, J. Martínez, *et al.*, *poliastro: poliastro 0.17.0*, Zenodo, 2023. DOI: 10.5281/zenodo.6817189.

[85] beyond development team, *beyond: Flight Dynamic Library*, Python package (version 0.8) distributed via PyPI, Handles satellite visibility, ground tracks, and space observation functionalities. MIT-licensed., 2025. [Online]. Available: https://pypi.org/project/beyond/.

[86] I. Wolfram Research, *Mathematica, version 14.2*, https://www.wolfram.com/mathematica, Champaign, IL, 2025.

[87] S. C. Chapra, R. P. Canale, *et al.*, *Numerical methods for engineers*. Mcgraw-hill New York, 2011, vol. 1221.

[88] P. Virtanen *et al.*, “Scipy 1.0: Fundamental algorithms for scientific computing in python,” *Nature methods*, vol. 17, no. 3, pp. 261–272, 2020.

[89] Analytical and Computational Mathematics, Inc., “Application and analysis of satellite orbit prediction techniques,” NASA Johnson Space Center, Houston, TX, JSC Internal Note No. 77-FM-19, 1977, JSC Task Monitor: George A. Weisskopf. [Online]. Available: https://ntrs.nasa.gov/citations/19790020037.

[90] E. W. Weisstein, “Cubic formula,” *https://mathworld. wolfram. com/*, 2002.

# A

# Verification

This appendix describes the methods used to verify the implementation of the capabilities required for this work. Section A.1 presents the verification of the conversion routines. The verification of the dynamical model is addressed in Section A.2. Finally, Section A.3 focuses on the verification of the Stark model.

## A.1. Conversions

This section presents the verification of the coordinate conversions employed in this work. The methodology consists of verifying the transformations between Cartesian coordinates and the other coordinate systems considered. Since Cartesian coordinates are used as an intermediate frame, validating these transformations also ensures the correctness of conversions between any pair of coordinate systems. Subsections A.1.1, A.1.2, and A.1.3 address the conversions between Cartesian and Keplerian, Radial-AlongTrack-CrossTrack (RSW), and parabolic coordinates, respectively.

### A.1.1. Cartesian-Keplerian

The verification of the conversion between Cartesian coordinates and Keplerian elements is carried out using the Python library *Poliastro* [84]. For both the direct and inverse transformations, the standard gravitational parameter employed is that defined in *Poliastro*.

For the direct transformation, two Cartesian states are considered, listed in Table A.1. The set C1 corresponds to an arbitrary orbit, while the set C2 represents a circular orbit. The error in the Keplerian

**Table A.1:** Sets of Cartesian coordinates used for verification.

| | $x$ [km] | $y$ [km] | $z$ [km] | $v_x$ [km/s] | $v_y$ [km/s] | $v_z$ [km/s] |
|---|---|---|---|---|---|---|
| **C1** | 7123 | 3485 | 3389 | 3.389 | 7.123 | 3.485 |
| **C2** | 7000 | 0 | 0 | 0 | 7.546 | 0 |

elements between the in-house implementation and the *Poliastro* routine is reported in Table A.2. For

**Table A.2:** Error in the conversion from Cartesian to Keplerian elements.

| | $a$ [km] | $e$ [-] | $i$ [rad] | $\Omega$ [rad] | $\omega$ [rad] | $\theta$ [rad] |
|---|---|---|---|---|---|---|
| **C1** | -1.091e-11 | -1.110e-16 | 0 | 0 | 0 | 0 |
| **C2** | -1.819e-12 | 0 | 0 | 0 | 0 | 0 |

the inverse transformation, the Keplerian elements corresponding to sets C1 and C2 are used (Table A.3). The associated Cartesian errors are presented in Table A.4.

**Table A.3:** Keplerian element sets used for inverse verification.

| | $a$ [km] | $e$ [-] | $i$ [rad] | $\Omega$ [rad] | $\omega$ [rad] | $\theta$ [rad] |
|---|---|---|---|---|---|---|
| **K1** | 2.205e+04 | 8.894e-01 | 4.318e-01 | 5.551 | 5.381 | 2.122 |
| **K2** | 7000 | 0 | 0 | 0 | 0 | 0 |

**Table A.4:** Error in the conversion from Keplerian to Cartesian coordinates.

| | $x$ [km] | $y$ [km] | $z$ [km] | $v_x$ [km/s] | $v_y$ [km/s] | $v_z$ [km/s] |
|---|---|---|---|---|---|---|
| **K1** | 0 | 4.547e-13 | 0 | -4.441e-16 | -2.665e-15 | -8.882e-16 |
| **K2** | 0 | 0 | 0 | 0 | 0 | 0 |

### A.1.2. Cartesian-RSW

The conversion between Cartesian and RSW frames is verified using the Python library *beyond* [85]. Because the transformation matrix between these frames is orthonormal, the inverse is equal to its transpose; thus, validating the forward transformation suffices to verify the inverse as well.

Since the RSW frame is defined locally, the transformation depends on the Cartesian state vector. The sets C1 and C2 from Table A.1 are used. In addition, a dimensionless vector $\bar{\mathbf{u}}$ in the Cartesian frame is transformed:

$$\bar{\mathbf{u}} = [1, 2, 3] \tag{A.1}$$

The resulting errors are reported in Table A.5.

**Table A.5:** Error in the conversion between Cartesian and RSW frames.

| | $R$ [-] | $S$ [-] | $W$ [-] |
|---|---|---|---|
| **C1** | 0 | 0 | 0 |
| **C2** | 0 | 0 | 0 |

### A.1.3. Cartesian-Parabolic

The conversion between Cartesian and parabolic coordinates is verified using *Wolfram Mathematica* [86]. As this transformation is nonlinear, both the direct and inverse mappings must be verified. It is noted, however, that *Mathematica* provides conversions only for position coordinates; explicit verification of velocity components is therefore not possible. Nonetheless, the subsequent verification of the Stark model in Section A.3 implicitly validates the parabolic velocity formulation, since the model is expressed in parabolic coordinates.

For the direct transformation, sets C1 and C2 from Table A.1 are employed. The associated errors are shown in Table A.6. For the inverse transformation, the parabolic coordinates corresponding to C1 and

**Table A.6:** Error in the conversion between Cartesian and parabolic coordinates.

| | $\xi$ [km$^{\frac{1}{2}}$] | $\eta$ [km$^{\frac{1}{2}}$] | $\phi$ [rad] |
|---|---|---|---|
| **C1** | 0 | 0 | 0 |
| **C2** | 0 | 0 | 0 |

C2 are listed in Table A.7. The Cartesian errors for the inverse mapping are given in Table A.8.

**Table A.7:** Parabolic coordinate sets used for verification.

| | $\xi$ [$km^{\frac{1}{2}}$] | $\eta$ [$km^{\frac{1}{2}}$] | $\phi$ [rad] | $\dot{\xi}$ [$km^{\frac{1}{2}}/s$] | $\dot{\eta}$ [$km^{\frac{1}{2}}/s$] | $\dot{\phi}$ [$rad/s$] |
|---|---|---|---|---|---|---|
| **P1** | 1.096e+02 | 7.235e+01 | 4.550e-01 | 4.805e-02 | 2.462e-02 | 6.190e-04 |
| **P2** | 8.367e+01 | 8.367e+01 | 0 | 0 | 0 | 1.078e-03 |

**Table A.8:** Error in the conversion from parabolic to Cartesian position coordinates.

| | $x$ [km] | $y$ [km] | $z$ [km] |
|---|---|---|---|
| **P1** | 0 | 0 | 0 |
| **P2** | 0 | 0 | 0 |

# A.2. Dynamical Model

This section presents the verification of the dynamical model. The process is divided into two parts: verification of the acceleration model and verification of the planet-centred solar-sail locally optimal control laws (LOCLs). The former is described in Subsection A.2.1, while the latter is addressed in Subsection A.2.2.

## A.2.1. Acceleration Model

The acceleration model accounts for Earth point-mass gravity and solar radiation pressure (SRP). Verification is carried out in two stages: first, the two-body problem (TBP) acceleration model is validated, and then SRP is added on top of the verified TBP dynamics.

### Earth Point-Mass

The point-mass gravity model has been implemented following the formulation of the TBP given in [43]. In the TBP, all Keplerian elements remain constant except for the true anomaly. To verify correct implementation, an orbit propagation in Cartesian coordinates was performed.

The initial Keplerian conditions are listed in Table A.9. Using these conditions, the orbit was propagated

**Table A.9:** Initial conditions in Keplerian elements.

| $a$ [km] | $e$ [-] | $i$ [rad] | $\Omega$ [rad] | $\omega$ [rad] | $\theta$ [rad] |
|---|---|---|---|---|---|
| 7.346e+03 | 7.414e-03 | 1.209e+02 | 2.527e+02 | 6.552e+01 | 2.937e+02 |

for one day. The resulting evolution of the Keplerian elements is shown in Fig. A.1. Figure A.1 confirms

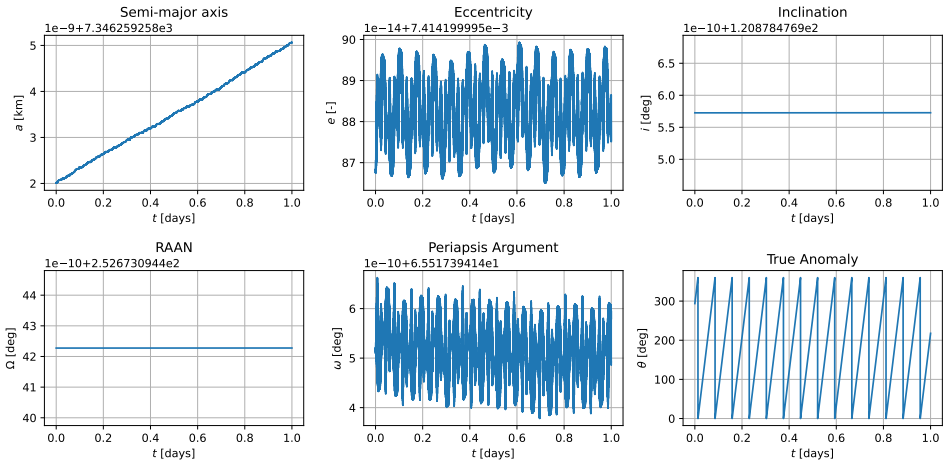


**Figure A.1:** Evolution of Keplerian elements for a one-day propagation of the TBP.

that the Keplerian elements remain nearly constant, with deviations attributable to numerical integration errors. As an additional validation step, the propagation was compared to a proprietary analytical solution of the Kepler problem. Figure A.2 shows the evolution of the error, further confirming the correct implementation of the TBP model.

### Solar Radiation Pressure

The SRP acceleration model was implemented using the planet-centred solar-sail equations of motion from [1]. To verify correctness, the planet-centred locally optimal control law for semi-major axis (SMA)-raising described in [1] was reproduced. The simulation uses the lightness number and initial conditions

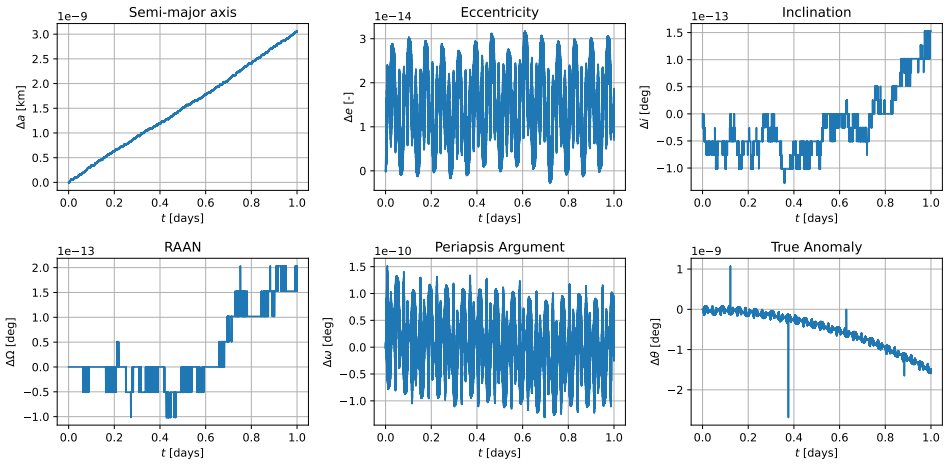


**Figure A.2:** Evolution of error in Keplerian elements for a one-day propagation between the numerical propagation and the analytical implementation of the Kepler Problem.

**Table A.10:** Ligthness number and initial conditions for verification of SRP accleration model.

| $\beta$ [-] | $a$ [km] | $e$ [-] | $i$ [rad] | $\Omega$ [rad] | $\omega$ [rad] | $\theta$ [rad] |
|---|---|---|---|---|---|---|
| 0.17 | 42241 | 0 | 0 | 0 | 0 | 0 |

in Table A.10. The propagation was performed for three periods of the initial orbit. Figure A.3 shows the evolution of the SMA, eccentricity, and sail cone angle, along with a two-dimensional trajectory plot. The agreement between the obtained results and those published in [1] verifies the implementation of

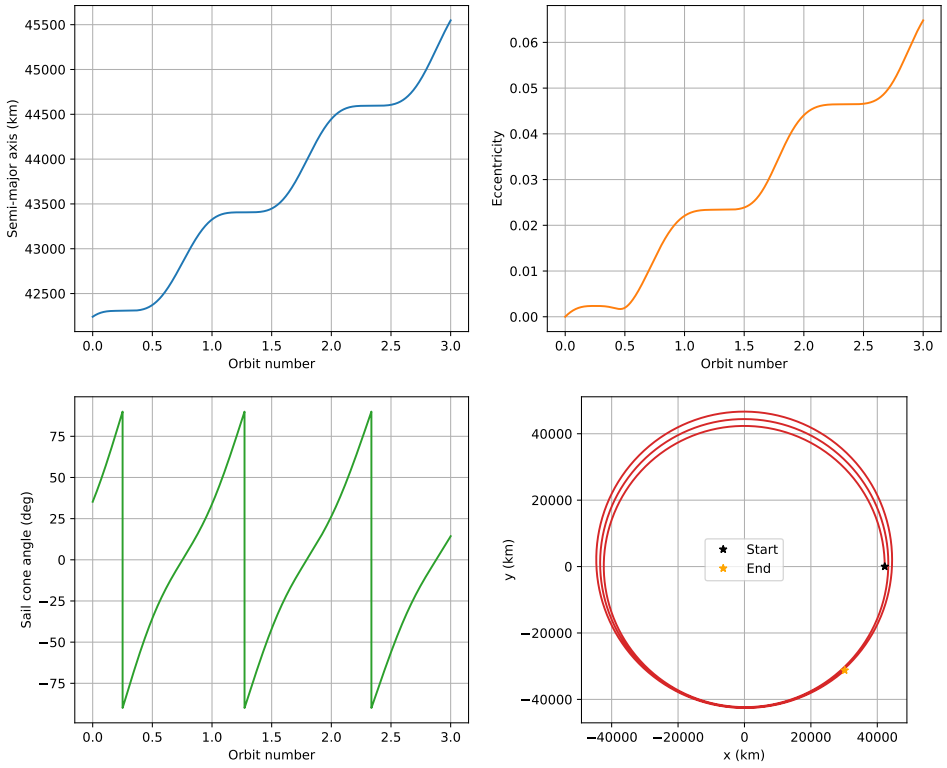


**Figure A.3:** Evolution of the SMA, eccentricity, and sail cone angle for a propagation of three initial-orbit periods. Additionally, a two-dimensional representation of the trajectory is shown.

the SRP acceleration model.

### A.2.2. Planet-Centred Solar-Sail Locally Optimal Control Laws

The LOCLs were implemented following the derivations in [31]. Verification was carried out by comparing the proprietary implementation with reference data provided by Carzana [32], which includes evaluations of SMA- and inclination-raising LOCLs at multiple points along a Keplerian orbit.

The orbital parameters, lightness number, and gravitational parameter used for the test case are reported in Table A.11. The dataset consists of 721 evaluations uniformly spaced in true anomaly over $\theta \in [0, 360]^\circ$.

**Table A.11:** Earth's standard gravitational parameter, lightness number and initial Keplerian elements for verification of the LOCLs.

| $\mu$ [km$^3$/s$^2$] | $\beta$ [-] | $a$ [km] | $e$ [-] | $i$ [rad] | $\Omega$ [rad] | $\omega$ [rad] | $\theta$ [rad] |
|---|---|---|---|---|---|---|---|
| 398600.441 | 0.0077 | 7500 | 0.123 | 1.1849342 | 2.0037891 | 9.4809535 | 0 |

Figures A.4 and A.5 present the evolution of the cone ($\alpha$) and clock ($\delta$) angles for the SMA- and inclination-raising LOCLs, respectively.

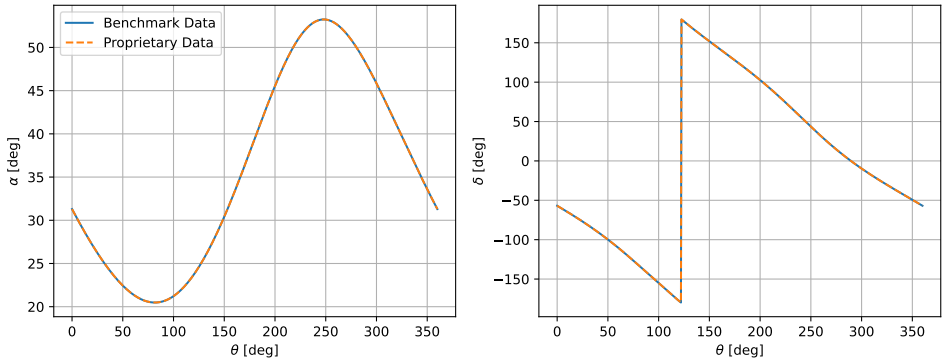


**Figure A.4:** Evolution of the cone, $\alpha$, and clock, $\delta$, angles for an SMA-raising LOCL along the full range of values of the true anomaly of a Keplerian orbit.

Figure A.5 shows the evolution of the cone and clock angles for the inclination-raising LOCL along the defined states. The agreement between the proprietary implementation and the reference data verifies

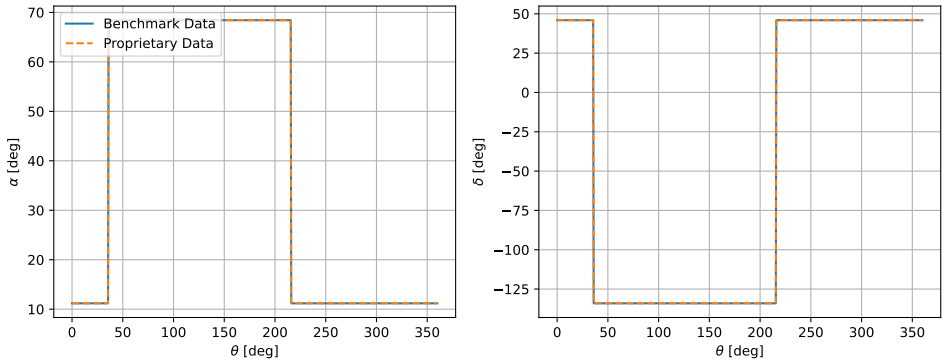


**Figure A.5:** Evolution of the cone, $\alpha$, and clock, $\delta$, angles for an inclination-raising LOCL along the full range of values of the true anomaly of a Keplerian orbit.

the correctness of the SMA- and inclination-raising control laws. While no external data was available for the remaining LOCLs, their derivation differs only in the choice of the vector $\boldsymbol{\lambda}$, as shown in Table 4.1. Since the computational process is otherwise identical, verification of these two cases suffices to confirm the correct implementation of a generic planet-centred solar-sail LOCL.

## A.3. Stark Model

This section presents the verification of the Stark model. For the purposes of this work, only the bounded case is considered, and therefore only this case has been verified numerically.

The bounded case is governed by Eqs. (5.168), (5.169), and (5.170). These define the evolution of the parabolic coordinates with respect to the fictitious times, the relations between fictitious and physical times, and the parameters used in the formulation, respectively.

Verification was carried out by reproducing a reference case reported in [70]. The standard gravitational parameter $\mu$, the initial state vector $\tilde{\mathbf{x}}_0$, and the perturbation magnitude $\epsilon$ employed are listed in Table A.12. Figure A.6 shows the three-dimensional trajectory (Fig. A.6a) and the time evolution of the semi-

**Table A.12:** Standard gravitational parameter, initial conditions and magnitude of the perturbation for the verification of the bounded case of the Stark model.

| $\mu$ [-] | $\tilde{\mathbf{x}}_0$ [-] | $\epsilon$ |
|---|---|---|
| 1 | [1,0,0,0,0.866,0.5] | 0.0103 |

major axis, eccentricity, inclination, and argument of periapsis (Fig. A.6b) for the analytical propagation of the initial conditions in Table A.12. The results are in full agreement with those published in [70], thereby confirming the correct implementation of the Stark model for the bounded case.

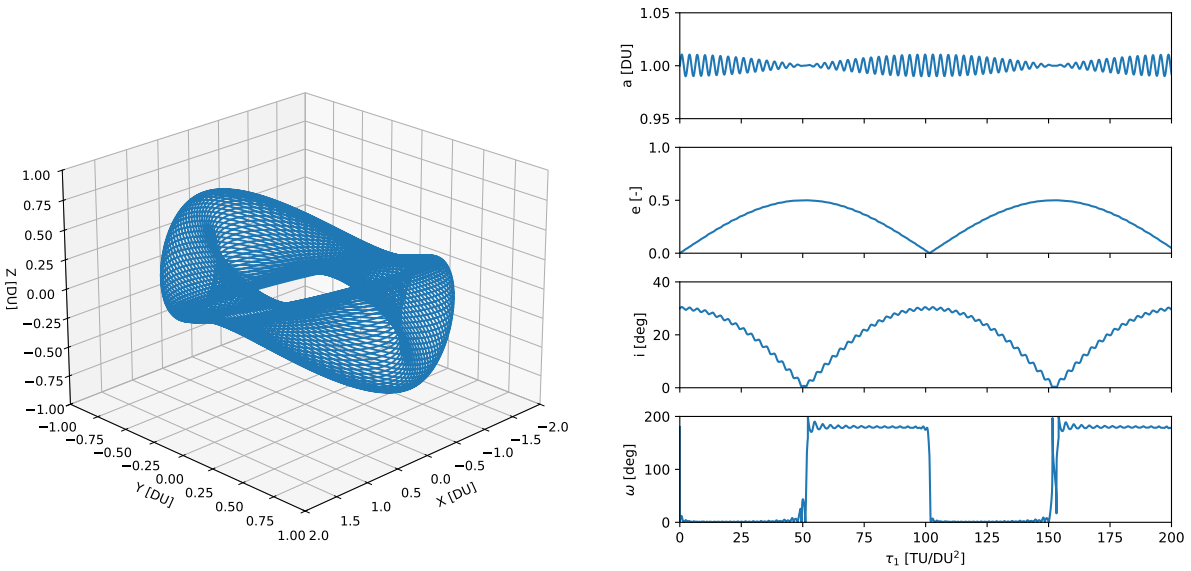


(a) (b)

**Figure A.6:** (a) Three-dimensional trajectory and (b) evolution of the SMA, eccentricity, inclination, and argument of periapsis for the initial conditions given in Table A.12.

It is worth noting that in [70] the horizontal axis of the Keplerian element plots is labelled as the physical time $t$, whereas in this implementation the fictitious time $\tau_1$ is used. The relationship between $t$ and $\tau_1$ for the case considered is shown in Fig. A.7. The figure indicates that the physical time spans approximately twice the range of the fictitious time. Since the trends in Fig. A.6b are equivalent to those reported in [70], it is assumed that the labelling of the horizontal axis in the reference was incorrect.

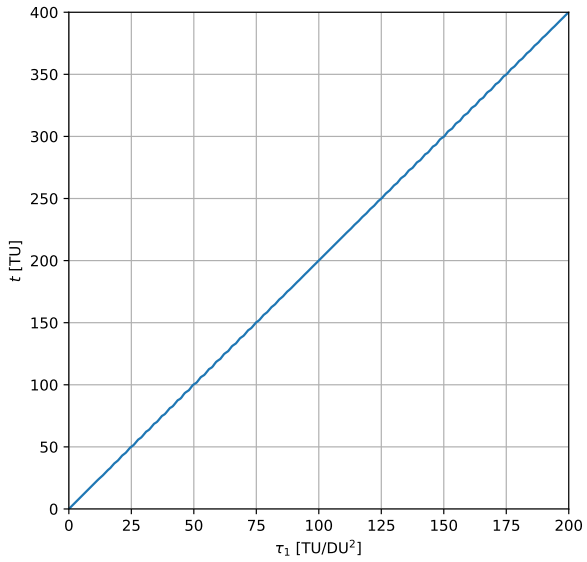


**Figure A.7:** Relation between the physical time $t$ and the fictitious time $\tau_1$ for the initial conditions given in Table A.12.

# B

# Benchmark Definition

This appendix describes the methodology employed to define the numerical benchmark used throughout this work. For each control law considered, numerical integrations were performed at different tolerances. The solution obtained at a given tolerance was compared against that computed with a tolerance one order of magnitude smaller, thereby providing an estimate of the integration error at the larger tolerance. This approach enables the identification of the tolerance value for which the truncation error, introduced by the integration scheme, equals the round-off error caused by floating-point arithmetic limitations [87].

The chosen numerical integrator is the *SciPy* implementation of the Runge-Kutta 45 (RK45) scheme [88]. RK45 was selected due to its robustness and efficiency, stemming from its step-size adaptability, which makes it particularly suitable for trajectory propagation problems [89].

The reference parameters used in the analysis are summarized in Table B.1, including the solar and Earth standard gravitational parameters as well as the Advanced Composite Solar Sail System (ACS3) solar-sail lightness number. The initial conditions of the reference orbit, expressed in both Cartesian and Keplerian form in the Earth Centred Inertial (ECI) frame, are reported in Table B.2. The tolerance sampling strategy is described in Table B.3. A logarithmic distribution of 17 values was adopted over the interval $\left[10^{-20}, 10^{-4}\right]$. For the lowest tolerance, $tol = 10^{-20}$, the error was estimated by comparison with a simulation at $tol = 10^{-21}$. The results of the benchmark definition analysis are presented in Fig.

**Table B.1:** Reference values: solar standard gravitational parameter $\mu_\odot$, Earth's standard gravitational parameter $\mu_E$, and solar-sail lightness number $\beta$.

| $\mu_\odot$ [m$^3$/s$^2$] | $\mu_E$ [m$^3$/s$^2$] | $\beta_{ACS3}$ [-] |
|---|---|---|
| 1.327e+20 | 3.986e+14 | 0.0077 |

**Table B.2:** Initial conditions of the reference orbit in the ECI frame, given in Cartesian and Keplerian form.

| $x$ [km] | $y$ [km] | $z$ [km] | $v_x$ [km/s] | $v_y$ [km/s] | $v_z$ [km/s] |
|---|---|---|---|---|---|
| -2.132e+03 | -7.006e+03 | -8.606e+01 | -3.635 | 1.080 | 6.341 |
| $a$ [km] | $e$ [-] | $i$ [deg] | $\Omega$ [deg] | $\omega$ [deg] | $\theta$ [deg] |
| 7.346e+03 | 7.414e-03 | 120.9 | 252.7 | 65.52 | 293.7 |

**Table B.3:** Tolerances employed in the benchmark definition analysis: interval, number of elements, and distribution.

| | Tolerance [-] |
|---|---|
| **Interval** | $\left[10^{-20}, 10^{-4}\right]$ |
| **Elements** | 17 |
| **Distribution** | Logarithmic |

B.1 for the different control laws: constant (Fig. B.1a), semi-major axis (SMA. Fig. B.1b), eccentricity (Fig. B.1c), inclination (Fig. B.1d), right ascension of the ascending node (RAAN, Fig. B.1e), and argument of periapsis (Fig. B.1f). In all cases, the position error exhibits a change in behaviour at $tol = 10^{-14}$, marked by the red dashed line. This tolerance is identified as the lowest value unaffected by round-off error. Consequently, $tol = 10^{-14}$ was selected for the benchmark simulations.

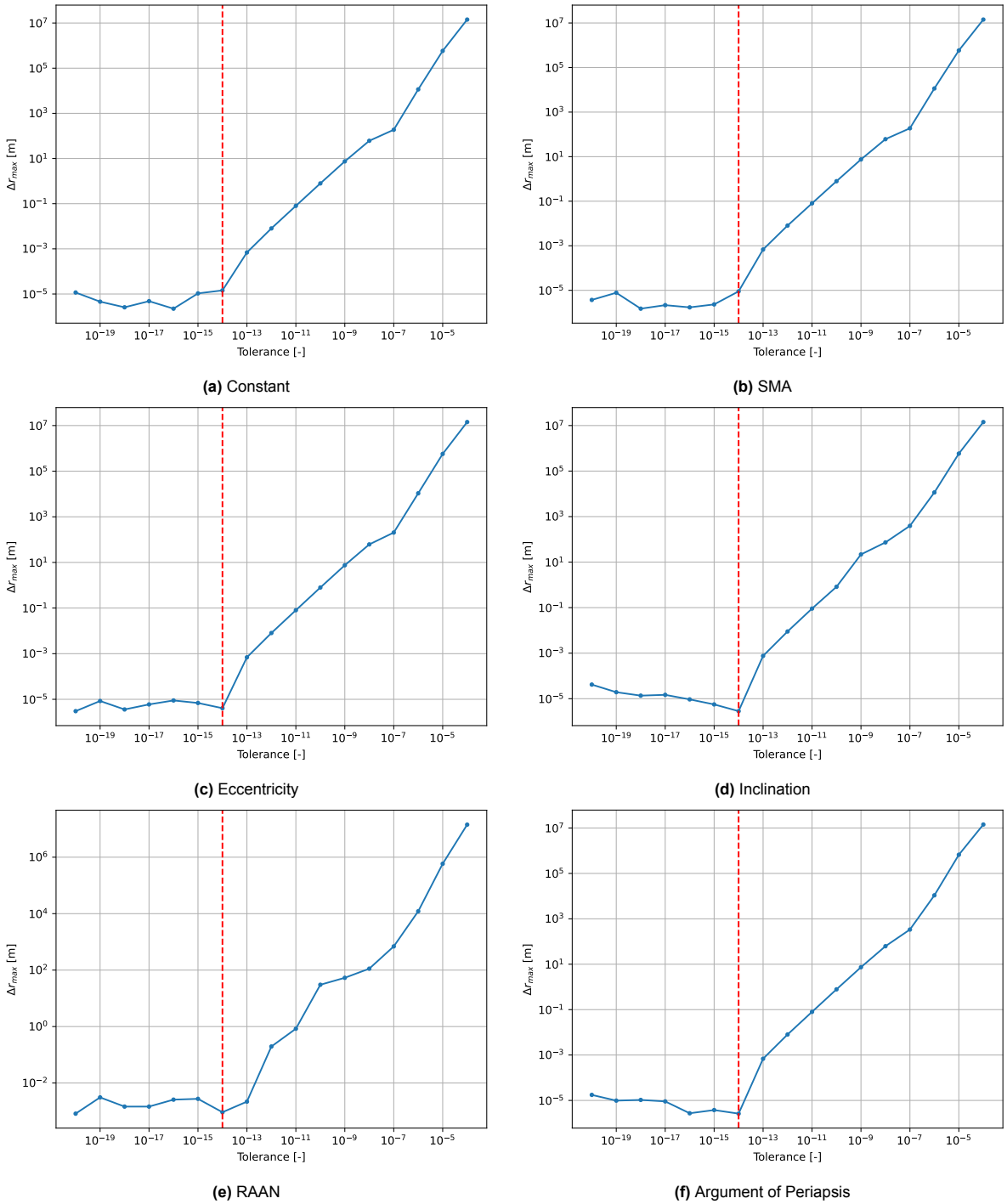


**(a)** Constant

**(b)** SMA

**(c)** Eccentricity

**(d)** Inclination

**(e)** RAAN

**(f)** Argument of Periapsis

**Figure B.1:** Position error resulting from the benchmark definition analysis for the tolerances given in Table B.3 for different control laws: constant (a), SMA (b), eccentricity (c), inclination (d), RAAN (e), and argument of periapsis (f). The red, dashed line corresponds to a tolerance of $tol = 10^{-14}$, which corresponds to the tolerance chosen for the benchmark.

# C

# Solution to the Cubic Equation

This appendix presents the detailed derivation of the solution to the cubic equation, which is required for the integration of the equations of motion of the Stark problem introduced in Chapter 5. The objective is to characterize the roots of the polynomial $P_1(Y)$ in Eq. (5.43) as a function of the coefficients of the cubic. The methodology follows the approach described in [90].

The first step consists in transforming the general cubic into its depressed form. This is achieved through the variable substitution given by:

$$Y = Y' - \frac{a_2}{3a_1} \tag{C.1}$$

Substitution in Eq. (C.1) eliminates the quadratic term. Applying this transformation, $P_1(Y)$ can be rewritten as:

$$P_1(Y') = a_1\left(Y'^3 + \bar{p}Y' + \bar{q}\right) \quad \textit{where} \quad \bar{p} = \frac{3a_1a_3 - a_2^2}{3a_1^2} \quad \& \quad \bar{q} = \frac{2a_2^3 - 9a_1a_2a_3 + 27a_1^2a_4}{27a_1^3} \tag{C.2}$$

Hence, the problem reduces to solving the depressed cubic equation given by:

$$Y'^3 + \bar{p}Y' + \bar{q} = 0 \tag{C.3}$$

To further simplify the problem, Vieta's substitution is introduced:

$$Y' = Y'' - \frac{\bar{p}}{3Y''} \tag{C.4}$$

Substituting Eq. (C.4) into Eq. (C.3) yields the following:

$$Y''^3 - \frac{\bar{p}^3}{27Y''^3} + \bar{q} = 0 \tag{C.5}$$

Multiplying Eq. (C.5) by $Y''^3$ and defining $Y''' = Y''^3$ leads to a quadratic equation:

$$Y'''^2 + \bar{q}Y''' - \frac{\bar{p}^3}{27} = 0 \tag{C.6}$$

Equation (C.6) is solved using the quadratic formula, yielding two possible values for $Y'''$:

$$Y''' = R \pm \sqrt{R^2 + Q^3} \quad \textit{where} \quad R = -\frac{1}{2}\bar{q} \quad \& \quad Q = \frac{1}{3}\bar{p} \tag{C.7}$$

In Eq. (C.7), the radicand corresponds to the discriminant of the cubic equation.

$$D = R^2 + Q^3 \tag{C.8}$$

From the two solutions of $Y'''$, the corresponding values of $Y''$ can be expressed as:

$$Y_1'' = \sqrt[3]{R + \sqrt{D}} \tag{C.9}$$

$$Y_2'' = \sqrt[3]{R - \sqrt{D}} \tag{C.10}$$

Using Eq. (C.4), the three solutions of the depressed cubic equation are then given by:

$$\begin{aligned} Y_1' &= (Y_1'' + Y_2'') \\ Y_2' &= -\frac{1}{2}(Y_1'' + Y_2'') + i\frac{\sqrt{3}}{2}(Y_1'' - Y_2'') \\ Y_3' &= -\frac{1}{2}(Y_1'' + Y_2'') - i\frac{\sqrt{3}}{2}(Y_1'' - Y_2'') \end{aligned} \tag{C.11}$$

Finally, applying the transformation in Eq. (C.1), the solutions of the original cubic equation are obtained:

$$\begin{aligned} Y_1 &= -\frac{a_2}{3a_1} + (Y_1'' + Y_2'') \\ Y_2 &= -\frac{a_2}{3a_1} - \frac{1}{2}(Y_1'' + Y_2'') + i\frac{\sqrt{3}}{2}(Y_1'' - Y_2'') \\ Y_3 &= -\frac{a_2}{3a_1} - \frac{1}{2}(Y_1'' + Y_2'') - i\frac{\sqrt{3}}{2}(Y_1'' - Y_2'') \end{aligned} \tag{C.12}$$

Equation (C.12) provides the general form of the solution to a cubic equation. The nature of the roots depends on the sign of the discriminant $D$:

- If $D > 0$: $\quad Y_i \in \mathbb{C} \quad \forall\, i \in [1,3]$
- If $D = 0$: $\quad Y_i \in \mathbb{R} \quad \forall\, i \in [1,3] \quad \& \quad Y_2 = Y_3$
- If $D < 0$: $\quad Y_i \in \mathbb{R} \quad \forall\, i \in [1,3]$

In Chapter 5, these cases are employed to determine the explicit solutions of the equations of motion of the Stark problem depending on the discriminant.

# D

# Work Breakdown Structure

This appendix provides an overview of the thesis organisation. Table D.1 presents a detailed description of the work packages, including their expected duration in weeks and a concise summary of their objectives. The project timeline, organised according to these work packages, is illustrated in the Gantt chart in Fig. D.1.

**Table D.1:** Thesis work packages description.

| Work package | Weeks | Description |
|---|---|---|
| 1. Literature Review | 6 | Review of state-of-the-art research. |
| 2. Research Proposal Reporting | 1 | Preparation of the research proposal. |
| * Research Proposal Deliverable | - | Milestone |
| 3. Dynamical Model | 3 | - |
| 3.1. Model Definition | 1 | Specification of the dynamical model. |
| 3.2. Model Implementation | 1 | Implementation of the dynamical model. |
| 3.3. V&V | 1 | Validation and Verification of the dynamical model. |
| 4. Analytical Model | 6 | - |
| 4.1. Model Implementation | 3 | Implementation of the Stark model. |
| 4.2. V&V | 1 | Validation and Verification of the Stark model. |
| 4.3. Code Profiling | 2 | Optimisation of the computational performance of the analytical model. |
| 5. Mid-Term Deliverable Reporting | 2 | Preparation of the Mid-Term report. |
| * Mid-Term Deliverable | - | Milestone |
| + Vacation | 2 | - |
| 6. Analysis | 8 | - |
| 6.1. Constant Control Law | 4 | Analysis under constant laws. |
| 6.2. Time-Varying Control Law | 4 | Analysis under time-varying control laws. |
| + Vacation | 2 | - |
| 7. Thesis Draft Reporting | 6 | Preparation of the thesis draft. |
| * Thesis Draft Deliverable | - | Milestone |
| 8. Final Thesis Reporting | 2 | Finalisation of the thesis report. |
| * Final Thesis Hand-In | - | Milestone |
| 9. Defence Preparation | 2 | Preparation for the thesis defence. |
| * Thesis Defence | - | Milestone |

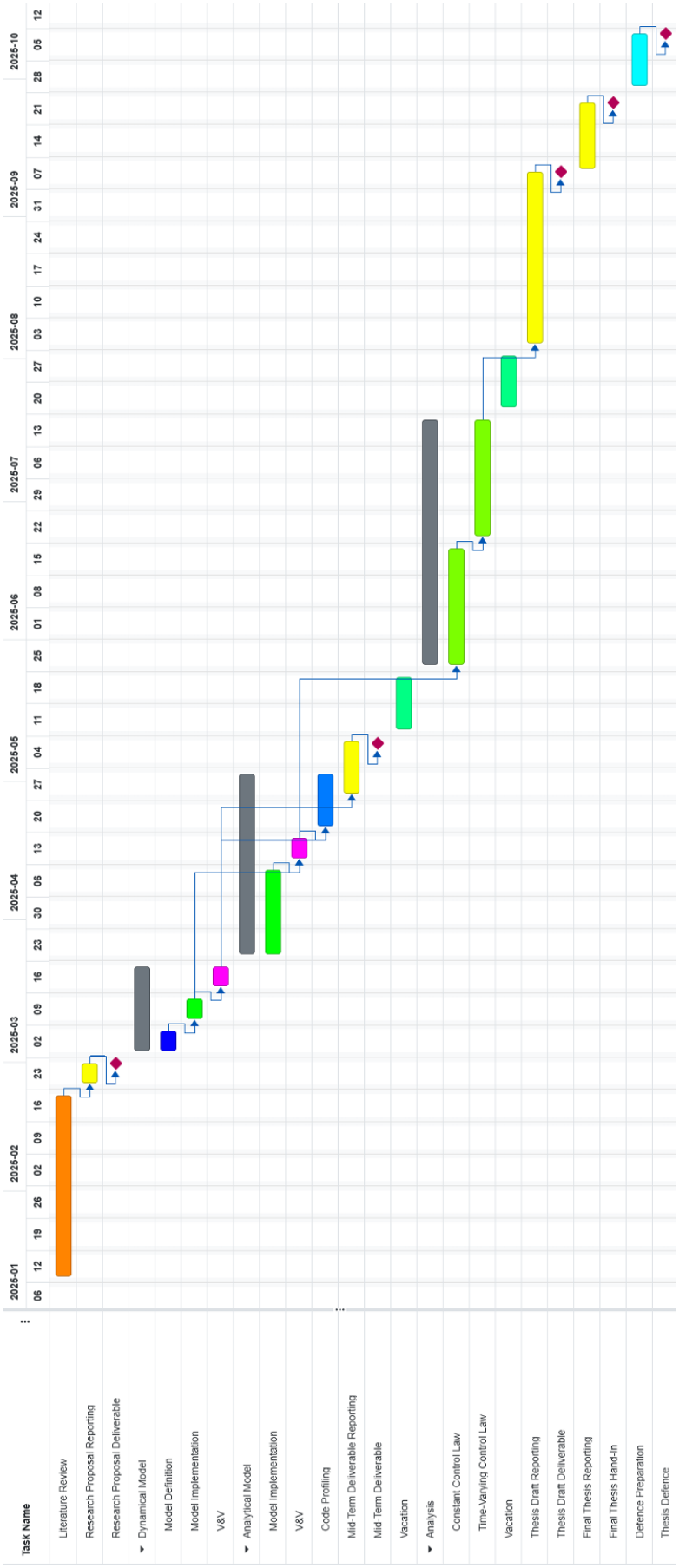


**Figure D.1:** Gantt chart of the thesis.